EUCHEMBIOJ

ISSN: 3023-5839

www.euchembioj.com

The European Chemistry and Biotechnology Journal

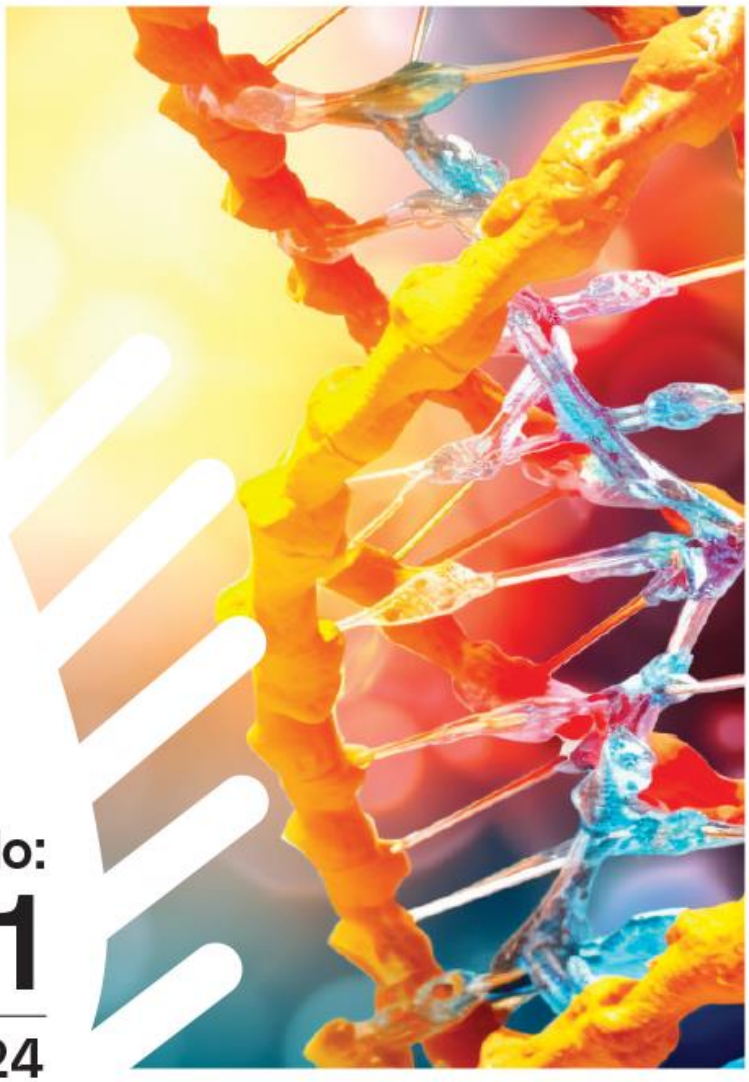

No: 01

2024

The European Chemistry and Biotechnology Journal

Issue 1 ● January 2024

Publisher: Tunc Catal
Publishing manager: Prof. Dr. Tunc Catal
Editorial office: Uskudar University, Universite Sok. No:14 34662 Altunizade Uskudar, Istanbul-Türkiye
Email: editor@euchembioj.com; **Phone**: +90 216 400 2222 (ext. 2417)
WEB: https://euchembioj.com/index.php/pub
DOI: https://doi.org/10.62063/ecb-no1.2024; **ISSN**: 3023-5839

The European Chemistry and Biotechnology Journal

Issue 1 ● January 2024

CONTENTS

EUCHEMBIOJ

THE EUROPEAN CHEMISTRY AND BIOTECHNOLOGY JOURNAL

Eur. Chem. Biotechnol. J. 1: 1-10 (2024) www.euchembioj.com

Research article

Novel N,S-Substituted naphthoquinone analogues from aminonaphthoquinones

Halil Ozdinc[1] | ORCID 0009-0003-3140-6206 | halilozdinc@gmail.com

Nihal Onul[*1] | ORCID 0000-0002-0101-1735 | nihalonul@iuc.edu.tr

Funda Ozkok[1] | ORCID 0000-0001-7263-1977 | ozkok@iuc.edu.tr

[1]**Istanbul University-Cerrahpaşa, Faculty of Engineering, Department of Chemistry, Avcilar-Istanbul, Türkiye**

*** Corresponding author**: nihalonul@iuc.edu.tr; Ph: +90-212-4737070; Fax: +90-212-4737180.

Received: 10.10.2023
Accepted: 01.12.2023
Published: 02.01.2024

Cite this article: Ozdinc, H., Onul, N., & Ozkok, F. (2024). Novel N,S-Substituted naphthoquinone analogues from aminonaphthoquinones. *The European chemistry and biotechnology journal*, *1*, 1-10. https://doi.org/10.62063/ecb-13

Abstract

In this study, novel N,S-substituted naphthaquinone analogues **(2, 4, 6,** and **8)** were synthesized from the reactions of previously known aminonaphthaquinone derivatives **(1, 3, 5, and 7)** with allyl mercaptan. 2-(allylthio)-3-(4-phenylpiperazin-1-yl)naphthalene-1,4-dione **(2)**, 2-(allylthio)-3-(4-(2-fluorophenyl)piperazin-1-yl)naphthalene-1,4-dione **(4)**, 2-(allylthio) -3-(4-benzylpiperidin-1-yl)naphthalene-1,4-dione **(6)** and 2-(4-chlorophenylamino)-3-(allylthio)naphthalene-1,4-dione (8) were obtained from the reactions of 2-chloro-3-(4-phenylpiperazin-1-yl)naphthalene-1,4-dione (1), 2-chloro-3-(4-(2-fluorophenyl)piperazin-1-yl)naphthalene-1,4-dione **(3)**, 2-(4-benzylpiperidin-1-yl)-3-chloronaphthalene-1,4-dione **(5)**, and 2-(4-chlorophenylamino) -3-chloronaphthalene-1,4-dione **(7)** with allyl mercaptan according to the general synthesis procedure. Synthesized new naphthaquinone analogues **(2, 4, 6, and 8)** were purified by column chromatography. The chemical structures of these novel N,S-substituted naphthaquinone analogues were characterized by spectroscopic methods (FT-IR, NMR, and MS).

Keywords: Aminonaphthoquinone, Naphthoquinone, Thionaphthoquinone.

Introduction

Natural naphthoquinone derivatives have been used in traditional Chinese medicine for centuries and are known to treat disease (Hussain et al., 2007; Cruz et al., 2014; Lopez et al., 2014; Aziz et al., 2008; Masi et al., 2017; Inagaki et al., 2015; Borghese et al., 2017). The Lawsone molecule, an important naphthoquinone derivative, has also been shown to be effective in killing mosquitoes that transmit the Zika virus (Masi et al., 2017; Inagaki et al., 2015). Vitamin K1, which plays an active role in blood clotting, is the most well-known naphthoquinone derivative (Kar et al., 2003; Nishikawa et al., 2015). Naphthoquinones constitute an important subclass of quinones, which are found in nature and from

which various derivatives can be obtained synthetically. Plumbagone, juglon, and lawsone are plant-derived naphthoquinones with antibacterial activity against various aerobic and anaerobic organisms. Toxins derived from naphthozarin (5,8-dihydroxy-1,4-naphthoquinone) are produced by Fusarium solani and attack plants, other fungi, and bacteria (Peralta et al., 2015; Riffel et al., 2002). Aliphatic thiols are important starting materials for the synthesis of thiophosphoric acid esters, drugs, and polysulfides and are often used as polymerization modifiers in rubber and plastics production. The most important industrial applications of aromatic thiols are as intermediates in the production of pharmaceuticals, agrochemicals, dyes and pigments, and chemicals for the electronics industry (Vollhardt et al. 2009; Roy et al. 2000). The biological activity properties of amino and thionaphthoquinones are known from the literature (Durán et al., 2023; Kavaliauskas et al., 2022; Liu et al., 2023; López-López et al., 2022; Souza et al., 2023). In this study, novel N,S-substituted naphthoquinone analogues 2, 4, 6, and 8 were synthesized from the reactions of previously known aminonaphthoquinone derivatives 1 (Kalmayer et al. 1991), 3 (Tadashi et al. 1996), 5 (Vanallan et al. 1963), and 7 (Fries et al. 1922) with allyl mercaptan. Synthesized new naphthoquinone analogues (2, 4, 6, and 8) were purified by column chromatography, and their chemical structure was characterized by spectroscopic methods (FT-IR, NMR, MS).

Materials and methods

Chemistry

Infrared (FT-IR) spectra were recorded with the ATR method on a Termo Scientific Nicolet 6700. ^{1}H and ^{13}C NMR spectra were recorded on Spectrometer Varian UNITY INOVA 500 MHz (CDCl3, DMSO-d6 solvent, TMS (δ = 0) internal standard). Mass spectra were obtained on a Shimadzu LC-MS 8030 triple quadrupole mass spectrometer. (Mobile phase A: water (5 mμ ammonium formate), Mobile phase B: acetonitrile (5 mμ ammonium formate)). Products were purified by column chromatography on silica gel (Merck silica gel 60, 0.063-0.2 mm). Melting points were measured on a Buchi SMP20 (B-540) apparatus. Thinlayer chromatography (TLC) was purchased from Merck DC-AlufolienKieselgel 60F254. The solvents used during the reactions and purification of the products were recovered in a Rotavapor Büchi Heatig Bath B-490. Chromatograms were observed using a CAMAG Muttenz-Schweiz 29200 UV lamp. All chemicals used in the reactions were obtained from Merck, Sigma-Aldrich.

Synthesis

General synthesis method. N-substituted naphthoquinone derivative and allyl mercaptan in an equivalent molar ratio were stirred in a 250 mL flask in the presence of 60 mL of dichloromethane and triethylamine for 6 h on a magnetic stirrer at room temperature. The reaction mixture in the flask was extracted with methylene chloride and 200 mL (50 mL x 4) water. The organic phase was dried over sodium sulfate. After recovery of the solvent in the evaporator, the crude products were separated and purified by column chromatography. The chemical structures of the synthesized naphthoquinone analogues were elucidated by spectroscopic methods (NMR, FT-IR, and MS).

2-(allythio)-3-(4-phenylpiperazine-1-yl)naphthalene-1,4-dione (2)

2-(allythio)-3-(4-phenylpiperazine-1-yl)naphthalene-1,4-dione (2) was synthesized from the reaction of 0.5 g (1.417 mmol) 2-Chloro-3-(4-phenylpiperazine-1-yl)naphthalene-1,4-dione (1) and 0.105 g (1.417 mmol) allyl mercaptan according to general synthesis procedure.

2: Red solid. Yield: 0.097 g (% 17.6). FT-IR (ATR):υ (cm^{-1})= 3200 ($CH_{aromatic}$), 2963, 2910 ($CH_{aliphatic}$), 1534, 1501 cm^{-1} ($C{=}C_{aromatic}$), 1638, 1617 (C=O); ^{1}HNMR (500 MHz, CDCl3): δ = 7.9-8.0 (dd, 2H, $CH_{naphthoquinone}$), 7.5-7.6 (m, 2H, $\boldsymbol{C}H_{naphthoquinone}$), 7.2-7.3 ve 6.9-7.0 (m, 5H, $\boldsymbol{C}H_{aromatic}$), 5.6-5.8 (m, H, $\boldsymbol{C}H{=}$), 4.9-5.0 (m, 2H, $=\boldsymbol{C}H_2$), 3.2-3.7 (m, 6H, N-CH_2, S-$\boldsymbol{C}H_2$), 2.4-2.9 (m, 4H, N-$\boldsymbol{C}H_2$); ^{13}C NMR (125 MHz, *CDCl$_3$*): δ = 182.1-181 (***C***=O), 154 ($\boldsymbol{C}_{aromatic}$-N), 145.2 ($\boldsymbol{C}_{naphthoquinone}$-N), 129 ($\boldsymbol{C}_{naphthoquinone}$), 134.5, 132, 131 ($\boldsymbol{C}_{naphthoquinone}$, $\boldsymbol{C}H_{naphthoquinone}$), 129.5, 118, 116 ($\boldsymbol{C}H_{aromatic}$), 37.7 (S-$\boldsymbol{C}H_2$), 117 ($=\boldsymbol{C}H_{2\ ally}$), 133.9 ($\boldsymbol{C}H{=}_{ally}$), 52.4 ($\boldsymbol{C}H_2$-N); +ESI: *m/z*= 391 $[M+H]^+$, *m/z* =350 $[M-(CH_2\text{-}CH{=}CH_2)]^+$, $C_{23}H_{22}N_2O_2S$, (M=390.5 g/mol).

2-(alylthio)-3-(4-(2-fluorophenyl)piperazine-1-yl)naphthalene-1,4-dione (4)

2-(alylthio)-3-(4-(2-fluorophenyl)piperazine-1-yl)naphthalene-1,4-dione **(4)** was synthesized from the reaction of 2-chloro-3-(4-(2-fluorophenyl)piperazin-1-yl)naphthalene-1,4-dione **(3)** (0.6 g, 1.618 mmol) and allyl mercaptan (0.12 g) to general synthesis procedure.

4: Dark red viscos. Yield: 0.179 g (% 27.1). FT-IR (ATR):υ (cm^{-1})= 3010 ($CH_{aromatic}$), 2950 ($CH_{aliphatic}$), 1646 (C=O), 1541, 1500 (C=C); ^{1}HNMR (500 MHz, *CDCl₃*): δ = 7.5-8.0 (m, 4H, C***H***$_{naphthoquinone}$), 6.8-7.0 (m, 4H, C***H***$_{aromatic}$), 5.6-5.8 (m, H, C***H***=), 4.8-5.0 (m, 2H, =C***H₂***), 3.6-3.8 (m, 2H, S-C***H₂***), 3.2-3.5 ve 2.5-3.0 (m, 4H, C***H***$_2$-N); ^{13}C NMR (125 MHz, *CDCl₃*): δ = 182.2-182.1 (***C***=O), 154.9 (***C***$_{naphthoquinone}$-N), 126.8 (***C***$_{naphthoquinone}$-S), 132.3, 133.0, 134.0 (***C***$_{naphthoquinone}$, ***C***H$_{naphthoquinone}$), 157 (***C***$_{aromatic}$-F), 124.8, 119.7, 116.6, 116.4 (**C**$_{aromatic}$, ***C***H$_{aromatic}$), 37.7 (S-***C***H$_2$), 118.1 (=***C***H$_2$), 51.7 (***C***H$_2$-N); +ESI: *m/z*= 409.15 $[M+H]^+$, *m/z*= 368.15 $[M-(CH_2-CH=CH2)]^+$, $C_{23}H_{21}FN_2O_2S$, (M=408.49 g/mol).

2-(allythio)-3-(4-benzylpiperidine-1-yl)naphthalene-1,4-dione (6)

2-(allythio)-3-(4-benzylpiperidine-1-yl)naphthalene-1,4-dione (6) was synthesized from the reaction of 0.6 g 2-(4-Benzylpiperidine-1-yl)-3-chloronaphthalene-1,4-dione **(5)** and 0.122 g allyl mercaptan to general synthesis procedure.

6: Dark red viscos. 0.123 g (% 18.6). FTIR (ATR):υ (cm^{-1})= 3199 (C-$H_{aromatic}$), 2950, 2905 (C-$H_{aliphatic}$), 1638, 1618 (C=O); ^{1}HNMR (500 MHz, *CDCl₃*): δ = 7.9-8.0 ve 7.5-7.6 (m, 4H, C***H***$_{naphthoquinone}$), 7.0-7.3 (m, 5H, C***H***$_{aromatic}$), 2.0-3.0 ve 1.1-1.4 (m, 10H, 5 C***H***$_2$), 5.6-5.9 (m, H, C***H***=), 4.9-5.2 (m, 2H, =C***H***$_2$), 3.5-3.6 (m, 2H, C***H***$_2$-S); ^{13}C NMR (125 MHz, *CDCl₃*): δ = 179.2 (***C***=O), 143.4 (***C***$_{naphthoquinone}$-N), 132.6, 130.8, 129.8, 128.1, 127.8, 127.2, 125,8 (***C***$_{naphthoquinone}$, ***C***H$_{naphthoquinone}$, ***C***H$_{aromatic}$), 29.3 (***C***H$_{2\ piperidine}$), 41.1 (***C***H$_2$-N), 25.4 (***C***$_{piperidine}$), 37.7 (***C***H$_2$-S); +ESI: *m/z*= 404 $[M+H]^+$, *m/z*= 331$[M-SCH2-CH=CH2]^+$, $C_{25}H_{25}NO_2S$, (403.54 g/mol).

2-(allylthio)-3-(4-chlorophenylamino)naphthalene-1,4-dione (8)

2-(allylthio)-3-(4-chlorophenylamino)naphthalene-1,4-dione **(8)** was synthesized from the reaction of 0.4 g (1.54 mmol) 2-(4-Chlorophenylamino)-3-chloronaphthalene-1,4-dione **(7)** and 0.114 g (1.54 mmol) allyl mercaptan to general synthesis method.

8: Dark red viscos. 0.147 g (% 26.9). FT-IR (ATR):υ (cm^{-1})= 3319 (NH), 3050 ($C_{aromatic}$), 2917, 2849 (C-$H_{aliphatic}$), 1666, 1639 (C=O), 1592, 1551 (C=C); ^{1}HNMR (500 MHz, *CDCl₃*): δ = 7.6-8.1 (m, 4H, C***H***$_{naphthoquinone}$), 6.8-7.3 (m, 4H, C***H***$_{aromatic}$), 5.6-5.7 (m, H, C***H***=), 4.9-5.0 (m, 2H, C***H***$_{2\ allyl}$), 2.0-3.0 (m, 2H, CH_2-S), 4.0-4.1 (m, H, N***H***); ^{13}C NMR (125 MHz, *CDCl₃*): δ = 180, 181 (***C***=O), 137 (***C***$_{naphthoquinone}$-NH), 134.9, 134.4, 131.1, 129.5, 127.6, 123.9, 118.3 (***C***$_{aromatic}$, ***C***H$_{aromatic}$), 145 (***C***$_{aromatic}$-***C***H), 34.9 (S-***C***H$_{2\ allyl}$), 117.2 (***C***H$_{2\ allyl}$=), 133.6 (***C***H$_{allyl}$); +ESI: *m/z*= 356 $[M+H]^+$, 173 $[M-(SCH_2-CH=CH_2)-Ph-Cl]^+$, $C_{19}H_{14}ClNO_2S$, (M=355.84 g/mol).

Results and discussion

In this study, new N,S-substituted naphthoquinone analogues **2, 4, 6** and **8** were obtained from the substitution reaction of previously known N-substituted naphthoquinone compounds 1 (Kalmayer et al., 1991), **3** (Tadashi et al., 1996), **5** (Vanallan et al., 1963) and **7** (Fries et al., 1922) with allyl mercaptan. Due to the chlorine atom in the skeletal structure of the synthesized N-substituted naphthaquinone derivatives, the substitution reaction with allyl mercaptan was easily realized. The synthesized and characterized chemical structures of naphthoquinone analogues are presented in Scheme 1.

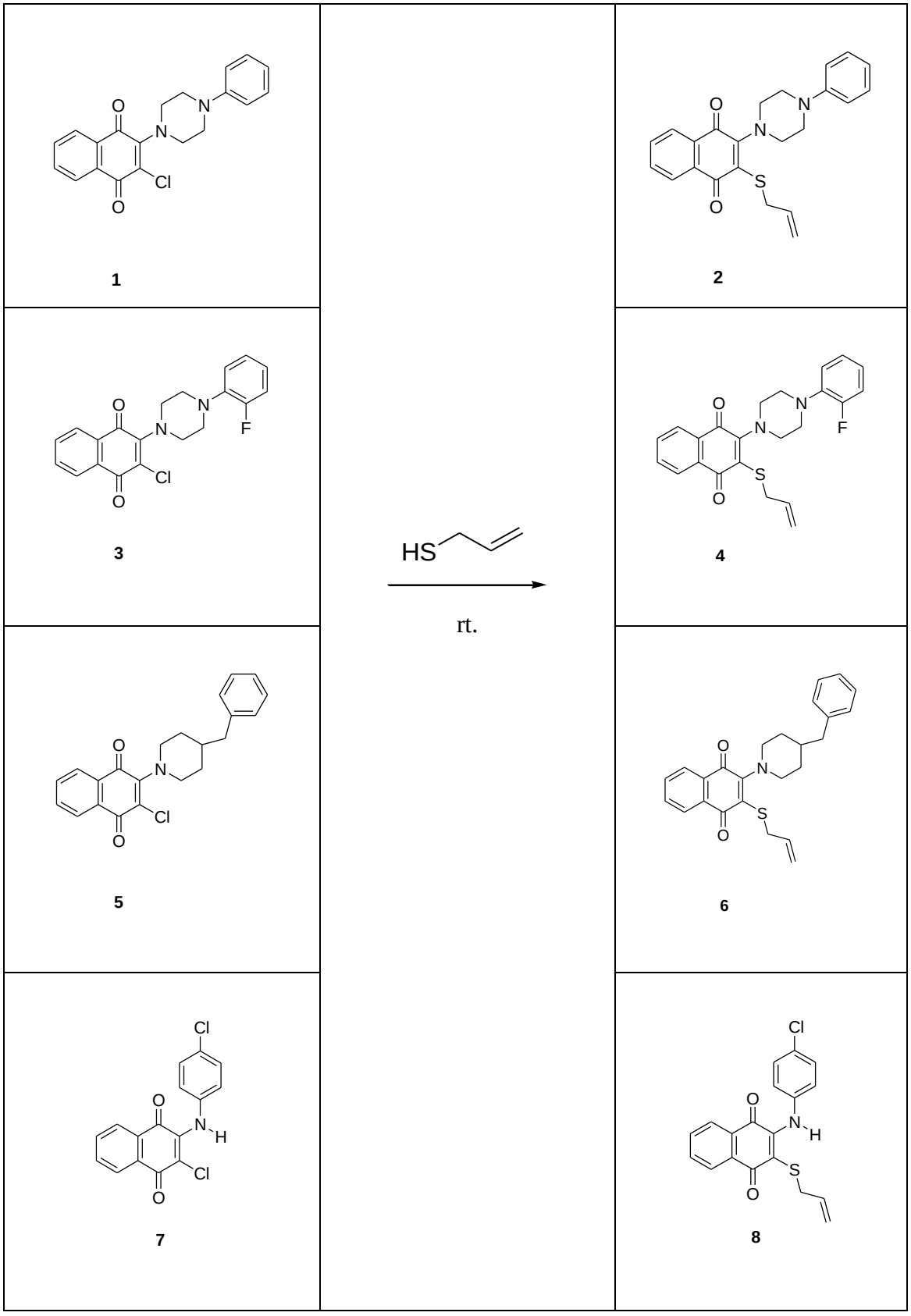

Scheme 1. Synthetic pathway of novel N,S-substituted napthoquinone analogues **(2, 4, 6 and 8).**

In the 1H-NMR spectrum of compound 2, the characteristic (CH=) proton of the allyl group gave a multiplet signal at δ= 5.6-5.8 ppm and (=CH_2) protons gave a multiplet signal at δ= 4.9-5.1 ppm.

Methylene protons in the piperazine ring were observed as multiplet at δ= 3.2-3.7 and δ= 2.4-2.9 ppm (Figure 1).

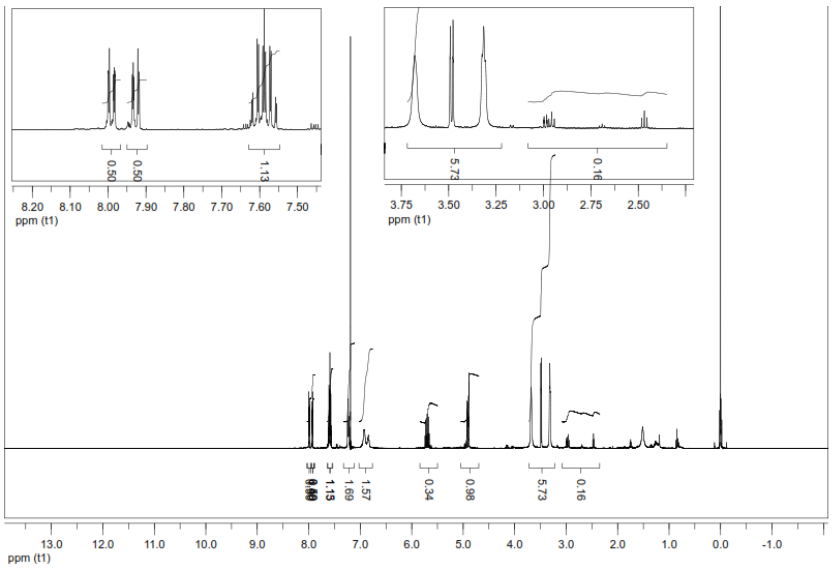

Figure 1. ^{1}H-NMR ($CDCl_3$) spectrum of compound 2.

In the ^{13}C-NMR spectrum of compound 2, the carbonyl carbons in the molecule were observed at δ= 182.1, 181 ppm, the tertiary carbon of the allyl group at δ= 133.9 ppm and the (=CH_2) carbon at δ= 117 ppm. Piperazine methylene carbons were seen at δ= 52.4 ppm and the methylene carbon attached to the sulfur atom was seen at δ= 37.7 ppm. In the mass spectrum of compound 2, *m/z*= 391 $[M+H]^+$ molecular ion and m/z= 350 [M-CH_2-CH_2-CH=CH_2] molecular fragmentation ion was observed with the breakage of the allyl (CH_2-CH=CH_2) group from this molecule (Figure 2).

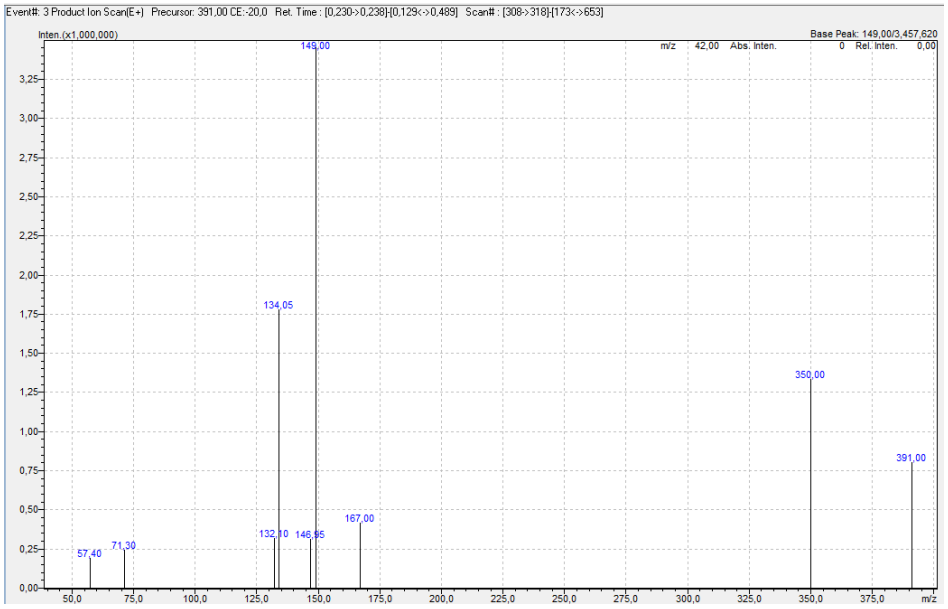

Figure 2. MS spectrum of compound **2.**

In the ^{1}H-NMR spectrum of compound **4**, the aromatic protons of the fluorophenylpiperazine group were multiplet at δ= 6.8-7.0 ppm, the characteristic (CH=) proton of the allyl group was multiplet at δ= 5.6-5.8 ppm and (=CH_2) protons were multiplet at δ= 4.8-5.0 ppm (Figure 3). In the mass spectrum of compound **4**, m/z= 409.15 $[M+H]^+$ molecular ion and m/z= 368.15 [M-CH_2-CH_2-CH=CH_2]$^+$ molecular fragmentation ion was observed with the breakage of the allyl

(CH_2-CH=CH_2) group from this molecule (Figure 4). In the ^{13}C-NMR spectrum of compound **4**, the carbonyl carbons in the molecule were observed at δ= 182.2, 182.1 ppm, the quaternary carbon in the naphthoquinone ring attached to the sulfur atom at δ= 126.8 ppm, the quaternary carbon attached to the piperazine ring at δ= 154.9 ppm, the piperazine methylene carbons at δ= 51.7 ppm and the methylene carbon attached to the sulfur atom at δ= 37.7 ppm. In the mass spectrum of compound **6**, m/z= 404 $[M+H]^+$ molecular ion and m/z= 331 $[M\text{-}SCH_2\text{-}CH_2\text{-}CH{=}CH_2]^+$ molecular fragmentation ion was observed with the breakage of the allylthiol (S-CH_2-CH=CH_2) group from this molecule.

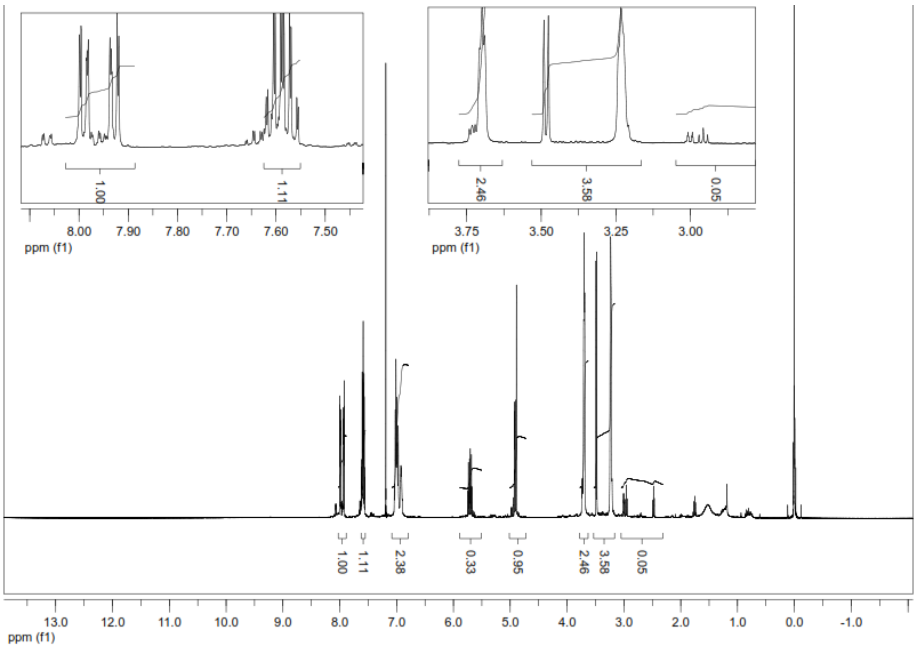

Figure 3. ^{1}H-NMR ($CDCl_3$) spectrum of compound **4.**

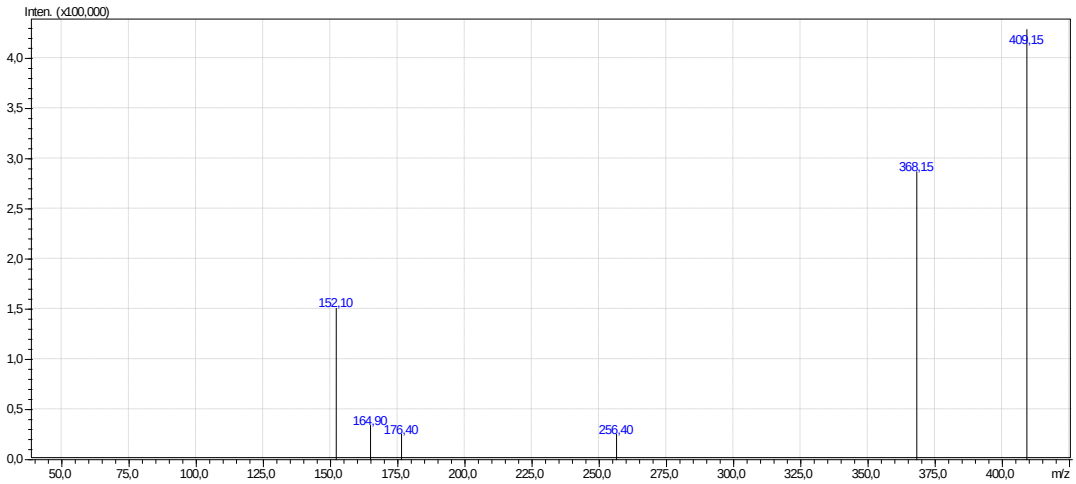

Figure 4. MS spectrum of compound **4.**

In the ^{1}H-NMR spectrum of compound **6**, the aromatic protons in the benzylpiperidine ring gave multiplet signals at δ=7.0-8.0 ppm, the characteristic (CH=) proton of the allyl group gave multiplet signals at δ= 5.6-5.9 ppm and (=CH_2) protons gave multiplet signals at δ= 4.9-5.2 ppm (Figure 5). In the ^{13}C-NMR spectrum of compound **6**, the quaternary carbon in the naphthoquinone ring attached to the nitrogen atom in the molecule was observed at δ= 143.4 ppm, the methylene carbons in the piperidine ring at δ= 29.3 ppm and the quaternary carbon at δ= 25.4 ppm.

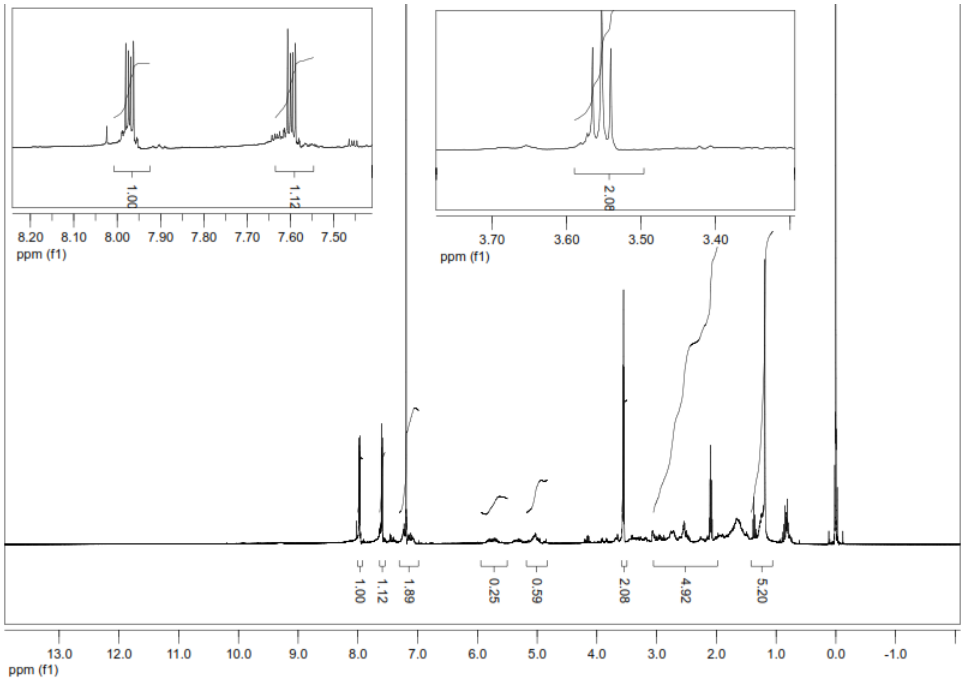

Figure 5. ^{1}H-NMR ($CDCl_3$) spectrum of compound **6.**

In the mass spectrum of compound **8**, *m/z*= 356 $[M+H]^+$ molecular ion was observed (Figure 6). In the ^{1}H-NMR spectrum of compound **8**, aromatic protons in the 4-chlorophenylamino ring were multiplet at δ=6.8-7.3 ppm, the characteristic (CH=) proton of the allyl group was multiplet at δ= 5.6-5.7 ppm, (=CH_2) protons were multiplet at δ= 4.9-5.0 ppm. In the ^{13}C-NMR spectrum of compound **8**, the carbonyl carbons in the molecule were observed at δ= 180, 181 ppm, the quaternary carbon of the naphthoquinone ring attached to the nitrogen atom was observed at δ= 137 ppm and in the FT-IR spectrum of the compound, the characteristic stretching band of the NH group at υ= 3319 cm^{-1} was observed (Figure 7).

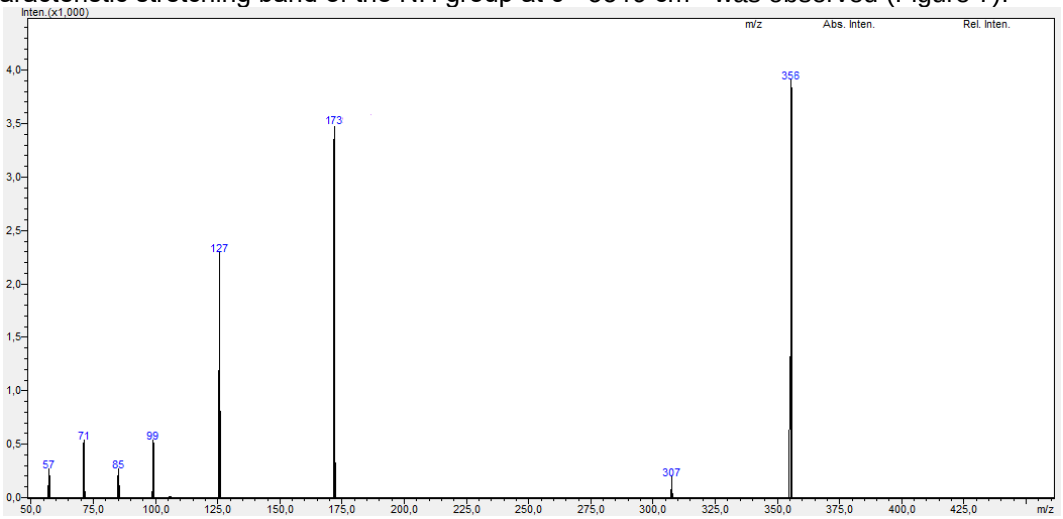

Figure 6. MS spectrum of compound **8.**

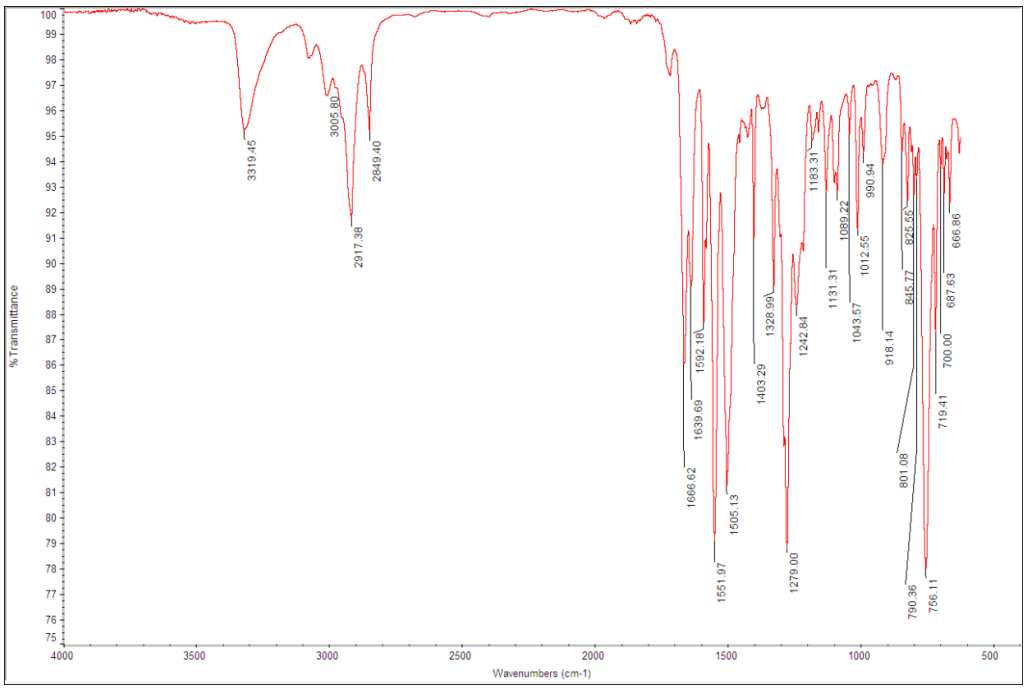

Figure 7. FT-IR spectrum of compound **8.**

Quinones are used in many areas of technology, including as pigments, as drugs, in microbial fuel cells and in supramolecular chemistry. Biosynthetically, quinones can be synthesized in bioreactors and, thanks to their structural richness, they are preferred for industries that use this advantage, for example in the search for new antibiotics, cancer drugs, food colourants and textile dyes (Christiansen et al., 2021). Quinones play a key role as charge storage electrode materials due to their redox centre and integration into the material flow in the biosphere. Effective electrical conductors and quinone-based biomaterials can greatly enhance electrical energy storage systems and technologies. Quinones are used, for example, in the creation of biopolymer energy storage systems using renewable biohybrid electrodes (Ajjan et al., 2019).

Conclusions

The biological activities of natural or synthetic naphthoquinone compounds containing amino and thio groups have been known for many years. The active properties of the naphthoquinone compounds are due to their redox ability. The aim of this study is to synthesize amino- and thiosubstituted naphthoquinone molecules based on previously known aminonaphthoquinone analogues with biological activity. In the structures of the new compounds obtained, there are groups such as amino, thioether, fluorine, chlorine with high biological activity in the literature. We expect that new N,S-substituted naphthoquinone analogues will provide a basis for pharmaceutical chemistry studies.

Funding

The authors would like to express their gratitude to Scientific Research Projects Coordination Unit of Istanbul University-Cerrahpaşa for financial support (Project Numbers: 45266, IUC BAP Project).

Conflict of interest

The authors declare no conflict of interest.

Data availability statement

Data can be obtained from the corresponding author upon a reasonable request.

Ethics committee approval

Ethics committee approval is not required for this study.

Authors' contribution statement

The authors acknowledge their contributions to this paper as follows: Study conception and design: N.O., F.O., H.O.; Data collection: N.O., F.O., H.O.; Analysis and interpretation of results: N.O., F.O., H.O.; Manuscript draft preparation: N.O., F.O., H.O. All authors reviewed the results and approved the final version of the manuscript.

References

Ajjan, F. N., Mecerreyes, D., & Inganäs, O. (2019). Enhancing energy storage devices with biomacromolecules in hybrid electrodes. *Biotechnology journal*, *14*(12), e1900062. https://doi.org/10.1002/biot.201900062

Aziz, M.H., Dreckschmidt, N.E., & Verma, A.K. (2008). Plumbagin, a medicinal plant-derived naphtoquinone, is a novel inhibitor of the growth and invasion of hormone refractory prostate cancer. *Cancer research*, *68*(21), 9024-9032. https://doi.org/10.1158/0008-5472.CAN-08-2494

Borghese, R., Brucale, M., Fortunato, G., Lanzi, M., Mezzi, A., Valle, F., Cavallini, M., & Zannoni D. (2017). Reprint of extracellular production of tellerium nanoparticules by the photosynthetic bacterium Rhodobacter capsulatus. *Journal of hazardous materials*, *324*, 31-38. https://doi.org/10.1016/j.jhazmat.2016.11.002

Christiansen, J. V., Isbrandt, T., Petersen, C., Sondergaard, T. E., Nielsen, M. R., Pedersen, T. B., Sørensen, J. L., Larsen, T. O., & Frisvad, J. C. (2021). Fungal quinones: diversity, producers, and applications of quinones from Aspergillus, Penicillium, Talaromyces, Fusarium, and Arthrinium. *Applied microbiology and biotechnology*, *105*(21-22), 8157–8193. https://doi.org/10.1007/s00253-021-11597-0

Cruz, E.H.G., Hussene, C.M.B., Dias, G.G., Diago, E.B.T., Melo, İ.M.M., Rodrigues, B.L., Silva, M.G., Valenca, W.O., Camera, C.A., Oliverira, R.N., Paiva, V.G., Goulart, M.O.F., Cavalcanti, B.C., Pessoa, C., & Silva, EN. (2014). 1,2,3-triazole-, arylamino- and thio-substituted 1,4-naphthoquinones: potent antitumor activity, electrochemical aspects and bioisosteric replacement of C-ring-modified lapachones. *Bioorganic & medicinal chemistry*, *22*(5), 1608-1619. https://doi.org/10.1016/j.bmc.2014.01.033

Durán, A.G., Chinchilla, N., Simonet, A.M., Gutiérrez, M.T., Bolívar, J., Valdivia, M.M., & Macías, F.A. (2023). Biological Activity of Naphthoquinones Derivatives in the Search of Anticancer Lead Compounds. *Toxins*, *15*(5), 348. https://doi.org/10.3390/toxins15050348

Fries, K., & Kerkow, F. (1922). Uber lineares (Benzo-naptho)-parathiozia, *Justus liebigs annalen der chemie, 427*(2-3), 281-302. https://doi.org/10.1002/jlac.19224270206

Hussain, H., Krohn, K., Ahmad, V.U., Miana, G.A., & Green, I.R. (2007). Lapachol:an overview. *Archive for organic chemistry*, *2*, 145-171. http://dx.doi.org/10.3998/ark.5550190.0008.204

Inagaki, R., Ninomiya, M., Tanoka, K., & Koketsu, M. (2015). Synthesis, characterization and antileukenic properties of naphtoquinone derivatives of lawsone. *ChemMedChem*, *10*(8), 1413-1423. https://doi.org/10.1002/cmdc.201500189

Kalmayer, J.H., & Petesch, N. (1991). Amino quinone reactions 10. Photoreaction of 2-amino-3-chloro-1,4-napthoquinones. *Pharmaceutica acta helvetiae*, *66*,130-136.

Kar, S., Lefterov, I.M., Wang, M., Lazo, J.S., Scott, C.N., Wilcox, C.S., & Carr, B.I. (2003). Binding and inhibition of Cdc25 phosphates by vitamin K analogues. *Biochemistry*, *42*(35), 10490-10497. https://doi.org/10.1021/bi027418p

Kavaliauskas, P., Opazo, F.S., Acevedo, W., Petraitiene, R., Grybaitė, B., Anusevičius, K., & Petraitis, V. (2022). Synthesis, biological activity, and molecular modelling studies of naphthoquinone derivatives as promising anticancer candidates targeting COX-2. *Pharmaceuticals (Basel, Switzerland)*, *15*(5), 541. https://doi.org/10.3390/ph15050541

Liu, Z., Shen, Z., Xiang, S., Sun, Y., Cui, J., & Jia, J. (2023). Evaluation of 1, 4-naphthoquinone derivatives as antibacterial agents: activity and mechanistic studies. *Frontiers of environmental science & engineering*, *17*(3), 31. https://doi.org/10.1007/s11783-023-1631-2

Lopez, L.I., Flores, S.D., Belmares, S.Y., & Galindo, A. (2014). Napthoquinones: Biological properties and synthesis of lawsone and derivatives. *Vitae-revista de la facultad de quimica farmaceutica*, *21*(3), 248-258. ISSNe 2145-2660

López-López, L.I., Rivera-Ávalos, E., Villarreal-Reyes, C., Martínez-Gutiérrez, F., & de Loera, D. (2022). Synthesis and antimicrobial evaluation of amino acid Naphthoquinone derivatives as potential antibacterial agents. *Chemotherapy*, *67*(2), 102-109. https://doi.org/10.1159/000521098

Masi, M., Cimmino, A., Tabanca, N., Beanal, J.J., Bloomquist, J.R., Evidente, A. (2017). A survey of bacterial, fungal and plant metabolites against Aedes aegypti (diptera:culicidae), the vector of yellow and dangue fevers and Zika virus. *Journal of open chemistry*, *15*, 156-166. https://doi.org/10.1515/chem-2017-0019

Nishikawa, Y., Carr, B.I., Wang, M., Kar, S., Finn, F., Dowel, P., Zheng, Z.B., Kernes, J., & Naganathan, S. (1995). Growth inhibition of hepatoma cells induced by K and its analogs. *The Journal of biological chemistry*, *270*(47), 28304–28310. https://doi.org/10.1074/jbc.270.47.28304

Peralta, L.R., Lopez, L.I.L., Belmares, S.Y.S., Cruz, A.Z., Herrara, R.R., & Gonzalez, C.N.A. (2015). Naphthoquinone: Bioactivity and Green Synthesis, The Battle Against Microbial Pathogens: Basic Science, Technological Advances and Educational Programs,In:Vilas,A. M.,Edition: Vol. 1, Formatex Research Center. pp. 542-550.

Riffel, A., Medina, L.F., Stefani, V., Santos, R.C., Bizani, D., & Brandelli, A. (2002). In vitro antimicrobial activity of a new series of 1,4-naphthoquinones. *Brazilian journal of medical and biological research = Revista brasileira de pesquisas medicas e biologicas*, *35*(7), 811–818. https://doi.org/10.1590/s0100-879x2002000700008

Roy, K.M. (2000). Thiols and organic sulfides, ULLMANN'S Encyclopedia of Industrial Chemistry, Vol. 36, Wiley-VCH (Electronic release 2017).

Souza, R.M.C., Pimentel, L.M.L.M., Ferreira, L.K.M., Pereira, V.R.A., Santos, A.C.D.S., Dantas, W.M., & De Oliveira, R.N. (2023). Biological activity of 1, 2, 3-triazole-2-amino-1, 4-naphthoquinone derivatives and their evaluation as therapeutic strategy for malaria control. *European journal of medicinal chemistry*, *255*, 115400. https://doi.org/10.1016/j.ejmech.2023.115400

Tadashi, H., Hiroyuki, G., & Hiroyuki, T. (1996). Preparation of napthoquinones as inflammation inhibitors with cell adhesion inhibiting activity. J.P. 08113555 A19960507, Jpn. Kokai Tokkyo Kaho.

Vanallan, J.A., Reynolds, G.A., & Adel, R.E. (1963). Polynuclear heterocycles IV. The synthesis of some new heterocycles quinones. *The Journal of organic chemistry*, *28*, 524-527. https://doi.org/10.1021/jo01037a066

Vollhardt, P., & Schore, N. (2009). Organic chemistry: structure and function. 6th edition, W.H. Freeman and Company, New York.

EUCHEMBIOJ

THE EUROPEAN CHEMISTRY AND BIOTECHNOLOGY JOURNAL

Eur. Chem. Biotechnol. J. 1: 11-26 (2024) www.euchembioj.com

Research article

Investigation of performance losses in microbial fuel cells with low platinum loadings on air-cathodes

Eda Sonmez[1*] | ORCID 0000-0003-0971-2920 | eda95sonmez@gmail.com

Burcak Avci[2] | ORCID 0000-0002-3595-7852 | avcib@itu.edu.tr

Nourhan Mohamed[2] | ORCID 0000-0001-8184-5299 | norhan.ramadan1@gmail.com

Hakan Bermek[1*] | ORCID 0000-0003-2911-7678 | hbermek@yahoo.com

[1]Department of Molecular Biology and Genetics, Istanbul Technical University, 34469, Maslak, Istanbul, Türkiye

[2]Department of Metallurgical and Materials Engineering, Istanbul Technical University, 34469, Maslak, Istanbul, Türkiye

***Corresponding authors**: eda95sonmez@gmail.com; hbermek@yahoo.com; Ph.: +90-212 285 7301; Fax: +90-212 285 7254.

Received: 10.10.2023
Accepted: 02.12.2023
Published: 02.01.2024

Cite this article: Sonmez, E., Avci, B., Mohamad, N., & Bermek, H. (2024). Investigation of performance losses in microbial fuel cells with low platinum loadings on air-cathodes. *The European chemistry and biotechnology journal*, *1*, 11-26. https://doi.org/10.62063/ecb-14

Abstract

The effect of platinum (Pt) loadings of air-cathodes in the 0-0.5 mg cm^{-2} range on single chamber microbial fuel cell (MFC) performance and cathode impedance was evaluated. In MFC tests, reducing benchmarking Pt loading of 0.5 mg cm^{-2} to 0.1-0 mg cm^{-2} decreased maximum power density by between 38% and 84%. The decrease in cathode open circuit potential with reduced loadings was small down to a catalyst loading of 0.03 mg cm^{-2}, but was significant when the loading was further reduced to 0.01 or 0 mg cm^{-2}. Impedance measurements of cathodes revealed that both charge-transfer and diffusion resistance increase with decreasing catalyst loadings on cathodes. Charge-transfer resistance of benchmarking cathode increased to a small extent when loadings were reduced to 0.1-0.03 mg cm^{-2}. Below 0.03 mg cm^{-2}, dramatic increase of charge-transfer resistance suggested that 0.03 mg cm^{-2} can be considered as the minimum Pt loading for which kinetic limitations are not of great concern and can be overcome to a large extent compared to lower loadings. In comparison to charge-transfer resistance, diffusion resistance differed more significantly between the loadings of 0.03 and 0.5 mg cm^{-2}; and it was therefore the main component that changed the internal resistance of these cathodes.

Keywords: Charge-Transfer Resistance, Diffusion Resistance, Electrochemical Impedance Spectroscopy, Microbial Fuel Cell, Platinum Loading

Introduction

Microbial fuel cells (MFCs), which use microorganisms to convert chemical energy stored in biodegradable substances to electricity represent an emerging clean energy production technology (Rittman et al., 2008). The working principle of an MFC is based on biocatalytic oxidation of the carbon source at the anode and a reduction reaction of an electron acceptor at the cathode; where oxygen, potassium ferricyanide/permanganate/dichromate and ferric chloride have been used as electron acceptors so far (Oh et al., 2004; You et al., 2006; Wei et al., 2012; Kumar et al., 2017; Ucar et al., 2017). Among them, the use of oxygen has been the most common in recent years due to its sustainability and renewability compared to the others, while single chamber designs with air-cathodes further simplified MFC operation by allowing passive oxygen transfer and eliminating the need for aeration of aqueous cathodes used in double chamber systems (Liu and Logan, 2004). When oxygen is employed as a cathodic electron acceptor, low kinetic rate of oxygen reduction reaction (ORR) occurring at the surface of carbon or graphite electrodes necessitates the use of an electrocatalyst to lower the activation energy barrier and increase the current output of MFCs (Rismani-Yazdi et al., 2008). Platinum (Pt), which is a widely used cathode catalyst in the form of nanoparticles dispersed on a carbon support (Pt/C) for MFC studies, is considered to have the highest catalytic activity towards ORR among metals based on the calculations of O_2- , O- and OH- binding energies (Lima et al., 2007; Wang et al., 2014;). However, as an expensive noble metal, the use of Pt in cathodes has been reported to account for approximately 50% of the total cost of lab-scale MFCs, making this electrocatalyst economically non-viable, especially for targeted large-scale wastewater treatment applications (Rozendal et al., 2008). Although some efforts have been made to completely replace Pt catalyst with metal oxides (Xia et al., 2018; Majidi et al., 2019; Ayyaru et al., 2019), metal-nitrogen-carbon complexes (Lu et al., 2016; Yang and Logan, 2016; Tang and Ng, 2017), and metal-free carbon materials (Feng et al., 2011; Liu et al., 2015); reported maximum power densities were either lower than achieved with Pt/C cathode at the same catalyst loading (Feng et al., 2011; Majidi et al., 2019; Ayyaru et al., 2019) or higher than obtained with Pt/C cathode but required higher loadings of alternative catalysts than typical benchmarking loading of Pt (0.5 mg cm^{-2}) (Liu et al., 2015; Xia et al., 2018). Therefore, if the criterion of catalyst loading is considered along with maximum power density, Pt can be still regarded as the best performing catalyst material in the majority of the studies and reducing its use to lower loadings on cathodes without significant loss in performance might be another suitable approach to decrease MFC costs.

Previously, the effect of reduced Pt loadings on performance has been examined by several studies in MFC literature in different aspects. Cheng et al. performed chronopotentiometry to air-cathodes with Pt loadings ranging from 0.1 to 2 mg cm^{-2} and reported a potential difference less than 10-20 mV for all samples with respect to 0.5 mg Pt cm^{-2} cathode when Nafion was used as the binder material. They also found a 19% decrease in maximum power density of MFC when Pt loading was reduced from 0.5 to 0.1 mg cm^{-2} (Cheng et al., 2006). In the work of Mateo et al., maximum current density and power density from polarization data were strongly dependent on Pt loading of cathodes ranging from 0.25 to 2 mg cm^{-2}, however open circuit voltages (OCVs) and treatment capacity of MFCs with a synthetic wastewater did not differ significantly (Mateo et al., 2017). Santoro et al. tested the time-dependence of power densities obtained throughout an operational period of 8 days in MFCs with a wider range of Pt loadings on cathodes (0.005-1 mg cm^{-2}) and they showed that difference between power densities achieved with high (1 and 0.5 mg cm^{-2}) and lower Pt loadings became smaller over this period (Santoro et al., 2013). Although these studies provide useful information about losses in some performance indicators related to MFC operation for their own experimental conditions; they lack a quantitative analysis of electrochemical processes occurring at the cathode which limit the power outputs of MFCs when catalyst loadings are reduced. In this context, determining individual sources of internal resistance of cathodes can help to better understand the effect of cathode structure with reduced Pt loadings on overall MFC performance and to design more effective electrodes with such low catalyst loadings accordingly. Electrochemical impedance spectroscopy (EIS), which is a powerful electrochemical technique for characterization of fuel cells/electrodes, can be used to determine ohmic, charge transfer and diffusion resistance constituting three main components of internal resistance; for which contribution of these processes to voltage losses are not distinguishable in the more commonly used polarization curve method (Yuan et al., 2007). In spite of higher charge transfer resistances expected for cathodes with reduced Pt loadings, the extent of these increases in charge

transfer resistance and the effect of catalyst loading on the other resistances related to ohmic and diffusion processes, if exists, remain unknown.

In this study, air-cathodes with Pt loadings ranging from 0.01 to 0.5 mg cm^{-2} were prepared by a conventional ink-based method. Performance of single chamber MFCs with different cathodes was investigated in terms of polarization behaviour, maximum power density and Coulombic efficiency. To give insight into changes in the internal resistance compositions of cathodes when Pt loading was reduced, EIS was performed on polarized cathodes.

Materials and methods

Electrodes

Anodes and cathodes of MFCs were non-wet proofed and wet proofed carbon clothes (BASF Fuel Cell Inc.), respectively. Anodes were used as purchased without any treatment whereas the air side of the cathodes were coated to have one carbon base layer and four additional PTFE diffusion layers, as described previously (Cheng et al., 2006). To produce the catalyst layer on the solution-facing side of the carbon cloth cathodes, a catalyst ink with a density of 87.5 mg Pt/C mL^{-1} was prepared by thoroughly mixing Pt/C catalyst (20 wt.% Platinum on Vulcan XC-72R, BASF), Nafion ionomer solution (5 wt.%, Sigma-Aldrich), isopropyl alcohol and water. To achieve 0.5 mg Pt cm^{-2} loading on the cathode, corresponding volume of the starting ink was directly pipetted onto carbon cloth for brush coating. For lower loadings, corresponding volumes of the starting ink were pipetted into separate tubes and further diluted with isopropyl alcohol and water to make the resulting inks applicable to the carbon cloth substrate for brush coating. The weight ratio of the ionomer (dry) to Pt/C catalyst was 3:7 in all cathodes and the volume ratio of the solvents (water and isopropyl alcohol) was 1:1 in all the inks prepared. The amount of Pt on cathodes was verified by weighting the cathodes before the coating and after the end of the drying process at room temperature (24 hours). Tested Pt loadings were 0.5 mg Pt cm^{-2}, 0.1 mg Pt cm^{-2}, 0.05 mg Pt cm^{-2}, 0.03 mg Pt cm^{-2} and 0.01 mg Pt cm^{-2}. A cathode with a carbon base layer and diffusion layers on the air side but without catalyst loading on the solution side was also prepared as a negative control sample.

Construction, acclimation and operation of MFCs

Six membrane-less air-cathode MFCs were constructed from 12 mL plexiglass cube-shaped reactors in which anodes and cathodes were placed in opposite sides of the reactor chamber. The surface area of both anodes and cathodes was 7 cm^2. MFCs were operated in batch mode and with an external resistance of 1 kΩ except during polarization measurements. Before testing cathodes with different platinum loadings in MFCs, anodes were colonized with activated sludge as starting inoculum and sodium acetate medium solution which contained 1 g sodium acetate, 0.31 g NH_4Cl, 0.13 g KCl, 4.54 g $NaH_2PO_4.H_2O$, 2.44 g Na_2HPO_4, 12.5 mL mineral and 12.5 mL vitamin solution per liter (Lovley and Phillips, 1988). Colonization of anodes was started by adding inoculum and sodium acetate medium to the reactors in a 1:1 volume ratio until voltage outputs exceeded 100 mV and continued by adding only medium solution afterwards. During this acclimation period, all six cathodes were identical carbon cloths with 0.5 mg Pt cm^{-2} catalyst loading to ensure uniform conditions in all reactors. Anodes were considered acclimated when reproducible voltage outputs were obtained from at least 3 batch cycles. At this point, cathodes were changed with newly fabricated cathodes with different Pt loadings.

Analysis

Voltage generation of the MFCs was monitored at 10 min intervals using a digital multimeter with a data acquisition system (Pico Technology). Current (I= V/R) and power (P= I.V) were calculated based on Ohm's law and normalized to the cathode projected surface area. Polarization data were obtained by multiple cycle method (Watson and Logan, 2011), in which the resistors of MFC circuits were changed from 1 kΩ to 100 Ω and each resistor was used during complete batch cycles (triplicate). 3-hour of maximum steady-state period of voltage vs. time graphs was used to average voltage, current and power values. Columbic efficiency (CE) was calculated as the ratio of actual Coulombs obtained to the theoretical amount of Coulombs that can be obtained from the substrate during a batch cycle, by integrating current over time and using the formula

$$CE = \frac{M \int_0^t I dt}{FbSv} \quad (1)$$

where *F* is Faraday's constant (*F*=96 485 C mol^{-1}), *b* is the number of moles of electrons produced per mole of acetate (*b*= 8), S is substrate concentration (*S*=1 g L^{-1}), *v* is the liquid volume (*v*=0.012 L) and *M* is the molecular weight of sodium acetate (*M*= 82 g mol^{-1}) (Liu et al., 2005).

Electrochemical impedance spectroscopy

Electrochemical impedance spectroscopy (EIS) was performed on cathodes by using a 3-electrode setup which consisted of cathode as the working electrode, anode as the counter electrode and an Ag/AgCl reference electrode (+197 mV vs. SHE). Measurements were conducted in potentiostatic mode over a frequency range of 100 kHz to 5 mHz with an AC signal of 10 mV amplitude and data registration of 10 points per decade by using a potentiostat (Bio-Logic Science Instruments). Before the impedance measurements, the working electrode was stabilized at open circuit potential (OCP) and then the potential to be applied for EIS was set for 30 minutes. Cathode potentials were set to -0.2 V vs. Ag/AgCl with an aim to observe the effects of both kinetic and diffusion processes in the spectra; for which the applied potential was assumed to provide suitable polarized conditions for cathodes based on measured cathode OCP values. Additional measurements were taken at less polarized conditions on some samples to evaluate the potential dependence of the impedance behaviour. EIS data were analysed with EC-Lab software by fitting the spectra with equivalent circuits shown according to the flooded-agglomerate model of gas diffusion electrodes (Zhang et al., 2011; Springer and Raistrick, 1989). In both circuits, constant phase elements (CPEs) were used to represent non-ideal behaviour of capacitors due to non-homogeneous surface roughness, coating and reaction rate distribution on electrodes (He and Mansfeld, 2009). Impedance of a CPE is mathematically expressed as follows:

$$Z_{CPE} = Q^{-1}.\ (j2\pi f)^{-a} \qquad (2)$$

where *j* is the imaginary unit ($j^2 = -1$), *Q* is pseudo-capacitance ($\Omega^{-1}\ s^a$ or $F\ s^{a-1}$), *f* is frequency (Hz) and *a* is CPE exponent (Dominguez-Benetton et al., 2012). For the cathodes whose Nyquist impedance plots showed 2 clear loops, the equivalent circuit with two time constants in Figure 1a was used to determine the values of electrochemical components; namely R_Ω for ohmic resistance, R_{ct} for charge transfer resistance in parallel with CPE_1 for the kinetic process and R_d for diffusion resistance in parallel with CPE_2 for a diffusional process. For the cathodes which showed a single apparent loop in Nyquist plots, the equivalent circuit with one time constant in Figure 1b which consisted of serial connection of R_Ω with a parallel combination of polarization resistance R_p and CPE was used; where R_p was suggested as the sum of charge transfer and diffusion resistance ($R_p = R_{ct}+R_d$). To avoid complications of high frequency artefacts resulting from experimental setup, typically observed for all samples in this study, data fitting was performed between 1.5 kHz and 5 mHz. Values of $\chi^2/|Z|$ were reported to represent the goodness of the fit of the equivalent circuits with data.

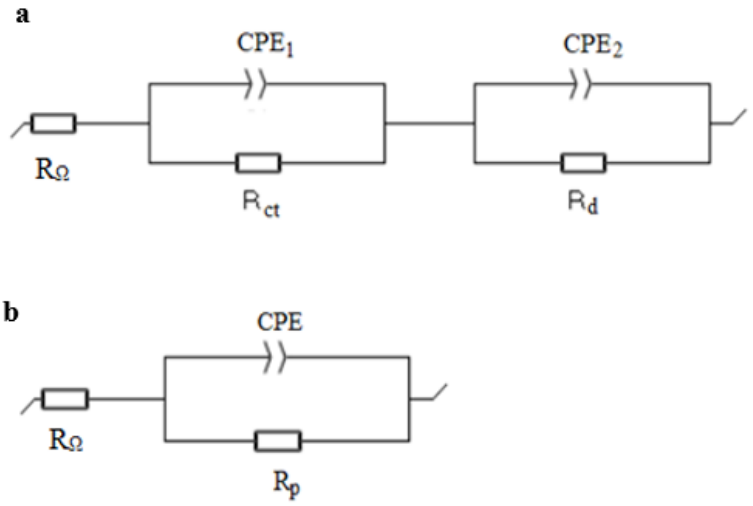

Figure 1. Equivalent circuits used to fit impedance data which shows **a)** two loops **b)** one loop in Nyquist plots.

Results and discussion

Voltage generation

After acclimating bacteria in MFCs and ensuring similar performances for anodes based on comparable voltage outputs with the same type of cathodes in all reactors; cathodes were replaced with newly fabricated ones having different Pt loadings and stable voltage generation with new electrodes was confirmed. Figure 2a and 2b show 3 successive cycles of voltage production in MFCs at 1 kΩ, indicating reproducible power generation of MFCs with each cathode. The maximum voltage of 456 ± 5 mV produced by MFC with cathode of highest Pt loading in this study (0.5 mg Pt cm^{-2}) decreased to 343 ± 4 mV, 263 ± 3 mV and 211 mV ± 3 when loading was reduced to 0.1, 0.05 and 0.03 mg Pt cm^{-2}, respectively. The maximum voltage obtained with a minimal catalyst loading on cathode (0.01 mg Pt cm^{-2}, 162 ± 2mV) was only slightly higher than that obtained with bare cathode (154 ± 1 mV). Durations of voltage cycles ranged from ~22 hours to 30 hours and they did not show a clear relationship with cathode catalyst loading.

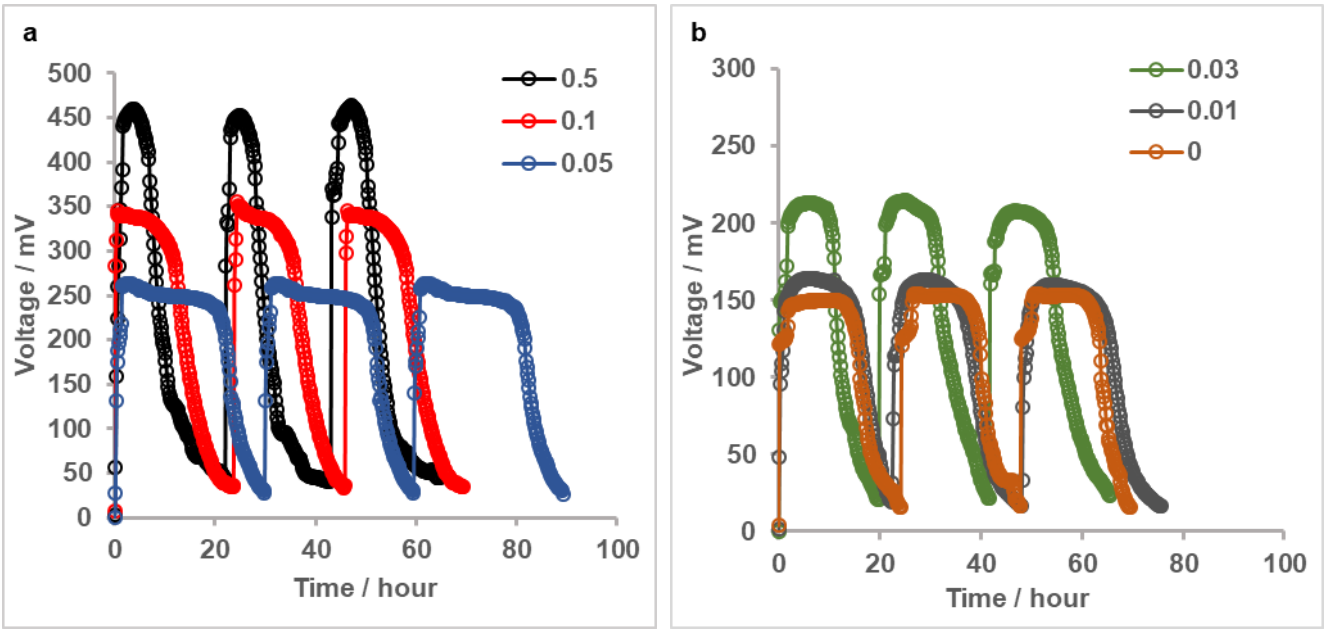

Figure 2. Reproducible voltage generation of MFCs with **a)** 0.5, 0.1 and 0.05 mg Pt cm^{-2} cathodes **b)** 0.03, 0.01 and 0 mg Pt cm^{-2} cathodes at 1 kΩ.

Voltage losses and power densities of MFCs

The performance of the MFCs having different catalyst loadings on cathodes were evaluated in terms of their polarization behaviour and generated power densities. At open circuit conditions, cell voltage decreased with decreasing Pt loadings on cathodes and were in 736-762 mV range for the MFCs with 0.03 to 0.5 mg Pt cm^{-2} cathodes and much lower for the MFCs with 0.01 mg Pt cm^{-2} and bare cathodes (611 and 602 mV, respectively). Measurement of the open circuit potentials (OCPs) of the cathodes individually with a reference electrode showed that OCP of the 0.5 mg Pt cm^{-2} cathode slightly decreased from 560 mV to 541-531 mV vs. SHE with decreasing loadings down to 0.03 mg Pt cm^{-2}; and then to ~ 397 and 387 mV vs. SHE for the 0.01 mg Pt cm^{-2} and zero loadings. This indicated that OCPs of the anodes were close in all MFCs and differences in the cell voltage at zero current were due to different cathode OCPs.

The polarization curves of MFCs showed that overpotentials of the cells with bare and 0.01 mg Pt cm^{-2} loaded cathodes were comparable up to a current density of ~ 0.35 A m^{-2} and at ~ 0.55 A m^{-2}, whereas they differed in the 0.35-0.55 A m^{-2} range (Figure 3a). For MFCs having higher catalyst loading on cathodes (0.03, 0.05, 0.1 and 0.5 mg Pt cm^{-2}), overpotential was increased with decreasing catalyst loadings in the entire range of current densities. The maximum power density obtained in MFC with the cathode of the highest Pt loading in this study (0.5 mg Pt cm^{-2}) was 303 ± 11 mW m^{-2} (Figure 3b). When the catalyst loading of cathode was reduced to 0.1 mg Pt cm^{-2}, MFC generated a power density of 189 ± 5 mW m^{-2}, showing a 38% decrease compared to that generated with 0.5 mg Pt cm^{-2} cathode. Further reducing Pt loading on cathodes decreased maximum power density by 62% for 0.05 mg cm^{-2} (115 ± 8 mW m^{-2}), 75% for 0.03 mg cm^{-2} (76 ± 7 mW m^{-2}) and 80% for 0.01 mg cm^{-2} (59 ± 3 mW m^{-2}) cathodes. The maximum power density of MFC obtained without catalyst on cathode (48 ± 1 mW m^{-2}) was approximately one sixth of that obtained with the highest Pt loading on cathode and slightly lower than that of MFC with 0.01 mg Pt cm^{-2} cathode. These results suggested that reducing the catalyst loading of 0.5 mg Pt cm^{-2} by a factor of 5 or more significantly affected MFC performance in terms of voltage losses and maximum power density; and even with the closest Pt loading of 0.1 mg cm^{-2} to this benchmarking cathode, difference in overvoltages and maximum power densities was notable.

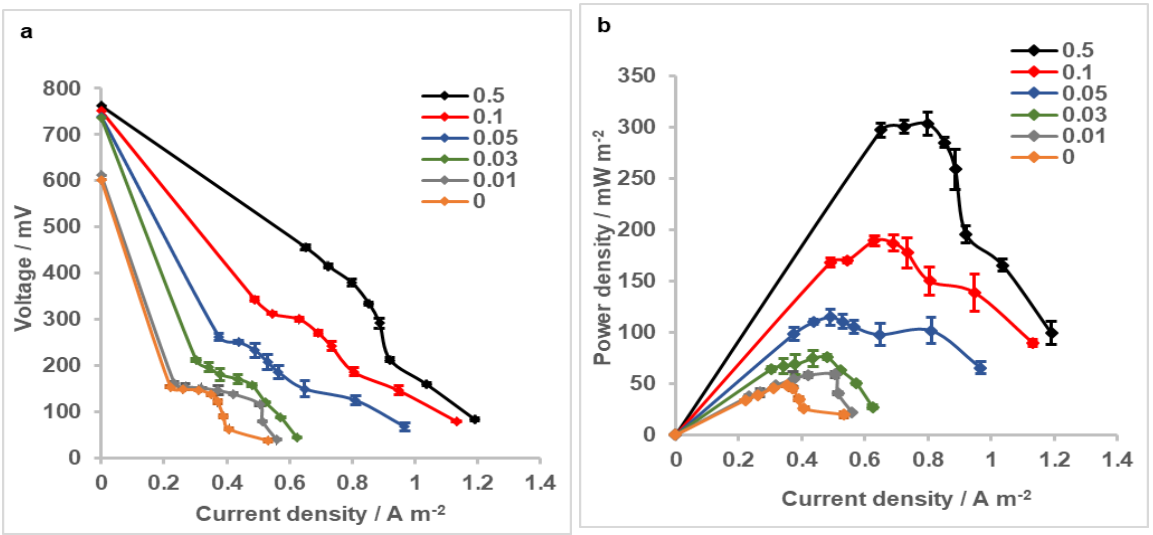

Figure 3. a) Polarization and **b)** power density curves of MFCs with cathodes having different Pt loadings. Error bars represent standard deviations based on triplicate measurements.

Coulombic efficiencies of MFCs

Coulombic efficiencies (CEs) of MFCs with different cathodes were calculated for the entire current density range measured in polarization tests to evaluate the effect of Pt loading on this performance indicator. For each MFC, CE was increased with increasing current density (Figure 4). CE range of MFC with 0.5 mg Pt cm^{-2} cathode was between ~15% and 33% whereas it was slightly different for MFCs with 0.1 mg Pt cm^{-2} and 0.05 mg Pt cm^{-2} cathodes (17-33% and 18-32%, respectively). However, at a given current density; CE of MFC with 0.05 mg Pt cm^{-2} cathode was higher than other two, possibly resulted from longer batch cycle durations for this MFC compared to the others. When the Pt loading on cathodes was further reduced; CEs for MFCs varied from 10% to 20% for 0.03 mg Pt cm^{-2}, from 9% to %20 for 0.01 mg Pt cm^{-2} and from 9% to 17% for bare cathodes. These CEs were comparable on the basis of both quantity and corresponding current density, unlike MFCs of cathodes with higher Pt loadings.

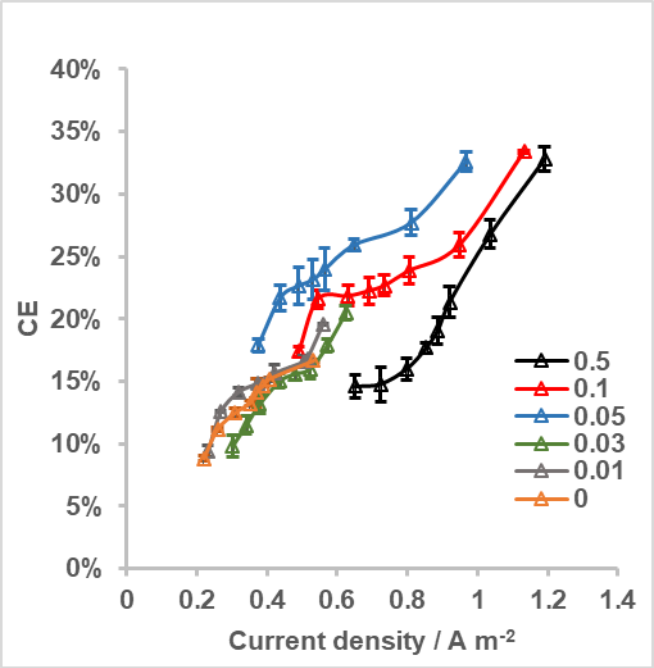

Figure 4. CE as a function of current density for MFCs with cathodes having different Pt loadings. Error bars represent standard deviations based on triplicate measurements.

Impedance of the cathodes with different Pt loadings

EIS was performed on cathodes with different Pt loadings at polarized conditions. At a cathode potential of -0.2 V vs. Ag/AgCl, Nyquist impedance plots showed that the total internal resistance of cathodes decreased with increasing Pt loadings; inferred from decreasing resistances in the low frequency region of the spectra (Figure 5a and 5b). Complex plane impedance plots of cathodes with 0, 0.01 and 0.03 mg Pt cm^{-2} consisted of two well separated semi circles, which could be attributed to charge transfer and diffusion processes (Figure 5a); whereas plots of cathodes with higher loadings (0.05, 0,1 ,0.5 mg cm^{-2}) showed a single loop in which charge transfer and diffusion regions were indistinguishable at first glance. In additional experiments with higher applied potentials to these cathodes (0.1 mg Pt cm^{-2} cathode is given as an example in Figure 6), it was observed that arcs in the impedance spectra converged to larger semi-circles with increasing potentials; indicating that it is both possible for these samples to be found in kinetic-controlled or kinetic/diffusion mixed controlled region when the set potential was -0.2 V. We therefore referred to the semi-circles of the spectra in Figure 5b to as polarization resistance (R_p), in which contributions of charge or mass transfer remained unknown until a second mathematical analysis of the data. A more detailed analysis of impedance spectra for the cathodes with these 3 highest loadings is discussed below.

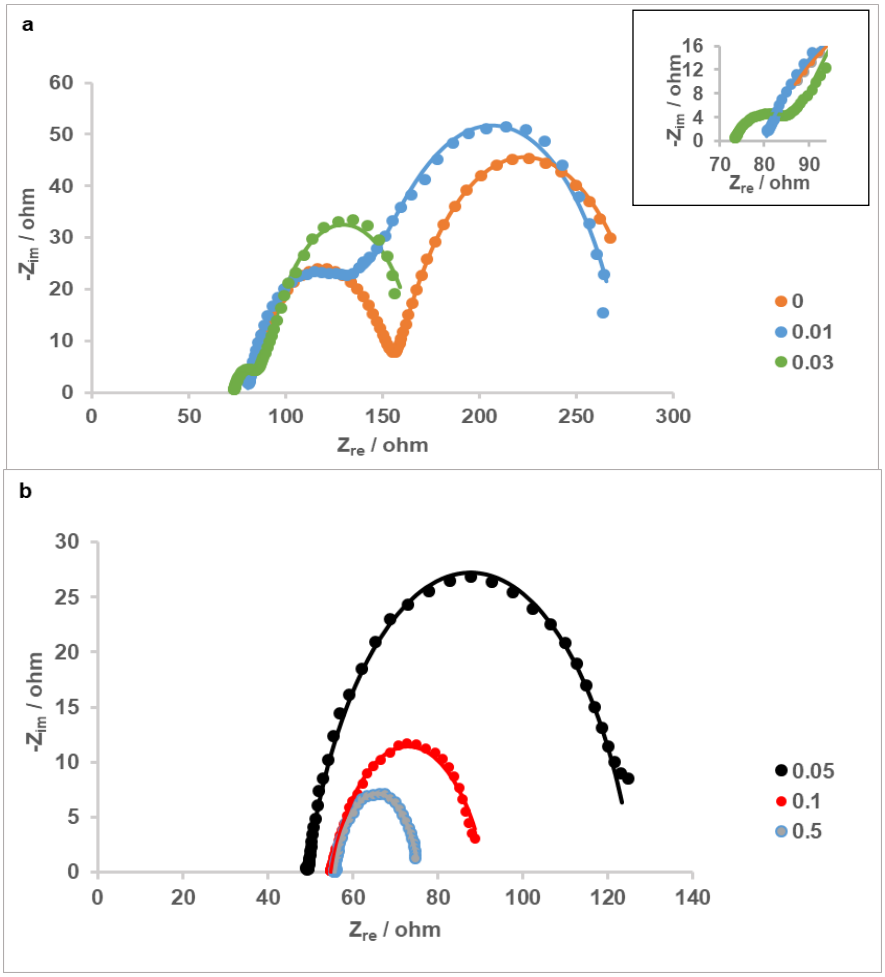

Figure 5. Nyquist plots of cathodes with **a)** 0, 0.01, and 0.03 mg Pt cm^{-2} loadings **b)** 0.05, 0.1 and 0.5 mg Pt cm^{-2} loadings. Symbols and lines represent experimental data and data obtained by fitting the spectra with equivalent circuits, respectively.

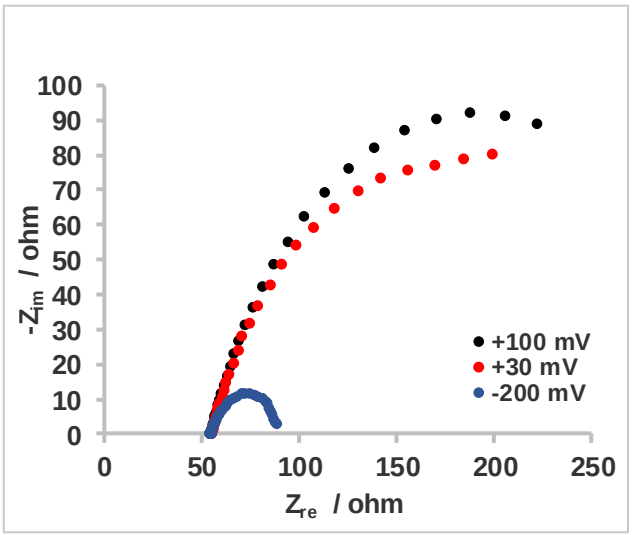

Figure 6. Potential dependence of impedance of the cathode with 0.1 mg Pt cm^{-2} loading.

Loading of the cathode with the lowest amount of Pt/C in this study (0.01 mg Pt cm^{-2}) decreased the charge transfer resistance of the bare cathode by ~ 13 Ω whereas diffusion resistances of these cathodes differed very little (Figure 5a, Table 1), suggesting that the presence of this minimal catalyst

loading affected ORR kinetics but did not cause a significant change in the cathode structure which is related to diffusion process. When the catalyst loading was 0.03 mg Pt cm^{-2}, the reduction of R_{ct} and R_d with respect to bare cathode was more pronounced as these were decreased by 57.45 Ω and 54.74 Ω, respectively. Polarization resistance (R_p) for cathodes with 0.05, 0.1 and 0.5 mg Pt cm^{-2} were decreased with increasing catalyst loading and they were all smaller than the sum of R_{ct} and R_d calculated for cathodes having less catalyst content.

Despite the use of the same solution and cell configuration for all samples during EIS experiments, ohmic resistance measured between working and reference electrode differed for cathodes. $R_Ω$, which was similar and between 80-80.5 Ω for the cathodes without catalyst loading and with 0.01 Pt cm^{-2}; first decreased to 72.4 Ω with 0.03 mg Pt cm^{-2} and then to 49.5-55.8 Ω range with higher loadings (Table 1).

A more detailed examination of the apparent loops in Nyquist plots for cathodes with 0.05, 0.1 and 0.5 mg Pt cm^{-2} loadings (Figure 5b) revealed that the arcs constituting these loops were not perfectly symmetrical. This situation was especially evident in the cathode with 0.1 mg Pt cm^{-2} and brought out the possibility of the presence of two relatively close time constants corresponding to charge transfer and diffusion processes in Nyquist plots. With an attempt to mathematically solve these individual contributions to R_p of these cathodes, we first estimated the starting values for diameters of charge transfer and mass transfer semi-circles for the 0.1 mg Pt cm^{-2} cathode sample, based on characteristic frequencies of these two time constants and the x-axis intercepts to which high and low frequency arcs converged. By using the equivalent circuit in Figure 1a for the fitting process, we obtained the values for electrochemical components and used them as starting values to fit the spectra of the other cathodes with 0.05 and 0.5 mg Pt cm^{-2}. Following this procedure, we were able to obtain the values for R_{ct}, R_d and their corresponding CPE parameters; while the goodness of the fits with the newly used circuit was improved as compared to the previous one for 0.05 and 0.1 mg Pt cm^{-2} cathodes (Table 1). According to this fitting model, cathodes showed a decrease in both R_{ct} and R_d between 3 samples with increasing loadings and these results were consistent with those of the other cathodes (0, 0.01 and 0.03 mg Pt cm^{-2}), as the addition of more catalyst yielded an overall decrease in charge transfer and diffusion resistances.

Distribution of resistive components of the individual cathodes is shown in Figure 7, in which fitting parameters obtained with both equivalent circuits for 0.05, 0.1 and 0.5 mg Pt cm^{-2} cathodes are given for clarity. For the cathodes with zero and 0.01 mg Pt cm^{-2} loadings, the major contributor to the internal resistance was diffusion resistance, which accounted for 46% and 48% of the total resistance, respectively. Loading with a minimal amount of catalyst decreased the charge transfer contribution of the negative control sample from 28% to only 23%, whereas ohmic and charge transfer percentages were close in both cathodes. With the 0.03 mg Pt cm^{-2} cathode, a dramatic decrease of the charge transfer contribution to 11% was found and from this loading on, the ratio of charge transfer resistance to internal resistance remained between 9-15%; which was the smallest among those of other components. While the 0.03 mg Pt cm^{-2} cathode had nearly equal contributions from ohmic and diffusion resistances, diffusion resistance percentages were reduced with increasing loadings from this point and eventually the internal resistance became ohmic-dominant for the cathodes with highest loadings (0.1 and 0.5 mg Pt cm^{-2}). These findings indicated that 0.03 mg Pt cm^{-2} loading might be regarded as a turning point for which charge transfer resistances due to ORR kinetics contribute to the internal resistance to a much smaller extent than below this loading and this contribution changes relatively little for higher loadings. However, high diffusion resistance is still valid for 0.03 mg Pt cm^{-2} cathode and is the major cause for the difference between its resistance distribution profile and those of the cathodes with higher Pt loadings. For the cathodes whose impedance spectra were modelled by using the equivalent circuit in Figure 1b, the contribution of polarization resistance to internal resistance decreased from 61% to 40% and 26% as the Pt loading was increased.

Table 1: Values of electrical elements extracted by fitting EIS data of cathodes having different Pt loadings with equivalent circuits. . For 0.05, 0.1, and 0.5 mg Pt cm^{-2} cathodes, rows with and without (*) symbol show fitting results obtained by using equivalent circuit in Figure 1a and Figure 1b, respectively. For the other cathode samples, given parameters correspond to those obtained by using equivalent circuit in Figure 1a. $\chi^2/|Z|$ values represent the goodness of the fit.

Pt loading (mg cm^{-2})	R_Ω (Ω)	R_{ct} (Ω)	Q_2 (mF $s^{(a2-1)}$)	*a2*	R_d (Ω)	Q_3 (mF $s^{(a3-1)}$)	*a3*	R_p (Ω)	Q_4 (mF $s^{(a4-1)}$)	*a4*	$\chi^2/\|Z\|$
0	80.52	76.13	0.14	0.712	133.8	34	0.76	-	-	-	3.48E-03
0.01	80.14	63.12	1.482	0.741	132.5	24	0.821	-	-	-	3.11E-03
0.03	72.39	18.68	6.673	0.539	79.06	80	0.867	-	-	-	2.79E-03
0.05	49.24	-	-	-	-	-	-	77	18	0.783	3.09E-03
0.1	54.85	-	-	-	-	-	-	36.39	43	0.715	8.76E-04
0.5	55.76	-	-	-	-	-	-	19.83	54	0.798	1.72E-04
0.05*	49.47	15.98	42	0.942	61.71	28	0.770	-	-	-	1.29E-03
0.1*	54.74	13.83	67	0.646	21.71	97	0.825	-	-	-	3.64E-04
0.5*	55.8	6.846	69	0.855	12.39	125	0.9	-	-	-	3.84E-04

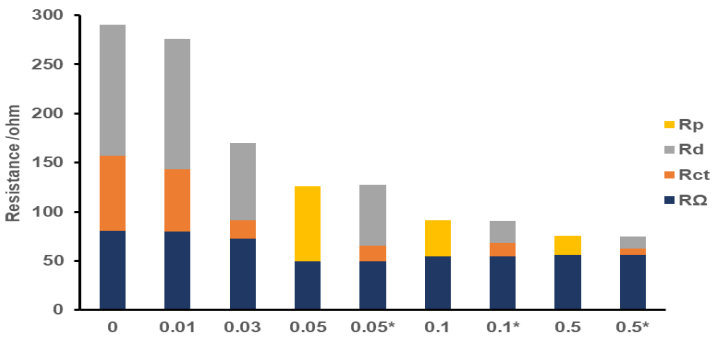

Figure 7. Internal resistance of cathodes having 0-0.5 mg Pt cm^{-2} loadings in terms of ohmic resistance (R_Ω), charge-transfer resistance (R_{ct}), diffusion resistance (R_d) and polarization resistance (R_p). Symbol of (*) indicates cathode samples whose EIS data were analysed according to the equivalent circuit with 2 time constants in Figure 1a.

ORR is proposed to occur by a direct 4 electron transfer or an indirect 2 electron transfer mechanism per molecule of O_2 consumed at the cathode. Corresponding redox potential of the half-cell reaction with $4e^-$ transfer is 815 mV vs. SHE, whereas it ranges from 267 to 337 mV vs. SHE for $2e^-$ transfer mechanism depending on the formation of H_2O_2, OH^- or HO_2^- at pH 7 and 25 ^oC (Rossi et al., 2019). OCP of the cathode with the highest Pt loading in this study (0.5 mg cm^{-2}) was 560 mV vs. SHE. Although this potential was still far from the thermodynamically predicted value for ORR through $4e^-$ transfer, it was consistent with OCPs reported for in-house prepared and commercial gas diffusion cathodes with the same Pt loading (HaoYu et al., 2007). A non-negligible difference between theoretical and observed cathode potential at equilibrium is usually observed in MFCs (Logan and Regan, 2006), and explained by the formation of a mixed potential at the cathode due to substrate crossover from anode. These crossover effects are expected to be stronger in separator-free reactors like those in current study and Pt catalyst, in particular, has been shown to be susceptible to them earlier (Harnisch et al., 2009). The decrease in the cathode OCP with reduced Pt loadings was small down to a catalyst loading of 0.03 mg Pt cm^{-2} (a maximum difference of 29 mV between 0.5 and 0.03 mg Pt cm^{-2} cathode samples), but was significant when the loading was further reduced to 0.01 mg Pt cm^{-2} or zero, yielding 397 and 387 mV vs. SHE, respectively. These lower OCPs of the 0.01 mg Pt cm^{-2} and bare cathodes could be attributed to ORRs which are relatively incomplete and which proceed closer to the $2e^-$ transfer mechanism compared to the higher Pt loading cathodes. Overall; OCPs of the cathodes became farther from the potential proposed for $4e^-$ transfer ORR when the Pt loading was reduced, but loss in OCP was much more pronounced for the cathode having lowest Pt loading and cathode without catalyst.

As expected, maximum power densities obtained in MFCs were in the same order as the catalyst loading on cathodes. The addition of minimum amount of Pt only slightly improved the maximum power density of MFC with uncatalyzed cathode (59 ± 3 mW m^{-2} vs. 48 ± 1 mW m^{-2}) and voltage outputs in the entire current density range, indicating that 0.01 mg cm^{-2} was not very effective as a minimal Pt loading with the coating method described here. The decrease in maximum power density of MFC was 38% or higher when the use of Pt loading was reduced from 0.5 to 0.1 mg cm^{-2} or lower loadings, suggesting a considerable effect of catalyst loading on this performance indicator. On the other hand, CE range obtained throughout the polarization experiments was almost unaffected when the loading was reduced from 0.5 to 0.05 mg cm^{-2} (~15-33%), and lower (~9-20%) when the loadings were between 0 and 0.03 mg cm^{-2}. These low CEs usually result from decreased recovery of electrons from the substrate due to oxygen diffusion to the anode in MFC designs lacking a separator and the CE range obtained here with 0.5 mg cm^{-2} cathode was comparable to that obtained in a previous study which used the same cathode/reactor configuration and substrate, except lower current density range obtained here (Zhang et al., 2009). The durations of batch cycles in polarization experiments were unexpectedly longer with 0.1 and 0.05 mg Pt cm^{-2} cathodes than with 0.5 mg Pt cm^{-2} cathode, which resulted in higher CEs with these reduced loadings compared to 0.5 mg cm^{-2} at a given current density. In the work of Cheng et al., who showed CE data at 1 kΩ during an operational period of ~25 cycles, CEs obtained with 0.1 mg cm^{-2} cathode were half of those obtained with 0.5 mg cm^{-2} cathode. CEs further decreased by 10-20% compared to 0.1 mg cm^{-2} in the absence of Pt (Cheng et al., 2006). By comparison, individual CE values obtained here at 1 kΩ were consistent with their findings for zero and 0.5 mg Pt cm^{-2} loadings, but CE obtained with 0.1 mg cm^{-2} cathode at 1 kΩ (~17%) was higher than CE obtained with their cathode sample having the same loading. This difference is likely due to the trends observed in CEs with 0.05-0.5 mg Pt cm^{-2} loadings explained above.

For potentiostatic EIS experiments, a potential of -0.2 V vs. Ag/AgCl was chosen in order to observe diffusion resistances in cathodes along with resistances resulting from kinetic and ohmic limitations. Although impedance spectra of cathodes with 0.5, 0.1 and 0.05 mg Pt cm^{-2} at this selected cathode potential can be interpreted as the splitting of the main arcs into two, well-developed semi-circles corresponding to kinetic and diffusion processes were not clearly seen. In general, charge transfer resistance decreases with increasing overpotentials due to increasing kinetic rates, whereas resistance related to mass transfer effects is expected to appear below a certain potential and increase with further polarization for air-cathodes in PEM fuel cells (Yuan et al., 2007; Tang et al., 2006). Additional tests with these cathodes at higher potentials showed that there was not a diffusion-related characteristic at these potentials and single arcs present in spectra decreased in size with decreasing potential down to -0.2 V vs. Ag/AgCl, which means that apparent single loops observed at -0.2 V were either charge-transfer semi-circles that shrank with increasing overpotential, or a combination of a charge-transfer and a diffusion semi-circle which decreased and increased in size,

respectively, compared to a spectrum that would be obtained at an intermediate potential between 2 lowest potentials examined. Therefore, spectra at -0.2 V for these samples were fitted in two ways, by using two equivalent circuits. For consistency, resistive element in the circuit with a single time-constant was proposed as polarization resistance rather than charge-transfer resistance, and polarization resistance included unknown portions of charge-transfer and diffusion resistance. On the other hand, spectra of cathodes having 0-0.03 mg Pt cm^{-2} loadings at -0.2 V showed 2 semi-circles clearly and modelled by using only the equivalent circuit with 2 time-constants.

Internal resistance of the cathodes increased with reduced loadings, as expected. Internal resistance of 0.01 mg cm^{-2} cathode mainly differed from the cathode without catalyst in charge-transfer portion, as shown by a ~ 13 Ω decrease, indicating little kinetic improvement with this ultra low Pt loading. The dramatic decrease in charge-transfer resistance of 0.03 mg Pt cm^{-2} cathode with respect to 0.01 mg Pt cm^{-2} and relatively small decrease from this point on with higher loadings suggested that 0.03 mg cm^{-2} can be considered as the minimum Pt loading for which kinetic limitations are not of great concern and can be overcome to a large extent compared to lower loadings, although diffusion resistance of this cathode was still prominent. Like charge-transfer resistance, diffusion resistance was also found to decrease with increasing catalyst loadings. Diffusion layer structure, thickness of the catalyst layer and ionomer loading in cathodes are factors that possibly affect the transport of oxygen, protons or generated water at the cathode through the catalyst layer and therefore, diffusion resistance (Song et al., 2001; Lim et al., 2012). Considering the diffusion layers prepared in the same way for all cathodes in this study, differences in diffusion resistance can be attributed to catalyst layer thickness and Nafion content of cathodes which were varied with the application of different loadings by using the Pt/C catalyst with a constant weight percentage (20%) and constant weight ratio of ionomer to Pt/C (3:7). However, these effects can be better understood by using the same Pt loading but various thickness via altering Pt/C weight percentage, or by using the same Pt loading with various ionomer loadings in cathodes and their subsequent comparison in impedance spectra in terms of diffusion resistance.

An interesting finding throughout EIS experiments was the decrease of ohmic resistance to some extent with increasing catalyst loadings. In our setup, ohmic resistance includes contributions from resistance of the electrolyte solution, ionic and electronic resistances of the catalyst layer and contact resistances; while electronic and contact resistances are considered much smaller than ionic resistance [40] (Reimer et al., 2018). Therefore, the intercept values of the high frequency semicircles/arcs with the Z_{re} axis in Figure 5a and 5b were mainly a combination of resistance of the electrolyte solution and ionic resistance of the catalyst layer. Assuming the same resistance for solution, it is likely that differences in R_{Ω} were resulted from different ionic conductivities in the catalyst layers. Nafion ionomer, which was added to catalyst layers in proportion with Pt/C amounts in this study (constant weight ratio of ionomer to Pt/C = 3:7 in all samples), possibly enhanced proton transport there and decreased the R_{Ω} with increasing catalyst loadings.

Conclusions

The effect of Pt loadings of cathodes in the 0-0.5 mg cm^{-2} range on MFC performance and impedance behaviour was evaluated. Reducing benchmarking Pt loading of 0.5 mg cm^{-2} by a factor of 5 or more resulted in a 38% or higher decrease in maximum power density. The lowest loading of 0.01 mg Pt cm^{-2} used in the study only slightly improved OCV, voltage output throughout polarization, maximum power density in MFC tests and charge-transfer resistance in EIS compared to the cathode without catalyst. Charge-transfer resistance of 0.03 mg cm^{-2} cathode was increased to a smaller extent than lower loadings when Pt loading was reduced, whereas OCPs of cathodes were comparable in the 0.03-0.5 mg Pt cm^{-2} range in contrast with its significant decrease with 0.01 mg Pt cm^{-2} and bare cathodes. Along with charge-transfer resistance, diffusion resistance was also found to increase with decreasing catalyst loadings on cathodes due to structural differences affecting mass transfer in catalyst layers.

Conflict of interest

The authors declare no conflict of interest.

Data availability statement

Data can be obtained from the corresponding author upon a reasonable request.

Ethics committee approval

Ethics committee approval is not required for this study.

Authors' contribution statement

The authors acknowledge their contributions to this paper as follows: **Study conception and design**: E.S., H.B.; **Data collection**: E.S., B.A., N.M.; **Analysis and interpretation of results**: E.S., H.B.; **Manuscript draft preparation**: E.S., H.B. All authors reviewed the results and approved the final version of the manuscript.

References

Ayyaru, S., Mahalingam, S., & Ahn, Y.H. (2019). A non-noble V2O5 nanorods as an alternative cathode catalyst for microbial fuel cell applications. *International journal of hydrogen energy*, *44*, 4974. https://doi.org/10.1016/j.ijhydene.2019.01.021

Cheng, S., Liu, H., & Logan, B.E. (2006). Power densities using different cathode catalysts (Pt and CoTMPP) and polymer binders (nafion and PTFE) in single chamber microbial fuel cells. *Environmental science & technology*, *40*(1), 364-369. https://doi.org/10.1021/es0512071

Cheng, S., Liu, H., & Logan, B.E. (2006). Increased performance of single-chamber microbial fuel cells using an improved cathode structure. *Electrochemistry communications*, *8*, 489-494. https://doi.org/10.1016/j.elecom.2006.01.010

Dominguez-Benetton, X., Sevda, S., Vanbroekhoven, K., & Pant, D. (2012). The Accurate Use of Impedance Analysis for the Study of Microbial Electrochemical Systems. *Chemical Society reviews*, *41*(21), 7228-7246. https://doi.org/10.1039/c2cs35026b.

Feng, L., Chen, Y., & Chen, L. (2011). Easy-to-Operate and Low-Temperature Synthesis of Gram-Scale Nitrogen-Doped Graphene and Its Application as Cathode Catalyst in Microbial Fuel Cells. *ACS nano*, *5*(12), 9611-9618. https://doi.org/10.1021/nn202906f

HaoYu, E., Cheng, S., Scott, K., & Logan, B. (2007). Microbial fuel cell performance with non-Pt cathode catalysts. *Journal of power sources*, *171*, 275-281. https://doi.org/10.1016/j.jpowsour.2007.07.010

Harnisch, F., Wirth, S., & Schröder, U. (2009). Effects of substrate and metabolite crossover on the cathodic oxygen reduction reaction in microbial fuel cells: Platinum vs. iron(II) phthalocyanine based electrodes. *Electrochemistry communications*, *11*, 2253-2256. https://doi.org/10.1016/j.elecom.2009.10.002

He, Z., & Mansfeld, F. (2009). Exploring the use of electrochemical impedance spectroscopy (EIS) in microbial fuel cell studies. *Energy & environmental science*, *2*, 215-219. https://doi.org/10.1039/B814914C

Kumar, S., Malyan, S., & Bishnoi, N. (2017). Performance of buffered ferric chloride as terminal electron acceptor in dual chamber microbial fuel cell. *Journal of environmental chemical engineering*, *5*, 1238-1243. https://doi.org/10.1016/j.jece.2017.02.010

Lim, J.W., Cho, Y.H., Ahn, M., Chung, D.Y., Cho, Y.H., Jung, N., Kang, Y.S., Kim, O.H., Lee, M.J., Kim, M., & Sung, Y.E. (2012). Ionic resistance of a cathode catalyst layer with various thicknesses by electrochemical impedance spectroscopy for PEMFC. *Journal of the electrochemical society*, *159*, B378. https://doi.org/10.1149/2.030204jes

Lima, F.H.B., Zhang, J., Shao, M.H., Sasaki, K., Vukmirovic, M.B., Ticianelli, E.A., & Adzic, R.R. (2007). Catalytic Activity−d-Band Center Correlation for the O2 Reduction Reaction on Platinum in Alkaline Solutions. *The Journal of physical chemistry C*, *111*, 404-410. https://doi.org/10.1021/jp065181r

Liu, H., & Logan, B.E. (2004). Electricity Generation Using an Air-Cathode Single Chamber Microbial Fuel Cell in the Presence and Absence of a Proton Exchange Membrane. *Environmental science & technology*, *38*(14), 4040-4046. https://doi.org/10.1021/es0499344

Liu, H., Cheng, S., & Logan, B.E. (2005) Production of Electricity from Acetate or Butyrate Using a Single-Chamber Microbial Fuel Cell. *Environmental science & technology*, *39*(2), 658-662. https://doi.org/10.1021/es048927c

Liu, Q., Zhou, Y., Chen, S., Wang, Z., Hou, H., & Zhao, F. (2015). Cellulose-derived nitrogen and phosphorus dual-doped carbon as high performance oxygen reduction catalyst in microbial fuel cell. *Journal of power sources*, *273*, 1189-1193. https://doi.org/10.1016/j.jpowsour.2014.09.102

Logan, B.E., & Regan, J.M. (2006). Microbial Fuel Cells—Challenges and Applications. *Environmental science & technology*, *40*, 5172-5180. https://doi.org/10.1021/es0627592

Lovley, D.R., & Phillips, E.J. (1988). Novel Mode of Microbial Energy Metabolism: Organic Carbon Oxidation Coupled to Dissimilatory Reduction of Iron or Manganese. *Applied and environmental microbiology*, *54*(6), 1472-1480. https://doi.org/10.1128/aem.54.6.1472-1480.1988

Lu, G., Zhu, Y., Lu, L., Xu, K., Wang, H., Jin, Y., Jason-Ren, Z., Liu, Z., & Zhang, W. (2016). Iron-rich nanoparticle encapsulated, nitrogen doped porous carbon materials as efficient cathode electrocatalyst for microbial fuel cells. *Journal of power sources, 315*, 302. https://doi.org/10.1016/j.jpowsour.2016.03.028

Majidi, M.R., Shahbazi, F., Hosseini, M., & Ahadzadeh, I. (2019). Low-cost nanowired α-MnO2/C as an ORR catalyst in air-cathode microbial fuel cell. *Bioelectrochemistry (Amsterdam, Netherlands)*, *125*, 38-45. https://doi.org/10.1016/j.bioelechem.2018.09.004

Mateo, S., Fernandez-Morales, F.J., Cañizares, P., & Rodrigo, M.A. (2017). Influence of the cathode platinum loading and of the implementation of membranes on the performance of air-breathing microbial fuel cells. *Electrocatalysis*, *8*, 442-449. https://doi.org/10.1007/s12678-017-0393-7

Oh, S., Min, B., & Logan, B.E. (2004). Cathode Performance as a Factor in Electricity Generation in Microbial Fuel Cells. *Environmental science & technology*, *38*(18), 4900-4904. https://doi.org/10.1021/es049422p

Reimer, U., Lehnert, W., Holade, Y., & Kokoh, B. (2008). in Fuel Cells and Hydrogen- From Fundamentals to Applied Reserach (Eds. V. Hacker, S. Mitsushima), Elsevier, Amsterdam, Netherlands, pp. 15.

Rismani-Yazdi, H., Carver, S.M., Christy, A.D., & Tuovinen, O.H. (2008). Cathodic limitations in microbial fuel cells: An overview. *Journal of power sources*, *180*, 683-694. https://doi.org/10.1016/j.jpowsour.2008.02.074

Rittmann, B.E., Torres, C.I., & Marcus, A.K. (2008). Understanding the distinguishing features of a microbial fuel cell as a biomass-based renewable energy technology. *Emerging Environmental Technologies, ed. by V Shah*, Springer Netherlands, Dordrecht, pp. 1-28.

Rossi, R., Cario, B.P., Santoro, C., Yang, .W, Saikaly, P.E., & Logan, B.E. (2019). Evaluation of electrode and solution area-based resistances enables quantitative comparisons of factors impacting

microbial fuel cell performance. *Environmental science & technology*, *53*(7), 3977-3986. https://doi.org/10.1021/acs.est.8b06004

Rozendal, R.A., Hamelers, H.V., Rabaey, K., Keller, J., & Buisman, C.J. (2008). Towards practical implementation of bioelectrochemical wastewater treatment. *Trends in biotechnology*, *26*(8), 450-459. https://doi.org/10.1016/j.tibtech.2008.04.008

Santoro, C., Li, B., Cristiani, P., & Squadrito, G. (2013). Power generation of microbial fuel cells (MFCs) with low cathodic platinum loading. *International journal of hydrogen energy*, *38*, 692-700. https://doi.org/10.1016/j.ijhydene.2012.05.104

Song, J.M., Cha, S.Y., & Lee, W.M. (2001). Optimal composition of polymer electrolyte fuel cell electrodes determined by the AC impedance method. *Journal of power sources, 94*, 78-84. https://doi.org/10.1016/S0378-7753(00)00629-7

Springer, T., & Raistrick, I. (1989). Electrical Impedance of a Pore Wall for the Flooded-Agglomerate Model of Porous Gas-Diffusion Electrodes. *Journal of the electrochemical society*, *136*, 1594. https://doi.org/10.1149/1.2096975

Tang, Y., Zhang, J., Song, C., Liu, H., Zhang, J., Wang, H., Mackinnon, S., Peckham, T., Li, J., McDermid, S., & Kozak, P. (2006). Temperature Dependent Performance and In Situ AC Impedance of High-Temperature PEM Fuel Cells Using the Nafion-112 Membrane. *Journal of the electrochemical society, 153*, A2036. https://doi.org/10.1149/1.2337008

Tang, X., & Ng, H.Y. (2017). Cobalt and nitrogen-doped carbon catalysts for enhanced oxygen reduction and power production in microbial fuel cells. *Electrochimica acta*, *247*, 193-199. https://doi.org/10.1016/j.electacta.2017.06.120

Ucar, D., Zhang, Y., & Angelidaki, I. (2017). An Overview of Electron Acceptors in Microbial Fuel Cells. *Frontiers in microbiology*, *8*, 643. https://doi.org/10.3389/fmicb.2017.00643

Wang, Z., Cao, C., Zheng, Y., Chen, S., & Zhao, F. (2014). Abiotic Oxygen Reduction Reaction Catalysts Used in Microbial Fuel Cells. *ChemElectroChem*, *1*, 1813-1821. https://doi.org/10.1002/celc.201402093

Watson, V.J., & Logan, B.E. (2011). Analysis of polarization methods for elimination of power overshoot in microbial fuel cells. *Electrochemistry communications*, *13*, 54-56. https://doi.org/10.1016/j.elecom.2010.11.011

Wei, L., Han, H., & Shen, J. (2012). Effects of cathodic electron acceptors and potassium ferricyanide concentrations on the performance of microbial fuel cell. *International journal of hydrogen energy, 37*, 12980-12986. https://doi.org/10.1016/j.ijhydene.2012.05.068

Xia, X., Li, M., Liu, T., Liang, P., & Huang, X. (2018). Facile synthesis of cobalt oxide as electrocatalyst for the oxygen reduction reaction in microbial fuel cells. Chemical engineering journal, 342, 395-400. https://doi.org/10.1016/j.cej.2018.02.092

Yang, W., & Logan, B.E. (2016). Immobilization of a Metal–Nitrogen–Carbon Catalyst on Activated Carbon with Enhanced Cathode Performance in Microbial Fuel Cells. *ChemSusChem*, *9*(16), 2226-2232. https://doi.org/10.1002/cssc.201600573

You, S., Zhao, Q., Zhang, J., Jiang, J., & Zhao, S. (2006). A microbial fuel cell using permanganate as the cathodic electron acceptor. *Journal of power sources, 162*(2), 1409-1415. https://doi.org/10.1016/j.jpowsour.2006.07.063

Yuan, X., Wang, H., Colin-Sun, J., & Zhang, J. (2007). AC impedance technique in PEM fuel cell diagnosis—A review. *International journal of hydrogen energy, 32*, 4365-4380. https://doi.org/10.1016/j.ijhydene.2007.05.036

Zhang, X., Cheng, S., Wang, X., Huang, X., & Logan, B.E. (2009). Separator characteristics for increasing performance of microbial fuel cells. *Environmental science & technology*, *43*(21), 8456–8461. https://doi.org/10.1021/es901631p

Zhang, F., Pant, D., & Logan, B.E. (2011). Long-term performance of activated carbon air cathodes with different diffusion layer porosities in microbial fuel cells. *Biosensors & bioelectronics*, *30*(1), 49–55. https://doi.org/10.1016/j.bios.2011.08.025

EUCHEMBIOJ

THE EUROPEAN CHEMISTRY AND BIOTECHNOLOGY JOURNAL

Eur. Chem. Biotechnol. J. 1: 27-38 (2024) www.euchembioj.com

Research article

Determination of the inhibition effect of hesperetin and its derivatives on *Candida glabrata* by molecular docking method

Vildan Enisoglu Atalay[1*] | ORCID 0000-0002-9830-9158 | vildan.enisoglu@uskudar.edu.tr

Semse Asar[2] | ORCID 0009-0004-9172-3366 | semseamway@gmail.com

[1]**Uskudar University, Faculty of Engineering and Natural Sciences, Department of Molecular Biology and Genetics, 34662, Istanbul, Türkiye**

[2]**Uskudar University, Institute of Science and Technology, Department of Molecular Biology, 34662, Istanbul, Türkiye**

***Corresponding author**: vildan.enisoglu@uskudar.edu.tr; Pbx.: +90-216 400 2222 (ext.2411); Fax: +90-216 400 2222.

Received: 13.10.2023
Accepted: 02.12.2023
Published: 02.01.2024

Cite this article: Atalay, V., & Asar, S., 2024. Determination of the inhibition effect of hesperetin and its derivatives on *Candida glabrata* by molecular docking method. *The European chemistry and biotechnology journal*, *1*, 27-38. https://doi.org/10.62063/ecb-15

Abstract

In the study, it was aimed to develop new candidate inhibitor molecules by targeting the AWP1 protein structure of *Candida glabrata* organism. Hesperetin molecule was taken as a reference and different substituted groups were attached to the determined ends of the molecule to increase the inhibition potential on the protein structure. A total of 100 molecules were designed and after conformer distribution using the Molecular Mechanics/MMFF method for each designed molecule, the area, volume, weight, energy, E_{HOMO}, E_{LUMO}, polarizability, dipole moment, log P values of these molecules were calculated using the Semi Empirical/PM6 method. Molecular docking studies of the optimized molecules were carried out through the Autodock Vina program. After the docking studies, the interactions of the designed molecules with the active site amino acids of the protein structure were analyzed by BIOVIA Discovery Studio Client software in case of possible mutation. As a result of the analysis, five molecules with higher binding energies than other designed molecules and currently used antifungal drugs were recommended.

Keywords: Awp1, *Candida glabrata*, hesperetin, molecular docking

Introduction

Fungal infections affect more than one billion people worldwide each year, with more than 1.6 million infected cases resulting in death (Bongomin et al., 2017; Gupta et al., 2012). Among the microorganisms that cause disease in humans in the clinic, two important members of the yeast class can be ranked as *Candida albicans* and *Candida glabrata* according to their frequency of disease in humans (Calderone & Clancy, 2011). Invasive nosocomial infections are caused by *Candida* species, particularly in patients with impaired immune systems. Of these, *Candida albicans* is the most prevalent species that causes

non-invasive candidiasis of the skin and mucous membranes (Tamo, 2020). But non-albicans Candida species—like *C. glabrata, C. parapsilosis, C. tropicalis, C. krusei, C. lusitaniae, C. dubliniensis, and C. guilliermondii*—have shown a more than 50% increase in prevalence in recent years (Seyedmousavı et al., 2015; Tamo, 2020). According to recent research, *C. glabrata* is more frequently isolated in cases of invasive candidiasis and is linked to a higher patient death rate. Depending on the region under investigation, *C. glabrata* is either the second or third most commonly isolated species of *Candida* (Guinea & Infection, 2014). Additionally, *C. glabrata* is frequently encountered in the environment, particularly on surfaces, water, soil, flowers, and leaves. After *Candida albicans*, it is the second most common isolated cause of candidiasis. About 15–25% of invasive clinical cases are accounted for by it (McCarty & Pappas, 2016; Pfaller & Diekema, 2007). About 40–60% of cases of invasive candidiasis caused by *Candida glabrata* result in substantial morbidity and mortality, possibly as a result of the bacteria's intrinsic low sensitivity to the most widely used azoles (Timmermans et al., 2018). *C. glabrata* is basically a yeast, but what distinguishes it from non-pathogenic yeasts used as bread and brewer's yeast are differences in the structure of the cell wall. Studies using various biochemical tests have shown that adhesin-like glycophosphatidylinositol proteins are present in higher amounts in *C. glabrata* than in other yeasts (Weig et al., 2004). Mass-spectrometry was then used to identify the proteins more accurately, resulting in the identification of four new adhesin-like proteins. In addition to the results, these proteins were subsequently named Awp 1,2,3,4. In addition, Epa6 from the lectin-like EPA family, which clusters with these four new adhesin-like proteins, is responsible for the gel-like biofilm layer formed by *C. glabrata* to adhere to human epithelial cells. (de Groot et al., 2008) In conclusion, Awp2,3,4 and Epa6, which are novel adhesin-like proteins of *C. glabrata*, were found only in *C. glabrata* strains obtained in stool test results, while Awp1 was found in strains isolated from blood. Treatment of *C. glabrata* infections is complicated by their inherent resistance to antifungals, especially azoles. (Mota et al., 2015) Long-term exposure to antifungal drugs for treatment and prevention of infections may be the main reason for the development of newly drug-resistant strains, according to analytical studies (Jensen et al., 2016). The virulence of *C. glabrata* was investigated by combining biochemical tests and mycoscopy methods, and bioinformatics studies were utilized in further studies (Enkler et al., 2016).

In this study, the crystallographic structure of AWP1 which belongs to fungus *C. glabrata* organism was determined as a macromolecule and the designing of new ligands as candidate drug active molecules that can show antifungal effect was aimed. While designing new drug active molecules, the study was started using the hesperetin molecule. Afterwards, derivatization studies of the molecule were carried out with functional groups added to the hesperetin molecule.

The aglycone form of the hesperedin molecule, a flavanone glycoside abundant in citrus fruits, is called hesperetin. The scientific and common names of the plants containing the hesperetin molecule and the plant parts containing the molecule are given in Table 1.

Table 1. List of Plants Containing Hesperetin Molecule.

Plant	Common Name	Part
Artemisia dracunculus	Estragon	Shoot
Citrus paradisi	Grapefruit	Fruit
Citrus spp.	Citrus	Plant
Cynara cardunculus	Cardoon	Leaf
Eriodictyon californicum	Yerba santa	Resin, exudate, sap
Mentha aquatica	Water-mint	Plant
Mentha x piperita	Mentha spicata	Leaf

Resource: U.S. Department of Agriculture, Agricultural Research Service. (1992-2016). “Dr. Duke's Phytochemical and Ethnobotanical Databases. Home Page”. (Duke, 2020)

The two-dimensional structure of the hesperetin molecule and the positions on this structure where functional groups are planned to be attached are named as R_1, R_2, R_3, R_4, R_5, R_6, R_7, R_8.

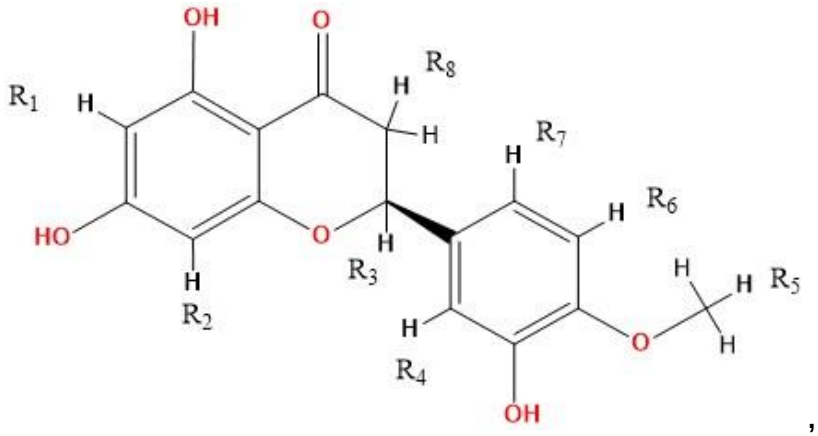

Figure 1. 2D structure and derivatization positions of the Hesperetin molecule.

In Table 2, functional groups and ligand numbers added to the binding positions described in Figure 1 are given. Based on the skeletal structure of the Hesperetin molecule, 100 molecular modifications were performed.

Table 2. Functional groups attached to the Hesperetin molecule and their positions.

Ligand	R_1	R_2	R_3	R_4	R_5	R_6	R_7	R_8
L-1						NH_2		
L-2	OH							
L-3		CH_3						
L-4								CH_2F
L-5					NO_2			
L-6				CH_2OH				
L-7							CH_3	
L-8					CH_2Cl			
L-9		CH_3CH_2						
L-10								COO
L-11							$C(CH_3)_3$	
L-12			OH					
L-13							OH	
L-14								OH
L-15		OH						
L-16				OH				
L-17					OH			
L-18						OH		
L-19	CH_3							
L-20						CCOH		
L-21			$CH_2CH_2CH_2$					
L-22					CH_2CH_3			
L-23				$CHOHCH_3$				
L-24							CH_2OCH_3	
L-25	$CH_2C(CH_3)_2OH$							
L-26				$CONH_2$				
L-27								CONH
L-28		$COCH_3$						
L-29			C_6H_{13}					
L-30	NO_2							
L-31	$C(CH_3)_3$							
L-32	C_6H_5							
L-33		C_6H_5O						
L-34					$C_6H_5O_2$			
L-35								O
L-36						CH_2CH_2		
L-37					$CH_2CH_2CH_2$			
L-38			$CH_2CH_2CH_2$					
L-39				$C(CH_3)_2O$				
L-40					C_6H_5			
L-41		C_6H_5						
L-42				C_6H_5				
L-43						C_6H_5		

L-44							C_6H_5	
L-45								C_6H_5
L-46								CH_3
L-47						CH_3		
L-48					CH_3			
L-49				CH_3				
L-50					NH_2			
L-51	NH_2							
L-52		NH_2						
L-53				NH_2				
L-54							NH_2	
L-55								NH_2
L-56								C_2H_3
L-57	OH	CH_3						
L-58			OH			OH		
L-59						OH		O
L-60	NH_2				NO_2			
L-61						C_6H_5		O
L-62	C_6H_5	CH_3						
L-63					C_6H_5			CONH
L-64				C_6H_5			$CONH_2$	
L-65	$CONH_2$			$C(CH_3)_2O$				
L-66	$CONH_2$				C_6H_5O			
L-67				NH_2				C_7H_7
L-68				CH_2CH_3	C_6H_5OS			
L-69						OH		O
L-70		NH_2			$C_6H_3F_2$			
L-71		$C_6H_3Cl_2$			$C_3H_3N_2$			
L-72				$C_3H_3N_3$				O
L-73	NH_2						$C_6H_3Cl_2$	
L-74				NH_2		$C_6H_3F_2$		
L-75		C_2H_3FN						O
L-76	CH_3			$C_4H_3O_2S$				O
L-77	NH_2			$C(CH_3)_3$				O
L-78		C_6H_5			OH			S
L-79					OH		$C_6H_3F_2$	
L-80	NH_2		$C(CH_3)_3$		OH			
L-81			OH		$C_3H_5O_2$			
L-82	NH_2		OH	$C_3H_5O_3$				
L-83	$CONH_2$			$C_3H_5O_2$				
L-84		CH_3			C_6H_5O			O
L-85	CH_3		OH		CH_2Cl			
L-86			OH	CH_2Cl	NH_2			
L-87		CH_3	OH					CONH
L-88		$C_6H_3Cl_2$	OH					CONH
L-89					$C_4H_7O_2$			CONH
L-90	$CONH_2$		OH		CF_3			
L-91	$CONH_2$	OH						CF_3
L-92	$CONH_2$		OH					CCl_3
L-93	NH_2	$CONH_2$			OH			CONH
L-94	CH_2OH		OH		CH_3			
L-95					Cl	$CONH_2$		OH
L-96	CH_2OH		OH		Cl			
L-97	$CONH_2$	C_6H_5O			CCl_3			
L-98	$CONH_2$	SH	OH					
L-99	$CONH_2$	OH			CH_2CH_2OH			
L-100	$CONH_2$			C_6H_5O		CH_2CH_3		

Materials and methods

In the study, conformer distribution analysis with molecular mechanics/MMFF method and geometry optimization of the designed molecules were performed using Semi Empirical/PM6 method in Spartan'14 (Spartan '14 V1.1.4) software. Visualization of the selected protein structure before docking studies was performed using the BIOVIA Discovery Studio software (Biovia, 2021). During these imaging processes, the water molecules in the crystal structure of the protein were deleted and the active site coordinates were selected as given in Table 3. The determined active site coordinates were also selected as the gridbox center coordinates in the Autodock Tools software (Morris et al., 2009)

used in the preparation of the docking files of proteins and ligands in the continuation of the studies, and other data used for the gridbox are given in Table 3.

Table 3. Grid Box Coordinates, Size and Spacing of the protein.

Coordinates	Grid box size	Grid space
x = 8.968	x=40	
y = 28.866	y=40	0.374 Å
z = 41.670	z=40	

Docking studies of protein and derivatized ligand molecules were performed by running the Autodock Vina software on the command prompt (Eberhardt et al., 2021). After the docking scores were calculated, the results obtained were analyzed using the BIOVIA Discovery Studio software. In the analyses, protein-ligand interaction maps were generated and the interaction types and distances of the ligand molecule with the amino acids around the active site in the target protein structure were noted in these maps.

Results and discussion

For each modification, area, volume, molecular weight(MW), energy, E_{HOMO}, E_{LUMO}, polarizability (α), dipole moment(μ), logP values of these molecules were calculated using Spartan'14 software and applying the Semi-Empirical/PM6 method. The results obtained are given in Table 4. In addition to the physicochemical parameters, the Binding Energies (BE) of the molecules with the protein structure and the inhibition constants (K_i) of these molecules also calculated.

Table 4. Physicochemical parameters of hesperetin and its derivatives.

Ligands	Area (Å^2)	Volume (Å^3)	MW (amu)	Energy (kcal.mol^{-1})	E_{HOMO} (eV)	E_{LUMO} (eV)	α	μ (debye)	logP	BE (kcal.mol^{-1})	K_i
Fluconazole	302.51	281.30	306.27	-41.76	-10.35	-0.97	61.98	2.97	-1.04	-8.6	4.96 x 10^{-7}
Hesperetin	301.62	285.56	302.28	-853.19	-8.94	-0.62	62.57	4.70	-3.12	-8.7	4.19 x 10^{-7}
L-1	315.11	296.34	317.29	-907.05	-8.97	-0.65	63.45	4.11	-4.84	-8.9	2.99 x 10^{-7}
L-2	309.3	292.86	318.28	-1038.63	-8.84	-0.86	63.25	4.72	-4.21	-9.4	1.29 x710^{-7}
L-3	319.76	303.53	316.30	-991.75	-8.93	-0.62	64.04	5.13	-2.95	-9.2	1.8 x 10^{-7}
L-4	324.02	308.54	334.29	-1091.90	-8.98	-0.67	64.44	4.69	-2.91	-8.7	4.19 x 10^{-7}
L-5	327.78	307.07	347.27	-828.18	-9.36	-0.74	64.25	3.10	-4.46	-9.3	1.52 x 10^{-7}
L-6	322.99	310.15	332.30	-1097.20	-9.09	-0.57	64.52	6.35	-4.01	-8.7	4.19 x 10^{-7}
L-7	319.10	303.24	316.30	-930.19	-8.76	-0.56	64.04	5.39	-2.95	-9.3	1.52 x 10^{-7}
L-8	336.28	318.10	350.75	-944.40	-9.16	-0.67	65.18	4.85	-2.41	-9.0	2.53 x 10^{-7}
L-9	339.86	321.99	330.33	-934.96	-8.93	-0.60	65.53	5.06	-2.53	-9.2	1.8 x 10^{-7}
L-10	324.11	312.15	346.29	-1230.78	-8.92	-1.20	64.87	2.73	-3.49	-8.9	2.99 x 10^{-7}
L-11	362.95	355.03	358.39	-978.70	-8.75	-0.54	68.24	5.78	-1.73	-9.3	1.52 x 10^{-7}
L-12	310.62	293.05	318.28	-1097.51	-9.10	-0.63	63.15	6.08	-2.90	-9.7	7.75 x 10^{-8}
L-13	307.43	292.12	318.28	-1085.40	-8.70	-0.81	63.21	3.28	-4.21	-9.7	7.75 x 10^{-8}
L-14	306.81	292.73	318.28	-1039.91	-8.76	-0.95	63.28	2.26	-3.78	-9.0	2.53 x 10^{-7}
L-15	309.57	292.92	318.28	-1037.21	-8.92	-0.85	63.23	6.99	-4.21	-9.4	1.29 x 10^{-7}
L-16	309.37	292.75	318.28	-1074.80	-9.11	-0.53	63.10	5.77	-4.21	-9.2	1.8 x 10^{-7}
L-17	307.99	292.25	318.28	-1096.81	-9.27	-0.68	63.05	6.35	-3.36	-9.4	1.29 x 10^{-7}
L-18	310.68	293.13	318.28	-1075.81	-9.46	-0.70	63.09	4.36	-4.21	-9.8	6.54 x 10^{-8}
L-19	318.52	303.24	316.30	-916.86	-8.91	-0.60	64.01	4.24	-2.95	-9.1	2.13 x 10^{-7}
L-20	339.22	321.24	342.30	-797.93	-9.28	-0.78	65.43	5.07	-3.78	-9.2	1.8 x 10^{-7}
L-21	354.17	339.52	344.36	-967.14	-8.89	-0.56	66.95	4.69	-2.00	-8.8	3.54 x 10^{-7}
L-22	342.47	322.54	330.33	-945.44	-8.88	-0.60	65.58	5.27	-2.30	-9.3	1.52 x 10^{-7}
L-23	342.40	328.44	346.33	-1126.65	-9.10	-0.63	66.02	6.00	-3.69	-8.8	3.54 x 10^{-7}
L-24	346.74	330.62	346.33	-1074.31	-8.86	-0.42	66.20	6.87	-3.65	-8.6	4.96 x 10^{-7}
L-25	378.75	363.81	374.38	-1205.32	-8.87	-0.45	68.90	4.70	-3.19	-9.5	1.09 x 10^{-7}
L-26	327.90	315.06	345.30	-1075.35	-9.30	-0.98	64.97	8.29	-4.53	-9.2	1.8 x 10^{-7}
L-27	329.52	315.80	345.30	-1063.75	-8.79	-0.93	65.14	2.03	-4.14	-9.1	2.13 x 10^{-7}
L-28	334.37	322.21	344.31	-1105.44	-9.23	-0.78	65.52	8.44	-3.37	-9.1	2.13 x 10^{-7}
L-29	422.18	408.02	398.45	-947.47	-8.86	-0.53	72.51	3.80	-0.51	-9.0	2.53 x 10^{-7}
L-30	321.70	305.60	347.27	-926.60	-9.24	-1.23	64.29	9.24	-5.56	-9.3	1.52 x 10^{-7}

L-31	366.67	355.62	358.39	-975.18	-8.95	-0.55	63.24	6.42	-1.23	-9.4	1.29×10^{-7}
L-32	379.22	368.78	378.38	-786.89	-8.95	-0.65	69.33	4.70	-2.56	-10.3	2.81×10^{-8}
L-33	389.72	376.32	394.37	-974.62	-8.95	-0.64	69.94	6.33	-3.64	-9.9	5.53×10^{-8}
L-34	401.87	384.52	410.37	-1146.95	-8.97	-0.63	70.60	4.64	-4.35	-9.7	7.75×10^{-8}
L-35	305.22	288.71	316.26	-922.52	-8.92	-1.35	63.01	4.40	-2.95	-9.1	2.13×10^{-7}
L-36	341.92	328.44	346.33	-1125.55	-9.46	-0.75	65.97	3.16	-3.73	-9.2	1.8×10^{-7}
L-37	351.81	330.21	346.33	-1104.84	-8.85	-0.57	66.21	6.61	-3.36	-9.6	9.17×10^{-8}
L-38	336.55	343.60	360.36	-772.15	-8.4	-1.35	67.58	4.24	-3.32	-8.7	4.19×10^{-7}
L-39	355.00	344.88	360.36	-1158.51	-8.92	-0.39	67.34	5.60	-3.47	-9.4	1.29×10^{-7}
L-40	384.66	370.00	378.38	-781.27	-8.96	-0.63	69.42	4.90	-2.19	-9.4	1.29×10^{-7}
L-41	379.14	368.78	378.38	-786.74	-8.95	-0.64	69.33	7.16	-2.56	-9.5	1.09×10^{-7}
L-42	376.42	368.490	378.38	-788.10	-8.92	-0.56	69.29	4.42	-2.56	-10.1	3.94×10^{-8}
L-43	378.23	368.76	378.38	-792.57	-9.26	-0.73	69.28	4.32	-2.56	-10.3	2.81×10^{-8}
L-44	378.02	368.77	378.38	-795.72	-8.88	-0.53	69.32	5.27	-2.56	-10.0	4.67×10^{-8}
L-45	376.69	368.68	378.38	-766.29	-8.87	-0.61	69.33	5.08	-1.37	-9.1	2.13×10^{-7}
L-46	317.80	303.40	316.30	-910.75	-8.91	-0.60	64.03	4.44	-2.56	-8.7	4.19×10^{-7}
L-47	321.47	304.01	316.30	-884.14	-8.61	-0.43	64.10	2.90	-2.95	-9.0	2.53×10^{-7}
L-48	322.50	304.19	316.30	-924.29	-8.88	-0.60	64.10	5.14	-2.78	-9.4	1.29×10^{-7}
L-49	317.83	303.07	316.30	-928.79	-8.86	-0.60	64.01	4.15	-2.95	-9.1	2.13×10^{-7}
L-50	314.49	296.42	317.29	-886.04	-9.02	-0.60	63.43	6.15	-3.74	-9.3	1.52×10^{-7}
L-51	314.68	296.22	317.29	-886.91	-8.95	-0.66	63.45	4.18	-4.84	-9.4	1.29×10^{-7}
L-52	314.94	296.33	317.29	-886.91	-9.07	-0.66	63.43	7.70	-4.84	-9.6	9.17×10^{-8}
L-53	312.51	295.83	317.29	-886.25	-8.73	-0.56	63.44	4.53	-4.84	-9.0	2.53×10^{-7}
L-54	310.73	295.35	317.29	-901.51	-8.37	-0.61	63.50	5.91	-4.84	-9.3	1.52×10^{-7}
L-55	314.22	296.60	317.29	-857.94	-8.71	-0.79	63.56	3.14	-4.16	-9.2	1.8×10^{-7}
L-56	334.65	323.91	344.31	-1016.87	-8.86	-0.67	65.72	4.48	-3.81	-8.9	2.99×10^{-7}
L-57	327.44	310.83	332.30	-1061.47	-8.70	-0.85	64.73	5.08	-4.03	-8.9	2.99×10^{-7}
L-58	319.90	300.69	334.28	-1274.99	-9.53	-0.87	63.72	5.50	-3.98	-9.6	9.17×10^{-8}
L-59	314.13	262.22	332.26	-1103.87	-9.42	-1.43	63.52	2.42	-4.04	-9.3	1.52×10^{-7}
L-60	328.59	312.74	362.29	-1314.32	-7.26	1.70	64.63	2.91	-4.60	-9.7	7.75×10^{-8}
L-61	382.20	371.96	392.36	-820.40	-9.21	-1.40	69.70	3.03	-2.39	-9.9	5.53×10^{-8}
L-62	397.56	386.77	392.40	-807.24	-8.93	-0.64	70.79	4.96	-2.38	-9.4	1.29×10^{-7}
L-63	412.39	400.20	421.40	-950.65	-8.78	-0.92	71.99	2.43	-3.20	-9.9	5.53×10^{-8}
L-64	409.23	398.84	421.40	-965.63	-9.22	-0.72	71.72	5.75	-3.96	-9.0	2.53×10^{-7}
L-65	382.23	373.66	403.38	-1381.02	-9.02	-0.54	69.69	7.88	-4.88	-10.0	4.67×10^{-8}
L-66	419.99	405.97	437.40	-1190.20	-8.93	-0.73	72.37	7.57	-4.68	-11.2	6.16×10^{-9}
L-67	429.09	420.51	455.48	-1080.32	-8.60	-0.81	73.65	3.20	-5.30	-9.8	6.54×10^{-8}
L-68	445.01	429.70	454.49	-1017.46	-8.84	-0.61	74.29	4.70	-3.19	-10.0	4.67×10^{-8}
L-69	314.13	296.22	332.26	-1103.87	-9.42	-1.43	63.52	2.42	-4.04	-9.2	1.8×10^{-7}
L-70	408.37	389.88	429.37	-1161.50	-9.24	-0.91	71.04	7.34	-2.79	-10.1	3.94×10^{-8}
L-71	467.25	457.54	513.33	-692.48	-9.26	-0.92	76.52	4.06	-0.41	-9.9	5.53×10^{-8}
L-72	359.61	349.35	382.32	-739.91	-9.28	-1.53	67.88	8.13	-3.81	-9.6	9.17×10^{-8}
L-73	420.87	406.27	462.28	-865.88	-9.03	-0.82	72.40	5.41	-2.36	-10.4	2.38×10^{-8}
L-74	401.00	388.51	429.37	-1181.82	-8.85	-0.86	71.00	2.95	-3.16	-10.4	2.38×10^{-8}
L-75	359.65	343.68	391.30	-1248.52	-9.15	-1.42	67.43	7.18	-3.27	-9.8	6.54×10^{-8}
L-76	400.15	391.35	444.41	-1196.64	-9.08	-1.50	71.33	8.89	-3.87	-8.4	6.95×10^{-7}
L-77	374.41	367.41	387.38	-994.18	-8.78	-1.34	69.42	2.69	-3.28	-9.5	1.09×10^{-7}
L-78	393.53	386.81	424.42	-811.23	-9.26	-2.16	71.08	4.28	-1.28	-8.3	8.23×10^{-7}
L-79	397.02	384.84	430.35	-1390.07	-9.27	-0.80	70.59	4.24	-1.68	-9.3	1.52×10^{-7}
L-80	384.17	373.79	389.40	-1178.49	-9.46	-0.61	69.68	3.45	-3.56	-8.1	1.15×10^{-6}
L-81	377.49	356.44	390.34	-1433.12	-9.12	-0.63	68.29	7.53	-3.01	-9.9	5.53×10^{-8}
L-82	371.36	362.32	405.35	-1405.69	-9.23	-0.77	68.77	7.35	-5.08	-9.9	5.53×10^{-8}
L-83	365.25	377.58	417.37	-1446.00	-9.22	-0.83	70.02	4.08	-4.83	-10.3	2.81×10^{-8}
L-84	416.05	398.50	422.38	-1020.86	-8.84	-1.29	71.92	4.15	-1.43	-10.2	3.33×10^{-8}
L-85	362.57	343.35	380.78	-1169.65	-9.22	-0.71	67.22	6.09	-2.01	-10.0	4.67×10^{-8}
L-86	351.05	334.85	381.76	-1143.72	-9.24	-0.86	66.56	7.06	-3.18	-9.0	2.53×10^{-7}
L-87	356.75	341.14	375.33	-1273.51	-8.86	-0.87	67.16	3.20	-3.73	-10.1	3.94×10^{-8}
L-88	441.77	432.80	506.29	-1222.23	-8.89	-0.98	74.62	2.60	-1.43	-9.1	2.13×10^{-7}
L-89	414.10	395.43	431.39	-1480.28	-8.91	-0.97	71.58	1.71	-4.24	-9.9	5.53×10^{-8}
L-90	374.56	354.44	429.30	-1980.61	-9.61	-1.07	68.11	5.16	-3.32	-11.0	8.63×10^{-9}
L-91	366.82	353.18	429.30	-1883.43	-8.97	-1.34	68.22	2.20	-4.61	-10.6	1.7×10^{-8}

L-92	383.87	377.83	478.66	-1304.22	-8.93	-1.29	70.22	2.39	-3.86	-10.6	1.7×10^{-8}
L-93	346.88	331.86	376.32	-1278.09	-8.27	-0.95	66.56	9.80	-6.46	-9.8	6.54×10^{-8}
L-94	355.27	336.19	362.33	-1345.06	-9.05	-0.62	66.66	5.98	-3.44	-9.6	9.17×10^{-8}
L-95	348.99	336.74	395.75	-1257.37	-9.55	-1.10	66.70	3.19	-4.66	-10.8	1.21×10^{-8}
L-96	348.97	331.79	382.75	-1347.49	-9.61	-0.99	66.26	3.61	-3.26	-10.2	3.33×10^{-8}
L-97	463.02	462.15	554.76	-1285.57	-8.97	-1.01	76.98	2.34	-3.32	-9.5	1.09×10^{-7}
L-98	354.89	338.44	393.37	-1316.26	-8.41	-0.90	67.05	5.09	-4.81	-10.1	3.94×10^{-8}
L-99	367.46	348.00	391.33	-1431.91	-8.83	-1.08	67.77	2.56	-6.13	-10.5	2.01×10^{-8}
L-100	448.28	440.64	465.45	-1246.87	-9.16	-0.74	75.13	5.57	-4.45	-9.7	7.75×10^{-8}

In the study, the docking results of Hesperetin and its derivatives were found in the range of -8.7 to -11.0 kcal.mol^{-1}, while the binding affinity of the drug Fluconazole was found to be -8.6 kcal.mol^{-1}. This change in binding energy means that the affinity of the molecule under study is increased approximately 100 times. In particular, it was observed that the -$CONH_2$ substituent attached to the R_1 and R_2 positions of the substituted groups contributed positively to the affinity. It was also observed that the increase in the area and volume values of the molecules was in parallel with the increase in the binding energies of the molecules. In order to make more detailed analysis with the obtained interaction map, the active site amino acids interacting with the ligands are organized in Table 5 by indicating the distances of the interaction types.

Table 5. Ligand-amino acid interactions.

	L-0	L-1	L-2	L-3	L-4	L-5	L-6	L-7	L-8	L-9	L-10	L-11	L-12	L-13	L-14	L-15	L-16	L-17	L-18	L-19	L-20
A B:72																					
A B:73	5.23	5.27		2.81	5.32			2.42	5.23							5.08					
V B:74	2.63	5.0							2.62	3.78						2.74					
S B:75				2.59	3.09																
S B:98																					
N B:99																	3.20				
T B:100				3.17	2.5			3.28					3.03	3.03			2.37		2.98		
G B:101	2.70	3.27							2.70							2.73					
P B:102												4.06									
S B:103	2.46	3.44			3.01				2.46	2.72						2.48	2.89				
T B:104	2.66	3.79		2.42				2.96	2.66				2.59	2.40		2.59			2.35		
T A: 128							2.39														
T B:128																					2.79
N B:129																				2.39	2.37
E A:152						2.49															
S B:153			2.32			3.41					2.1										
G A:155																		2.12			
G B:155											2.47										
S A:156																					2.61
S B:156						2.94									2.86			2.51			
E B:157						2.51	2.85														
T B:158																					2.81
N A:159																		2.53			
D A:160																		1.44			
N A:186			2.45			2.7					2.2							2.40			
A B:188																					2.82
A A:189																					2.37
A B:189						2.6	2.72								2.49			2.32			2.93
K A:208			5.25			2.4	2.28				4.88				2.54			2.36			
K B:208			2.82			3.1	3.06								3.05					2.60	2.98
F A:210												5.27									
T A:227																			2.95		
A A:230												5.39									
F A:247				5.36															4.99		
F A:248				4.63	3.58			4.94		2.83		6.96	4.95	4.93		5.75	5.16		4.76		
G A:249																			3.58		
I A:251												4.10									
A A:253												4.92									
T A:297												2.93									
L A:298												5.40									
L A:309												5.03									

Table 5. Ligand-amino acid interactions (cont.)

	L-21	L-22	L-23	L-24	L-25	L-26	L-27	L-28	L-29	L-30	L-31	L-32	L-33	L-34	L-35	L-36	L-37	L-38	L-39	L-40
A B:72		4.45																		
A B:73									5.29	2.32		2.23	5.40	2.10	2.39	5.23	2.47			2.33
V B:74	2.89															2.61		2.74	2.31	
S B:75									2.89											
N B:99		3.43				3.49						2.18		3.73						
T B:100	2.57	2.43		2.60		2.43			2.23	3.44	3.02	3.19	2.60	2.33	2.68		3.17			2.80
G B:101	2.49															2.72				
P B:102																			4.09	
S B:103						2.86		2.22						2.75	2.57	2.47				
T B:104								2.74		2.68	2.40		3.02		2.30	2.66	2.56	3.40		2.80
E B:105				2.90																
T B:128			2.16																	
S A:153					2.72															
S B:153			3.04																	
S B:156							2.88													
E A:157			2.89																	
E B:157							2.52													
N A:186			3.62																	
A B:187							2.48													
A B:189			2.70		2.31															
K A:208			3.00		2.29		3.01													
T A:227										2.25		2.55								2.13
F A:248						5.36		4.89	5.31	4.91	4.87	4.43	5.18		4.65		4.87	4.32		4.87
L A:311				5.24															5.08	
N A:313													2.95							

Table 5. Ligand-amino acid interactions (cont.).

	L-41	L-42	L-43	L-44	L-45	L-46	L-47	L-48	L-49	L-50	L-51	L-52	L-53	L-54	L-55	L-56	L-57	L-58	L-59	L-60
A B:72						5.48									5.43				5.44	
A B:73						2.74	3.77		2.29	2.88		5.17							2.83	
V B:74												2.72								3.74
S B:75		2.80		2.88											2.76					
N B:99													3.26							
T B:100				2.36				3.14	3.43	3.19			2.36	3.07	2.86			2.94		3.16
G B:101												2.73								3.05
P B:102		2.41														2.78				
S B:103				2.84			2.79					2.43			2.98			2.84		2.63
T B:104				2.57		2.84	2.79	2.44	2.97	2.46		2.59		2.79				2.53	2.77	2.60
H B:127																4.71				
T B:128	1.50		1.22																	
N B:129											2.02					2.23				
T B:130																3.47				
S A:153			2.30																	
S B:153	2.46		2.22																	
P B:161																4.46				
N A:186	3.47																			
A B:187	2.77		3.36																	
A B:188																				
A A:189																	2.12			
A B:189																	2.00			
K A:208	2.64		2.95																	
K B:208	3.13		2.48								2.46						2.84			
F A:210																5.17				
T A:227						1.55			2.25						1.73			1.62	1.57	
F A:247																		5.35		
F A:248					4.92			4.81	4.90	4.81		3.70	4.43	4.99				4.65		
G A:249						3.73									3.71			3.71	2.76	
I A:251		5.06																		
L A:298																2.93				
S A:299																2.65				
L A:311		4.89																		
N A:313																				3.08

Table 5. Ligand-amino acid interactions (cont.).

	L-61	L-62	L-63	L-64	L-65	L-66	L-67	L-68	L-69	L-70	L-71	L-72	L-73	L-74	L-75	L-76	L-77	L-78	L-79	L-80
A B:72																				
A B:73		2.34			2.69						4.93			2.31	2.67			2.39		
V B:74							2.41								2.17			1.88		
S B:75				3.39									3.78				3.57			
S B:98			2.89		2.65															
N B:99			3.10		2.10									2.14	3.29					
T B:100		3.42	2.56		3.25		2.30						2.49	3.20	2.65		2.38	2.64		
G B:101												5.03								
P B:102				2.43								4.20				3.82				
S B:103		3.08		2.68			2.84										2.33	2.00		
T B:104		2.66															2.67	3.01		
T B:128								2.29		2.72									2.54	
N B:129	1.91																			
E A:152										3.98										2.29
S A:153						2.71			2.88	3.17										3.75
S B:153										2.71									2.00	2.98
G A:155	3.77																		2.60	
S A:156	2.89																		3.59	
S B:156						2.51														
E A:157								2.97		2.50									2.91	2.15
E B:157																			2.35	2.89
N A:159						2.80														
D B:160						4.96														
P B:161												2.62								
N A:186								2.70		2.64										2.89
A A:189						3.28			2.39											
A B:189						1.54		2.70	2.37										2.81	
K A:208	1.81					2.30		2.97	2.42	1.83									2.45	5.39
K B:208	2.31									3.06									2.56	3.59
F A:210												5.31								
T A:227		2.21			2.17									2.49						
F A:247														4.47						
F A:248		3.98	4.88		4.55		2.85				2.96			4.45				5.84		
G A:249			2.61		2.49									2.62		2.18				
I A:251				5.17																
T A:297												2.61								
L A:311				4.98							5.47		4.48			4.25				
N A:313				1.91			2.48													

Table 5. Ligand-amino acid interactions (cont.).

	L-81	L-82	L-83	L-84	L-85	L-86	L-87	L-88	L-89	L-90	L-91	L-92	L-93	L-94	L-95	L-96	L-97	L-98	L-99	L-100
A B:73		5.42					5.50	5.20						5.36	2.64					
V B:74							2.61													
S B:75							3.01													
S B:98	2.65				2.53															
N B:99	2.09				2.05									2.78	2.50					
T B:100	2.46				2.48									2.68		3.04				
G B:101							2.51													
P B:102															2.97					
S B:103							2.39	2.54						3.00	1.68					
T B:104							2.79								3.80	2.62				
T B:128				1.99					2.98				2.81							
N A:129																				2.40
N B:129			2.63						2.43											
S A:153																	2.58			
S B:153				2.57							2.45	2.48					3.07			
G B:155											3.57						2.32			
S B:156						3.83			2.54										3.79	
E A:157											2.93	2.92								
E B:157									2.65								2.27			2.50
D A:160						1.67				2.54									2.53	
D B:160			1.85			2.49												2.48		
N A:186																	2.36			
A B:187									2.70											
A A:189			2.25			2.35			1.99	2.42	2.50	2.57	2.23					2.04	2.39	2.08
A B:189			2.30	2.66					1.90	2.53	2.67	2.64	2.16					2.51	2.52	
K A:208				3.66		2.91			3.92	2.47	2.13	2.15	3.51				6.27		2.22	2.42

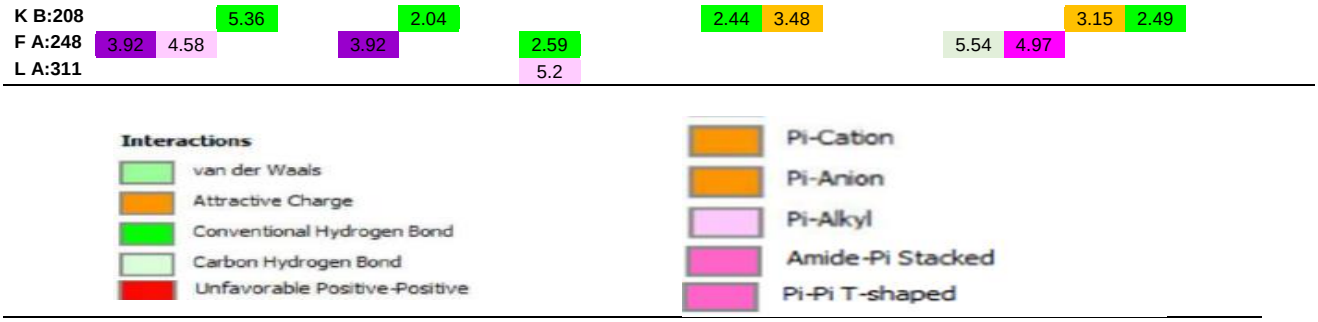

In addition to the results, it can be said that the derivatizations made at the R_4, R_7 and R8 positions contribute less to the affinity than those made at the R_1 and R_5 ends, even if there is an increase in the binding energy, they support unfavorable donor-donor interactions. The R_6 position had no positive or negative effect on affinity. Especially -NH_2, -OH and -CH_3 groups can be said to increase protein-ligand interactions by increasing the number of conventional hydrogen bonds which are very important in intermolecular interactions. When the interactions of Hesperetin molecule with the target macromolecule structure are considered, it is seen that it interacts with Ser103 and Val74 amino acids with conventional hydrogen bonds of 2.46 and 2.63 Å, respectively, and with Gly101 and Thr104 amino acids with carbon-hydrogen bonds of 2.70 and 2.66 Å, respectively also. A remarkable point in the interaction map is that the interacting amino acids belong to the B lobe. As a result of the substituted groups attached to the molecule in the derivatization study, interactions with amino acids in the A lobe could also be observed. Therefore, this allows us to interpretation of both the effector molecules designed and the active site characterization of the protein structure. The critical amino acids in the active site of the protein were determined by analyzing the data in Table 5. As a result of these examinations, the amino acids that interacted with the closest conventional hydrogen bond were determined as Ala B: 73, Thr B: 100, Ser B: 103, Thr B: 128, Asn B: 129, Ser B: 150, Ala A: 189, Ala B: 189, Lys A: 208. Therefore, it can be said that a possible mutation in these amino acids is critical in protein structure and function. In the analyzed results, the proposed molecules are ligands L-66, L-92, L-95, L-90 and L-99.

Conclusions

The aim of this study was to design new drug molecules that can show antifungal effect against *C. glabrata.* Out of 100 designed molecules, 5 candidate active molecules were selected. This is because there is more than one eliminating factor. While candidate molecules are expected to have high binding energies, they are also expected to interact in close proximity with the critical active site amino acids in the targeted protein structure. Another criterion evaluated is the type and characteristics of the observed interactions. At the same time, in the results obtained, the amino acids in the active site of the protein and determining the interactions with the molecules were generally polar and uncharged amino acids. Exceptionally, the apolar and aliphatic amino acid alanine and the positively charged amino acid lysine were also significant. Considering that *C. glabrata* develops a mechanism of resistance to drugs by mutating in a rapid period of time, it is necessary to design new candidate molecules that are antifungal effective, resistant to mutations and highly selective. It is recommended to further improve the information obtained on the inhibition potential of candidate molecules by targeting different protein structures of the organism in future studies.

Conflict of interest

The authors declare no conflict of interest.

Data availability statement

Data can be obtained from the corresponding author upon a reasonable request.

Ethics committee approval

Ethics committee approval is not required for this study.

Authors' contribution statement

The authors acknowledge their contributions to this paper as follows: Study conception and design: V.E.A., S.A.; Data collection: V.E.A., S.A.; Analysis and interpretation of results: V.E.A., S.A.; Manuscript draft preparation: V.E.A., S.A.. All authors reviewed the results and approved the final version of the manuscript.

References

Biovia, D.S.J.S.D.D.S. 2021. Discovery Studio Visualizer v21. 1.0. 20298.

Bongomin, F., Gago, S., Oladele, R.O., & Denning, D.W. (2017). Global and Multi-National Prevalence of Fungal Diseases-Estimate Precision. *Journal of fungi (Basel, Switzerland)*, *3*(4), 57. https://doi.org/10.3390/jof3040057

Calderone, R.A., & Clancy, C.J. (2012). Candida and candidiasis. American Society for Microbiology Press, 2nd Edition. ASM Press, Washington, DC.

De Groot, P.W., Kraneveld, E.A., Yin, Q.Y., Dekker, H.L., Groß, U., Crielaard, W., de Koster, C.G., Bader, O., Klis, F.M., & Weig, M. (2008). The cell wall of the human pathogen Candida glabrata: differential incorporation of novel adhesin-like wall proteins. *Eukaryotic cell*, *7*(11), 1951–1964. https://doi.org/10.1128/EC.00284-08

Duke, J.A. (1992). Database of biologically active phytochemicals & their activity. CRC Press, pp 1-30. ISBN 9780849336713

Eberhardt, J., Santos-Martins, D., Tillack, A.F., & Forli, S. (2021). AutoDock Vina 1.2.0: New Docking Methods, Expanded Force Field, and Python Bindings. *Journal of chemical information and modeling*, *61*(8), 3891-3898. https://doi.org/10.1021/acs.jcim.1c00203

Enkler, L., Richer, D., Marchand, A.L., Ferrandon, D., & Jossinet, F. (2016). Genome engineering in the yeast pathogen Candida glabrata using the CRISPR-Cas9 system. *Scientific reports*, *6*, 35766. https://doi.org/10.1038/srep35766

Guinea, J. (2014). Global trends in the distribution of Candida species causing candidemia. *Clinical microbiology and infection : the official publication of the European Society of Clinical Microbiology and Infectious Diseases, 20 Suppl 6*, 5–10. https://doi.org/10.1111/1469-0691.12539

Gupta, P., Gautam, P., Rai, N., & Kumar, N. (2012). An Emerging Hope to Combat Candida albicans: Plant Based Therapeutics. *Biotechnology International*, *5*, 85-114.

Jensen, R., Johansen, H., Søes, L.M., Lemming, L.E., Rosenvinge, F., Nielsen, L., Olesen, B., Kristensen, L., Dzajic, E., & Astvad, K.J.A.A. (2015). Posttreatment antifungal resistance among colonizing Candida isolates in candidemia patients: results from a systematic multicenter study. *Antimicrobial agents and chemotherapy*, *60*(3), 1500-1508. https://doi.org/10.1128/AAC.01763-15

McCarty, T.P., & Pappas, P.G. (2016). Invasive candidiasis. *Infectious disease clinics of North America, 30*(1), 103-124. https://doi.org/10.1016/j.idc.2015.10.013

Morris, G.M., Huey, R., Lindstrom, W., Sanner, M.F., Belew, R.K., Goodsell, D.S., & Olson, A.J. (2009). AutoDock4 and AutoDockTools4: Automated docking with selective receptor flexibility. *Journal of computational chemistry*, *30*(16), 2785–2791. https://doi.org/10.1002/jcc.21256

Mota, S., Alves, R., Carneiro, C., Silva, S., Brown, A.J., Istel, F., Kuchler, K., Sampaio, P., Casal, M., Henriques, M., & Paiva, S. (2015). Candida glabrata susceptibility to antifungals and phagocytosis is modulated by acetate. *Frontiers in microbiology*, *6*, 919. https://doi.org/10.3389/fmicb.2015.00919

Pfaller, M.A., & Diekema, D.J. (2007). Epidemiology of invasive candidiasis: a persistent public health problem. *Clinical microbiology reviews*, *20*(1), 133-163. https://doi.org/10.1128/CMR.00029-06

Seyedmousavi, S., İlkit, M., Durdu, M., Ergin, Ç., Polat, S.H., Melchers, W., & Verweıj, P. (2015). Candida and Candidosis: Updates on Epidemiology, Diagnosis, Treatment, Antifungal Drug Resistance, and Host Genetic Susceptibility. *Türk mikrobiyoloji cemiyeti dergisi*, *45*(1), 1-11. https://doi.org/10.5222/TMCD.2015.001

Tamo, S.P.B. (2020). Candida Infections: Clinical Features, Diagnosis and Treatment. *Infectious diseases& clinical microbiology*, *2*, 91-103. https://doi.org/10.36519/idcm.2020.0006

Timmermans, B., De Las Peñas, A., Castaño, I., & Van Dijck, P. (2018). Adhesins in *Candida glabrata*. *Journal of fungi (Basel, Switzerland)*, *4*(2), 60. https://doi.org/10.3390/jof4020060

Weig, M., Jansch, L., Groß, U., De Koster, C.G., Klis, F.M., & De Groot, P.W.J. (2004). Systematic identification in silico of covalently bound cell wall proteins and analysis of protein–polysaccharide linkages of the human pathogen *Candida glabrata*. *Microbiology (Reading, England)*, *150*(Pt 10), 3129–3144. https://doi.org/10.1099/mic.0.27256-0

EUCHEMBIOJ

THE EUROPEAN CHEMISTRY AND BIOTECHNOLOGY JOURNAL

Eur. Chem. Biotechnol. J. 1: 39-46 (2024) www.euchembioj.com

Research article

Salt-assisted liquid–liquid microextraction for determination of haloperidol in human plasma by LC-MS/MS

Selen Al[1] | ORCID 0009-0009-2014-1998 | ayseselen.al@ogr.iu.edu.tr

Aykut Kul[1*] | ORCID 0000-0002-1195-0939 | aykut.kul@istanbul.edu.tr

Olcay Sagirli[1] | ORCID 0000-0002-0434-2150 | osagirli@istanbul.edu.tr

[1]**Department of Analytical Chemistry, Faculty of Pharmacy, Istanbul University, 34452 Istanbul, Türkiye**

*****Corresponding author: aykut.kul@istanbul.edu.tr; Ph.: +90-212-440-0000; Fax: +90-212-440-0252.

Received: 20.10.2023
Accepted: 06.12.2023
Published: 02.01.2024

Cite this article: Al, S., Kul, A., & Sagirli, O. (2024). Salt-assisted liquid–liquid microextraction for determination of haloperidol in human plasma by LC-MS/MS. *The European chemistry and biotechnology journal*, *1*, 39-46. https://doi.org/10.62063/ecb-16

Abstract

Haloperidol is an antipsychotic used in the treatment of schizophrenia. Compared to other antipsychotics, it is widely used in developing countries due to its affordable price. Haloperidol has a narrow therapeutic range and variable pharmacokinetics; therefore, therapeutic drug monitoring (TDM) is recommended. For this reason, in this study, an easily applicable, fast, selective, accurate, reliable, and economical LC-MS/MS method was developed for the determination of haloperidol in human plasma for use in TDM and also method was validated according to European Medicines Agency (EMA) Bioanalytical method validation guidelines. In the developed method, analyte and internal standard were extracted from plasma by salt-assisted liquid-liquid microextraction (SALLME) technique and after that injected to the LC system. The limit of quantification of haloperidol was determined as 1 ng/ml. The calibration curve was validated between 1-15 ng/ml, with correlation coefficients >0.99. In addition, the developed method was used to determine drug concentration levels in the plasma of real patients.

Keywords: haloperidol, LC-MS/MS, SALLME, TDM

Introduction

Haloperidol is a butyrophenone derivative antipsychotic agent used in the treatment of schizophrenia and related psychoses (Lee et al., 2007). It was synthesized in 1958 and first marketed in the United States in 1967 (Gerace et al., 2012). While there is a wide choice of antipsychotics, some very expensive, in developed countries, older and less expensive drugs such as haloperidol is still widely used in developing countries (Leucht et al., 2008). Although haloperidol is frequently prescribed and often used as a comparator in clinical trials, both acute and long-term use can cause extrapyramidal

side effects such as dystonia, dyskinesia and parkinsonism (Grubor et al., 2020). This drug exerts its therapeutic effect through D2 receptor antagonism, as with other antipsychotic drugs (Tyler et al., 2017). It has a rapid onset of action and an extensive volume of tissue distribution. It is also lipophilic and highly protein bound (Wang et al. 2012). Only 1% of the administered dose of haloperidol is excreted unchanged in the urine because the drug is extensively metabolized in the liver (Gassó et al., 2013). Its metabolism includes conversion to an “inactive metabolite” (50/60%) by glucuronidation, to “reduced haloperidole” (an active metabolite - 23%) by reduction and back oxidation, and to a “pyridium metabolite” (a toxic metabolite 20/30%) by N-dealkylation (Vella-Brincat and Macleod 2004). The CYP2D6 genotype has an important role in the excretion of “haloperidol” and “reduced haloperidol” and may pose a risk of serious adverse effects. In addition, body weight, and smoking may cause changes in pharmacokinetics (Brockmöller et al., 2002). Haloperidol can be used with a variety of medications such as antipsychotics, antidepressants, and benzodiazepines (Shin et al. 2001). Combination antipsychotic therapy is a common practice, but it also has effects such as drug-drug interactions, variability in serum levels, and difficulties in patient adherence to treatment (Lally and MacCabe 2015). Because of this variable pharmacokinetics and narrow therapeutic range, haloperidol therapy requires personalized optimization. For this reason, therapeutic drug monitoring is recommended for haloperidol (Kudo and Ishizaki 1999). The recommended plasma concentration for haloperidol is 1-10 ng/mL, while the alert level is 15 ng/mL (Hiemke et al., 2018). Therapeutic drug monitoring (TDM) helps the clinician reach targeted concentrations and direct dosage to reduce the risk of side effects (Eliasson et al. 2013). TDM is performed by chromatographic and immunoassay methods, but in immunoassays the presence of various other components in the sample can lead to a lack of analytical specificity (Ates et al., 2020). For this reason, reliable, sensitive, high-quality analytical methods by instruments combined with Ultraviolet (UV), Fluorescent (FL), and mass spectrometry (MS) detectors are the main techniques used for TDM (Tuzimski and Petruczynik 2020).

Salt-assisted liquid liquid microextraction (SALLME) is a simple, fast and easily applicable sample preparation technique that uses various salts and water-miscible organic solvents (Gupta et al. 2009). Currently, there is a lack of any SALLME technique in the literature for the determination of haloperidol in human plasma. Therefore, the aim of this study was to develop a rapid, economical and easily applicable LC-MS/MS method for the determination of haloperidol in human plasma using SALLME technique.

Materials and methods

Materials and reagents

Haloperidol, haloperidol-d4, sodium hydroxide, sodium chloride, and organic solvents were procured from Merck (Darmstadt, Germany). Water was purified by a Purelab option-Q water system from Elga (Elga, Lane End, UK).

Stock solutions of haloperidol were prepared separately in methanol at a 1 mg/mL concentration. A working standard solution was prepared by diluting the stock standard solutions with an appropriate volume of methanol. Calibration standards and quality control samples were prepared by spiking the (internal standard) IS and working standard solution into blank plasma. The concentrations of the calibration standard solutions were 1, 2, 4, 6, 8, 10, 13, and 15 ng/mL, while the concentrations of the quality control samples were 1, 3, 7.5,12 ng/mL. All solutions were kept at -20°C when not in use.

Sample preparation

The salt-assisted liquid-liquid microextraction technique was followed for cleaning the plasma samples. The sample preparation procedure is shown in Figure 1.

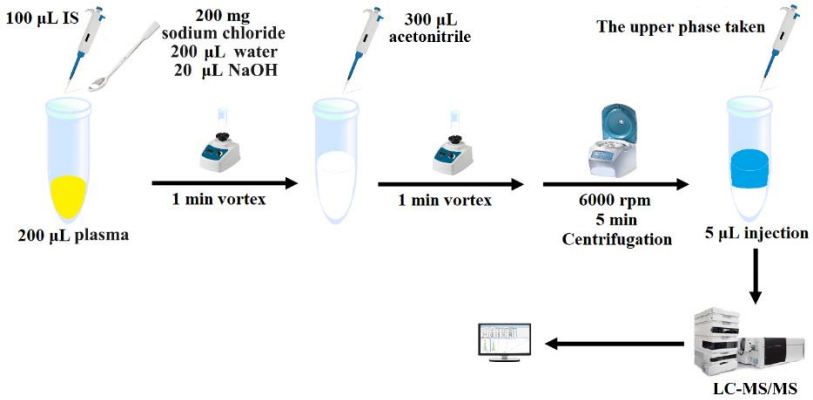

Figure 1. Sample preparation.

LC-MS/MS analysis

The method was performed on an Agilent 1200 series HPLC system coupled to an Agilent 6460 triple quadrupole tandem mass spectrometry with an InterSustain C18 (3.0 µm, 3.0× 100 mm) column. The column temperature and the injection volume were 30 °C and 5 µL respectively. The isocratic elution was performed using mobile phase A (water with 0.1% formic acid) and mobile phase B (acetonitrile with 0.1% formic acid) (60:40). The total run time was 4 min with flow rate of 0.4 mL/min. The desolvation gas temperature, nebulizer, and desolvation gas flow were set at 300 °C, 45 psi, 11 L/min. The typical ion transitions were 376.2→ 165.1 for haloperidol and m/z 380.2→169.0 for haloperidol-d4. Analytes were detected using electrospray ionization in the positive mode.

Validation of the method

Method validation was performed to evaluate the selectivity, lower limit of quantification (LLOQ), precision, accuracy, dilution integrity, matrix effects, carryover, calibration curve performance, and stability, according to European Medicines Agency (EMA) Bioanalytical Method Validation Guideline (EMA 2011). Selectivity is the ability of the method to separate the analyte from other substances in the matrix. For this purpose, blank plasmas from six different sources were analyzed and examined for any interference. The lower limit of quantification (LLOQ) is the lowest concentration of analyte that can be measured in a sample with acceptable accuracy, reliability, and precision. LLOQ was determined by considering the therapeutic range of the analyte. Accuracy and precision parameters were assessed by preparing quality control samples at 4 different concentrations (LLOQ, low-QC, medium-QC, and high-QC) and analyzing them six times on three different days. Calibration curve performance was evaluated using 8 different calibration concentration levels for the analyte and the calibration curve was defined between the lower limit of quantification and upper limit of quantification (ULOQ). Carryover was evaluated by injecting a blank sample after the standard at the upper limit of quantification. Dilution integrity was assessed by diluting a sample with a higher concentration than the ULOQ sample to within the range of the calibration curve. The stability parameter was evaluated using freshly prepared samples of the analytes and internal standard under 3 different conditions (4 weeks at -20°C, 24 hours in autosampler, 3 times freeze-thaw). In the matrix effect study, low and high QC samples were prepared in the plasma matrix and the solution obtained from six different sources was analyzed. The matrix effect was calculated by proportioning the response values obtained.

Sample analysis

The developed method has been successfully applied to plasma samples from patients on drug therapy.

Results and discussion

Method optimization

In this study, various amounts of sodium chloride salt (150, 200, and 300 mg), organic solution types (acetonitrile and ethyl acetate), and volumes (300, 400, and 500 µL) were tested for phase separation. 200 mg of sodium chloride and 300 µL acetonitrile produced the best yield.

Method validation

No interference was detected in the retention time of the analytes and internal standard in blank plasma. The retention times for the internal standard and haloperidol (Figure 2). The lower limit of quantification of haloperidol was determined as 1 ng/mL. The calibration curves were validated between 1-15 ng/mL for haloperidol, with correlation coefficients >0.99. No interference was detected in the blank plasma injected after the ULOQ sample.

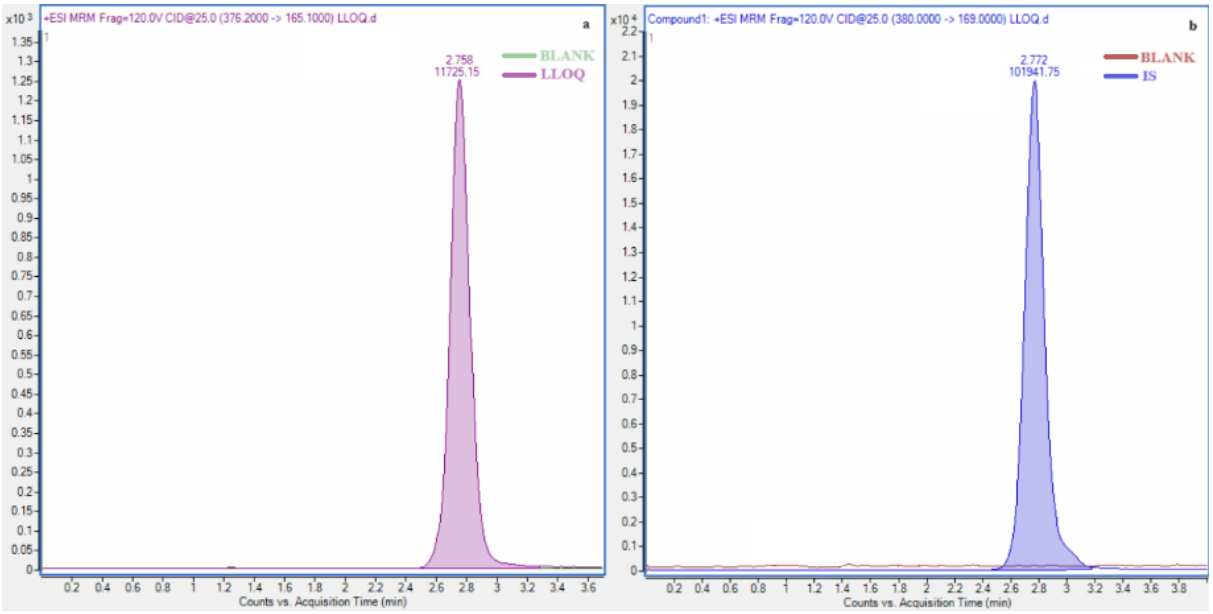

Figure 2. Chromatograms of the haloperidol (a) and IS (b).

All accuracy and precision values are given in Table 1. It is seen that the results comply with the EMA criteria.

Table 1. Accuracy and precision data for haloperidol.

QC concentration (ng/mL)	Intra-assay (n=6)		Inter-assay (n=18)	
	Accuracy (%)	CV (%)	Accuracy (%)	CV (%)
1 (LLOQ)	102.9	4.4	96.3	4.2
3 (low)	103.1	2.1	106.8	2.9
7.5 (medium)	106.4	3.8	100.9	3.5
12 (high)	102.5	5.7	106.3	4.8

QC: quality control, LLOQ: lower limit of quantification, CV: coefficient of variation

The accuracy and precision of the diluted samples were 101.7% and 3.4% for haloperidol. The accuracy values of the stability analyses for haloperidol and the internal standard are shown in Table 2. The results comply with EMA acceptance criteria.

Table 2. The stability of haloperidol in plasma.

QC concentration (ng/mL)	Stability (% Accuracy)		
	24 hours in the autosampler (n=6)	4 weeks at −20 °C (n=6)	three freeze-thaw cycles (n=6)
3 (low)	104.3	102.9	108.7
12 (high)	105.1	103.1	106.5

QC: quality control

The matrix effect results were within EMA's acceptable ranges (CV, 15%) (Table 3).

Table 3. The matrix effect data of haloperidol.

QC concentration (ng/mL)	*Normalized matrix effect factor (n=6)						CV (%)
3 (low)	1.0	1.0	1.0	1.1	1.0	1.1	5.0
12 (high)	1.0	1.1	1.0	1.0	0.9	1.0	6.3

QC: quality control, CV: coefficient of variation

Application to real sample

Five actual samples were successfully used to test the developed method. Table 4 presents all results.

Table 4. The results of the samples.

Sample	Age	Dose of haloperidol	Concentration of plasma (ng/mL)
Sample-1	19	5 mg	5.5
Sample-2	44	10 mg	2.4
Sample-3	14	10 mg	9.9
Sample-4	46	10 mg	2.3
Sample-5	24	10 mg	1.4

Method comparison

There are various LC-MS/MS methods in the literature for the determination of haloperidol in plasma and serum. These methods have various sample preparation techniques such as protein precipitation (Juenke et al. 2013, Gradinaru et al., 2014, Domingues et al., 2016, Cao et al. 2020), liquid-liquid extraction (Remane et al., 2011, Montenarh et al., 2016, Degreef et al., 2021), and solid phase extraction (Hempenius et al., 1999, Khelfi et al., 2018). Among these sample preparation techniques, protein precipitation is relatively easy but it has a low recovery. Liquid-liquid extraction requires the use of a lot of organic solvents, while solid-phase extraction is quite expensive compared to these methods. The Sample preparation technique presented in this study is not only easy to apply but also more environmentally friendly as it uses less organic solvents.

Conclusions

The LC-MS/MS method developed using the SALLME technique is simple, accurate, and precise. The values of the European Medicines Agency's bioanalytical method validation parameters are acceptable and therefore, the method is suitable for the therapeutic drug monitoring of haloperidol. Additionally, the SALLME technique can be used as an extraction method in many biotechnological studies.

Acknowledgements

Not applicable.

Funding

Not applicable.

Conflict of interest

The authors declare no conflict of interest.

Data availability statement

Data can be obtained from the corresponding author upon a reasonable request.

Ethics committee approval

The study was approved by the Ethics Committee of the University of Üsküdar (No. 7 of 29.07.2021) and was conducted in accordance with the Helsinki Declaration.

Authors' contribution statement

The authors acknowledge their contributions to this paper as follows: **Study conception and design**: O.S., A.K.; **Data collection**: S.A.; **Analysis and interpretation of results**: S.A.; **Manuscript draft preparation**: A.K. All authors reviewed the results and approved the final version of the manuscript.

References

Agency, E.M., 2011. Guideline on bioanalytical method validation. EMEA/CHMP/EWP/192217/2009.

Ates, H. C., Roberts, J. A., Lipman, J., Cass, A. E. G., Urban, G. A., & Dincer, C. (2020). On-site therapeutic drug monitoring. *Trends in biotechnology*, *38*(11), 1262-1277. https://doi.org/10.1016/j.tibtech.2020.03.001

Brockmöller, J., Kirchheiner, J., Schmider, J., Walter, S., Sachse, C., Müller-Oerlinghausen, B., & Roots, I. (2002). The impact of the CYP2D6 polymorphism on haloperidol pharmacokinetics and on the outcome of haloperidol treatment. *Clinical pharmacology and therapeutics*, *72*(4), 438-452. https://doi.org/10.1067/mcp.2002.127494

Cao, Y., Zhao, F., Chen, J., Huang, T., Zeng, J., Wang, L., Sun, X., Miao, Y., Wang, S., & Chen, C. (2020). A simple and rapid LC-MS/MS method for the simultaneous determination of eight antipsychotics in human serum, and its application to therapeutic drug monitoring. Journal of chromatography. B, Analytical technologies in the biomedical and life sciences, 1147, 122129. https://doi.org/10.1016/j.jchromb.2020.122129

Degreef, M., Berry, E. M., Maudens, K. E. K., & van Nuijs, A. L. N. (2021). Multi-analyte LC-MS/MS quantification of 38 antipsychotics and metabolites in plasma: Method validation & application to routine analyses. *Journal of chromatography. B, Analytical technologies in the biomedical and life sciences*, *1179*, 122867. https://doi.org/10.1016/j.jchromb.2021.122867

Domingues, D. S., Pinto, M. A., de Souza, I. D., Hallak, J. E., Crippa, J. A., & Queiroz, M. E. (2016). Determination of Drugs in Plasma Samples by High-Performance Liquid Chromatography-Tandem

Mass Spectrometry for Therapeutic Drug Monitoring of Schizophrenic Patients. *Journal of analytical toxicology*, *40*(1), 28-36. https://doi.org/10.1093/jat/bkv107

Eliasson, E., Lindh, J. D., Malmström, R. E., Beck, O., & Dahl, M. L. (2013). Therapeutic drug monitoring for tomorrow. *European journal of clinical pharmacology*, *69 Suppl 1*, 25-32. https://doi.org/10.1007/s00228-013-1504-x

Gassó, P., Papagianni, K., Mas, S., de Bobadilla, R. F., Arnaiz, J. A., Bernardo, M., & Lafuente, A. (2013). Relationship between CYP2D6 genotype and haloperidol pharmacokinetics and extrapyramidal symptoms in healthy volunteers. *Pharmacogenomics*, *14*(13), 1551-1563. https://doi.org/10.2217/pgs.13.150

Gerace, E., Salomone, A., Pellegrino, S., & Vincenti, M. (2012). Evidence of Haldol (haloperidol) long-term intoxication. *Forensic science international*, *215*(1-3), 121-123. https://doi.org/10.1016/j.forsciint.2011.01.038

Gradinaru, J., Vullioud, A., Eap, C. B., & Ansermot, N. (2014). Quantification of typical antipsychotics in human plasma by ultra-high performance liquid chromatography tandem mass spectrometry for therapeutic drug monitoring. *Journal of pharmaceutical and biomedical analysis*, *88*, 36-44. https://doi.org/10.1016/j.jpba.2013.07.041

Grubor, M., Zivkovic, M., Sagud, M., Nikolac Perkovic, M., Mihaljevic-Peles, A., Pivac, N., Muck-Seler, D., & Svob Strac, D. (2020). HTR1A, HTR1B, HTR2A, HTR2C and HTR6 Gene Polymorphisms and Extrapyramidal Side Effects in Haloperidol-Treated Patients with Schizophrenia. *International journal of molecular sciences*, *21*(7), 2345. https://doi.org/10.3390/ijms21072345

Gupta, M., Jain, A., & Verma, K. K. (2009). Salt-assisted liquid-liquid microextraction with water-miscible organic solvents for the determination of carbonyl compounds by high-performance liquid chromatography. *Talanta*, *80*(2), 526-531. https://doi.org/10.1016/j.talanta.2009.07.021

Hempenius, J., Steenvoorden, R. J., Lagerwerf, F. M., Wieling, J., & Jonkman, J. H. (1999). 'High throughput' solid-phase extraction technology and turbo ionspray LC-MS-MS applied to the determination of haloperidol in human plasma. *Journal of pharmaceutical and biomedical analysis*, *20*(6), 889-898. https://doi.org/10.1016/s0731-7085(99)00107-7

Hiemke, C., Bergemann, N., Clement, H. W., Conca, A., Deckert, J., Domschke, K., Eckermann, G., Egberts, K., Gerlach, M., Greiner, C., Gründer, G., Haen, E., Havemann-Reinecke, U., Hefner, G., Helmer, R., Janssen, G., Jaquenoud, E., Laux, G., Messer, T., Mössner, R., … Baumann, P. (2018). Consensus Guidelines for Therapeutic Drug Monitoring in Neuropsychopharmacology: Update 2017. *Pharmacopsychiatry*, *51*(1-02), e1. https://doi.org/10.1055/s-0037-1600991

Juenke, J. M., Brown, P. I., Urry, F. M., Johnson-Davis, K. L., & McMillin, G. A. (2013). Simultaneous UPLC-MS/MS assay for the detection of the traditional antipsychotics haloperidol, fluphenazine, perphenazine, and thiothixene in serum and plasma. *Clinica chimica acta; international journal of clinical chemistry*, *423*, 32-34. https://doi.org/10.1016/j.cca.2013.04.014

Khelfi, A., Azzouz, M., Abtroun, R., Reggabi, M., & Alamir, B. (2018). Determination of Chlorpromazine, Haloperidol, Levomepromazine, Olanzapine, Risperidone, and Sulpiride in Human Plasma by Liquid Chromatography/Tandem Mass Spectrometry (LC-MS/MS). *International journal of analytical chemistry*, 2018, 5807218. https://doi.org/10.1155/2018/5807218

Kudo, S., & Ishizaki, T. (1999). Pharmacokinetics of haloperidol: an update. *Clinical pharmacokinetics*, *37*(6), 435-456. https://doi.org/10.2165/00003088-199937060-00001

Lally, J., & MacCabe, J. H. (2015). Antipsychotic medication in schizophrenia: a review. *British medical bulletin*, *114*(1), 169-179. https://doi.org/10.1093/bmb/ldv017

Lee, Y., Wang, P. K., Lai, H. Y., Yang, Y. L., Chu, C. C., & Wang, J. J. (2007). Haloperidol is as effective as ondansetron for preventing postoperative nausea and vomiting. *Canadian journal of anaesthesia = Journal canadien d'anesthesie*, *54*(5), 349–354. https://doi.org/10.1007/BF03022656

Leucht, C., Kitzmantel, M., Chua, L., Kane, J., & Leucht, S. (2008). Haloperidol versus chlorpromazine for schizophrenia. *The Cochrane database of systematic reviews*, (1), CD004278. https://doi.org/10.1002/14651858.CD004278.pub2

Montenarh, D., Hopf, M., Maurer, H. H., Schmidt, P., & Ewald, A. H. (2016). Development and validation of a multi-analyte LC-MS/MS approach for quantification of neuroleptics in whole blood, plasma, and serum. *Drug testing and analysis*, *8*(10), 1080-1089. https://doi.org/10.1002/dta.1923

Remane, D., Meyer, M. R., Wissenbach, D. K., & Maurer, H. H. (2011). Ultra high performance liquid chromatographic-tandem mass spectrometric multi-analyte procedure for target screening and quantification in human blood plasma: validation and application for 31 neuroleptics, 28 benzodiazepines, and Z-drugs. *Analytical and bioanalytical chemistry*, *401*(4), 1341-1352. https://doi.org/10.1007/s00216-011-5187-9

Shin, J. G., Kane, K., & Flockhart, D. A. (2001). Potent inhibition of CYP2D6 by haloperidol metabolites: stereoselective inhibition by reduced haloperidol. *British journal of clinical pharmacology*, *51*(1), 45-52. https://doi.org/10.1046/j.1365-2125.2001.01313.x

Tuzimski, T., & Petruczynik, A. (2020). Review of Chromatographic Methods Coupled with Modern Detection Techniques Applied in the Therapeutic Drugs Monitoring (TDM). *Molecules (Basel, Switzerland)*, *25*(17), 4026. https://doi.org/10.3390/molecules25174026

Tyler, M. W., Zaldivar-Diez, J., & Haggarty, S. J. (2017). Classics in Chemical Neuroscience: Haloperidol. *ACS chemical neuroscience*, *8*(3), 444–453. https://doi.org/10.1021/acschemneuro.7b00018

Vella-Brincat, J., & Macleod, A. D. (2004). Haloperidol in palliative care. *Palliative medicine*, *18*(3), 195–201. https://doi.org/10.1191/0269216304pm881oa

Wang, E. H., Mabasa, V. H., Loh, G. W., & Ensom, M. H. (2012). Haloperidol dosing strategies in the treatment of delirium in the critically ill. *Neurocritical care*, *16*(1), 170–183. https://doi.org/10.1007/s12028-011-9643-3

EUCHEMBIOJ

THE EUROPEAN CHEMISTRY AND BIOTECHNOLOGY JOURNAL

Eur. Chem. Biotechnol. J. 1: 47-57 (2024) www.euchembioj.com

Research article

Stable and high voltage and power output of CEA-MFCs internally connected in series (iCiS-MFC)

Yanzhen Fan[1#] | fanyanzhen@gmail.com

Anthony Janicek[1#] | a.janicek@gmail.com

Hong Liu[1*] | ORCID 0000-0001-6083-4101 | hong.liu@oregonstate.edu

[1]Biological and Ecological Engineering, Oregon State University, Corvallis, OR 97333, USA

*****Corresponding author: E-mail: hong.liu@oregonstate.edu; Ph.: +1-541-737-6309. # Authors contributed equally to work.

Received: 09.11.2023
Accepted: 27.12.2023
Published: 02.01.2024

Cite this article: Fan, Y., Janicek, A., & Liu, H. (2024). Stable and High Voltage and Power Output of CEA-MFCs Internally Connected in Series (iCiS-MFC). *The European chemistry and biotechnology journal*, *1*, 47-57. https://doi.org/10.62063/ecb-17

Abstract

The voltage output of a single MFC is normally less than 0.8 V, often less than 0.3 V at maximum power output, which greatly limits the application of MFCs. When MFCs are scaled up, however, increasing reactor size has typically resulted in decreased power density. In this study, we developed a novel MFC configuration that contains multiple cloth electrode assemblies in which the MFCs were internally connected in series (iCiS-MFC). The iCiS-MFC, equivalent to 3 CEA-MFCs, produced a high voltage output over 1.8 V and a maximum power density of 3.5 W m^{-2} using carbon cloth cathodes containing activated carbon as the catalyst. This power density is 6% higher than that reported for a similar smaller CEA-MFC, indicating that power can be maintained during scale-up with a greater than 33-fold increase in total cathode surface area and greater than 20-fold increase in reactor volume. High stability was also demonstrated based on the performance of the iCiS-MFC over a period of one year of operation. The high power and stability is likely due, in part, to a more efficient means of current collection through the internal series connection, which also avoids the use of expensive current collectors. These results clearly demonstrate the great potential of this MFC design for further scaling-up.

Keywords: activated carbon, cloth electrode assembly, internally connected in series, microbial fuel cell, scaling-up

Introduction

There is a significant cost associated with wastewater treatment, which is largely attributable to energy consumption (Logan and Rabaey, 2012). On the other hand, wastewater contains several times more energy than needed for its treatment. Releasing energy stored in the high organic content in domestic, industrial, and agricultural wastewaters represent a potential means to offset this high cost and even for energy production (Perlack et al., 2005). With an ever-increasing demand for wastewater treatment

compounded by the enormous cost associated with treatment plant operation, finding more efficient and cost effective means of treating wastewater has become more important than ever. Developing new treatment technologies which will off-set this high-energy cost is necessary to maintain both water and energy security.

Microbial fuel cell (MFC) technology represents one such alternative. Despite its great potential, some researchers lose confidence on the future of MFC for wastewater treatment and energy recovery, primarily due to the great challenge in scaling-up (Logan et al., 2015). For example, compared with our previous reported 0.03L (liquid volume) MFC producing maximum power output of 62.3 mW, the total maximum power of 90L, 100L and 250L MFCs were only slightly higher: 82 mW, 114 mW, and 116 mW, respectively (Feng et al., 2014; Ge et al., 2015; Dong et al., 2015). Although media composition and our experimental conditions contributed the 3-4 orders of magnitude difference in volumetric power density, the main reason should be the difference in reactor architecture.

There are two general strategies for scaling-up MFCs: increasing the size of individual MFCs and connecting multiple MFCs into a stack (Cheng et al., 2014; Aelterman et al., 2006). Unfortunately, increasing individual reactor size typically results in decreased power generation measured in both volumetric power density and surface power density (Janicek et al., 2014; Dekker et al., 2009)[i,ii]. The decrease in surface power density might be caused by considerable potential loss over large commonly used carbon cloth electrodes, which can be as high as 0.35 V, or about 50% of open circuit potential, for carbon cloth of 1 meter long (Cheng et al., 2014). Another possible cause of the decrease in surface power density is the large internal resistance due to increased anode-cathode spacing, as Ohmic potential loss is proportional to electrode spacing (Fan et al., 2008). In addition to the decrease in surface power density, the decrease in volumetric power density is amplified by the much lower surface/volume ratio of the large individual MFC. Therefore, connecting multiple MFCs into a stack might be the only choice to scale-up MFC while maintaining its performance (Ieropoulos et al., 2008; Wang et al., 2011).

When connected into a stack, MFCs can be connected electrically in series to increase voltage. The open circuit voltage of an individual air cathode MFC is around 0.8V with an operating voltage less than 0.4 V at its maximum power output due to electrochemical losses. Such a low voltage output greatly limits the practical application of MFCs for power generation. Increasing voltage output through series electrical connection has the potential to result in lower power loss compared to other means of boosting voltage due to the lack of conversion energy loss. Serial connection, producing higher voltage but lower current than parallel connection, may also lead to lower power loss in electricity collection and transmission. However, in spite of many attempts, current MFC stack designs have not achieved the ideal voltage output with an overall voltage decrease ranging from 30-98% for serial connection of 2-4 MFCs (Dekker et al., 2009; Gurung et. al., 2012; Oh and Logan 2007; Gurung and Oh 2012). Using power managing system can booster voltage output of parallel connected MFCs, however, the addition of another system can further increase the complexity, thus reduce the reliability of MFC system. Furthermore, the maximum power density or energy output might be affected significantly (Donovan et al., 2011; Adami et al., 2013; Zhu et al., 2011; Wu et al., 2012). A more efficient MFC stack design capable of high power and voltage outputs are critical for successful scaling up of MFC technology.

Among the various MFC designs, the cloth electrode assembly (CEA)-MFC, which contains a compact electrode/separator design resulting in minimized electrode spacing, has demonstrated high performance and treatment efficiency at several milliliter scales (Fan et al., 2012; Janicek et al., 2015a; Fan et al., 2007). This reactor design replaces the membranes with low-cost and low-resistance cloth separators, thus lowering its contribution to the internal resistance of MFCs and greatly increasing the performance of MFCs (Janicek et al., 2015a). The CEA design also has great advantage over other MFC designs in terms of maintaining its performance during scale-up, as the electrode spacing is fixed and thus keeps the specific internal resistance as low as 20 $m\Omega\ m^2$ (Fan et al., 2008). A stable power density of 3.3 Wm^{-2} was achieved using activated carbon as cathode catalyst during 24 days of operation in batch mode (Janicek et al., 2015b). The high power, relatively low-cost, good scale-up potential, and stability of CEA-MFCs suggest that this configuration may be the best option for MFC stack development.

When MFC are scaled up or connected into stacks, a current collector is typically required to reduce ohmic losses of the electrode (Logan 2010). Although MFCs operate at low current densities, the energy loss can be as much 2 orders of magnitude greater when single point connection is used compared to optimized connections in a larger scale operation (electrode area of 1 m^2) (Cheng et al., 2014). Current

collectors can either be incorporated as the electrode base material or can be a separate wire or mesh that attaches to the electrode base material (Wei et al., 2011). In MFCs, current collectors have been made from titanium mesh, titanium wire, graphite plates, gold, and stainless-steel mesh (Logan 2010; Wei et al., 2011). Use of stainless steel may not be suitable for MFC applications due to the potential for severe corrosion, which ultimately leads to reduced performance (Janicek et al., 2015a). Precious metal current collectors are also cost prohibitive for scaling up MFC technology. As a result, a more efficient means of current collection is needed while avoiding the use of expensive or unstable current collectors.

In this study, we present a new MFC stack configuration, CEA-MFCs internally connected in serial (iCiS-MFC), in which the anode and the adjacent cathode share the same base material, i.e. carbon cloth, avoiding the need of a current collector. An iCiS-MFC equivalent to 3 MFCs was built and operated for approximately one year to demonstrate its long-term stability in producing high voltage output and power density.

Materials and methods

Reactor design and construction

A double iCiS air-cathode CEA-MFCs (3 on each side) was constructed with a total effective surface area of 480 cm^2 (for the double CEA-MFC) and a liquid volume of 240 ml (Figure 1a). Each CEA-MFC was placed in between 3 PVC frames. The internal frame, which served as the anode chamber, contained 3 openings measuring 20 cm by 4 cm by 1 cm. Cathodes and anodes were internally connected and made from the same piece of carbon cloth (CCP, fuelcellearth.com) (Figure 1b). The end MFC's electrodes were connected to the external circuit via a titanium wire, forming a double iCiS-MFC stack with 3 MFC connected in series on the top (designated as Stack A) and 3 on the bottom (designated as Stack B) (Figure 1a). A non-woven fabric layer was sandwiched between the anode and cathode of each CEA-MFC as previously described (Fan et al., 2012). In order to prevent gas from becoming trapped between the anode and cathode, 1 cm x 1 cm slits, as previously described, were cut into the anode to provide a means for gas to be released (Fan et al., 2012). Carbon cloth cathodes were constructed as previously described with an activated carbon loading of 25 mg cm^{-2} (Janicek et al., 2015b). Each MFC was labeled according to the position in Stack A (MFC1, MFC2, MFC3) and Stack B (MFC1, MFC2, MFC3) according to Figure 1a.

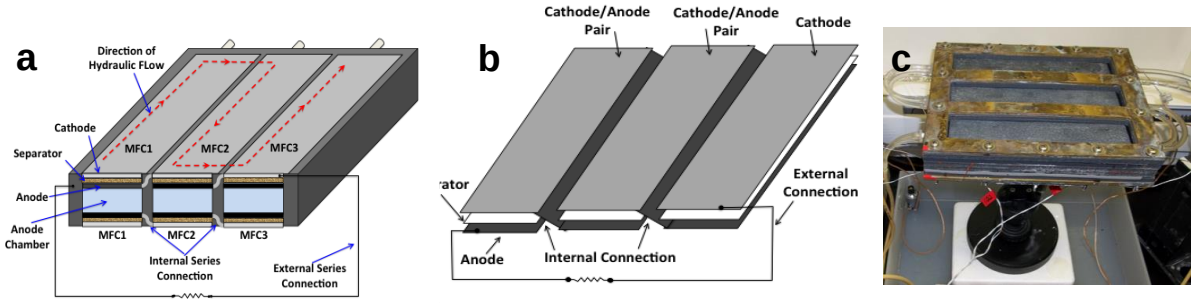

Figure 1. (a) Schematic of iCiS-MFC stacks containing 3 CEA-MFCs connected internally in series on the bottom initially (Stack A) and 3 on the top initially (Stack B). Also shown are the internal and external electrical connections, direction of hydraulic flow, and position/naming of individual MFCs within the reactor; (b) Schematic showing the anode/cathode pairs, each made from a single piece of carbon cloth (resulting in the internal electrical connection); and (c) photograph of the reactor.

MFC operation and analysis

The MFC was inoculated with a mixed bacterial culture as previously described (Fan et al., 2012). Acetate (5.9 g/L or 0.59 g/L) was used as the substrate and the medium solution contained the following (per liter), unless otherwise specified: NH_4Cl, 1.5 g; KCl, 0.13 g; $NaH_2PO_4.H_2O$, 4.67 g; $Na_2HPO_4.7H_2O$, 12.4 g; and mineral (12.5 ml) and vitamin (12.5 ml) solutions as reported (Lovley and Phillips 1988). The MFC experiments were operated at 32 ± 1°C in a temperature controlled chamber. The reactor was operated hydraulically in series. The reactor was initially operated in batch mode to facilitate start-up of the reactor. The system was switched to the continuous flow mode after three days as the power

output started to increase significantly. Then the reactor was continuously fed at a flow rate of 3 ml min^{-1} maintained through a peristaltic pump, corresponding to a hydraulic retention time of 80 min (unless otherwise specified). The external resistance of both the top and bottom reactors was set to maintain an operating voltage ~ 0.9 V during normal operation. The reactor was operated for a total of 365 days. For the first 100 days the reactor was operated at 5.9 g L^{-1} (100 mM) acetate and 80 mM PBS at different HRTs to determine the optimal operating conditions at higher substrate concentration. For the next 115 days, the reactor was operated at different substrate concentrations and different HRTs to further examine the effect of operational conditions on MFC performance. For the remaining 150 days, the reactor was operated at 0.59 gL^{-1} (10 mM) acetate and 10 mM PBS at an HRT of 25 minutes to determine performance and stability at lower substrate and buffer concentration. Total stack voltage as well as the voltage of individual MFCs were monitored using a multichannel data acquisition system (2700, Keithly, USA).

Results and discussion

Start-up of the iCiS-MFC

During start-up, the resistance of the Stack A and Stack B were controlled separately and set at 1000 ohms to facilitate growth of the biofilm. The voltage of Stack A (bottom) rapidly reached a maximum of 1.72 V within 3 days of operation (Figure 2a). During this period, voltage of individual MFCs of Stack A were similar, ranging from maximum values between 0.56 V to 0.6 V during the first 3 days, with a variability of less than 7% between MFCs (Figure 2b). The resistance of Stack A, controlled using a variable resistor, was then set to maintain an operating voltage of ~ 1.5 V for another five days to further facilitate anodic biofilm development. In the following 18 days of operation, the resistance was incrementally decreased to achieve a higher power output and stabilized at operating voltage of ~ 0.9 V corresponding to approximately 0.3 V per MFC in the series.

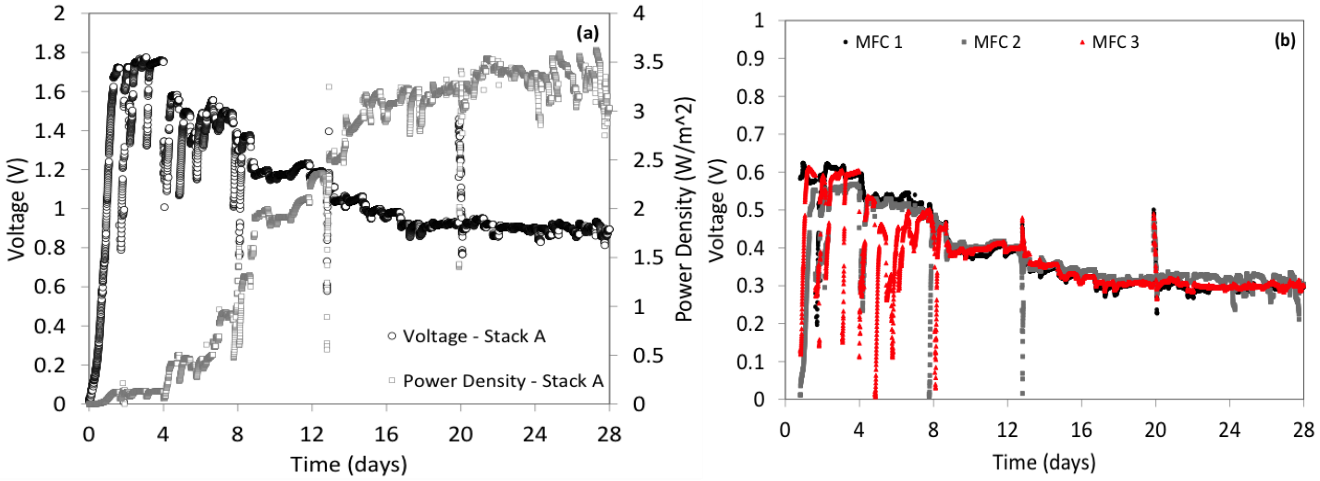

Figure 2. Voltage and power as a function of time during start-up of (a) Stack A; (b) individual cells of Stack A (bottom).

Stable power output for Stack A reached a maximum of 3.5 Wm^{-2} after 18 days of operation (Figure 2a), which was 6% higher than that previously obtained (3.3 W m^{-2}) in a significantly smaller CEA-MFC operated in batch mode (Zhu et al., 2011). This result indicates that power can be maintained during scale-up with a greater than 33-fold increase in total cathode surface area and greater than 20-fold increase in reactor volume. It should be noted that the result for the smaller scale CEA-MFC was obtained at a buffer concentration of 50 mM, which was lower than that used to obtain the result presented here (80 mM). However, previous results have shown that when buffer concentration was increased from 50 mM PBS to 100 mM PBS, in a similar smaller CEA-MFC operated under similar conditions, power density only increased 11% (Fan et al., 2012). The result presented here is also similar to that obtained when platinum was used as the cathode catalyst in a smaller CEA-MFC operated under similar conditions (Fan et al., 2012). The equivalent specific internal resistance, computed from

polarization curve, is 23.8 mΩ m^2 for Stack A (Figure S1), which is comparable to that achieved in a similar smaller reactor (Fan et al., 2012).

The voltage of Stack B (top) reached a maximum value of ~ 1.57 V at 1000 ohms resistance after 7 days of operation, which was 9% lower and took twice as long as Stack A (Figure 3a). The resistance of Stack B was then adjusted to maintain an operating voltage of ~ 1.4 V for 5 days. During this start-up period voltage of individual MFCs of Stack B were highly variable, ranging from 0.07 V to 0.77 V (Figure 3b). After this 12 day's operation, the resistance was gradually decreased until a total stack operating voltage of ~ 0.9V was achieved in approximately 20 days. However, voltage of individual MFCs remained significantly variable with 36% variability between cells. Furthermore, voltage of individual MFCs also varied between 0.25V and 0.36V. By comparison, Stack B took slightly longer to achieve a stable power output, reaching 2.2 Wm^{-2} after 20 days of operation, representing a power density 37% lower than Stack A (Figure 3a).

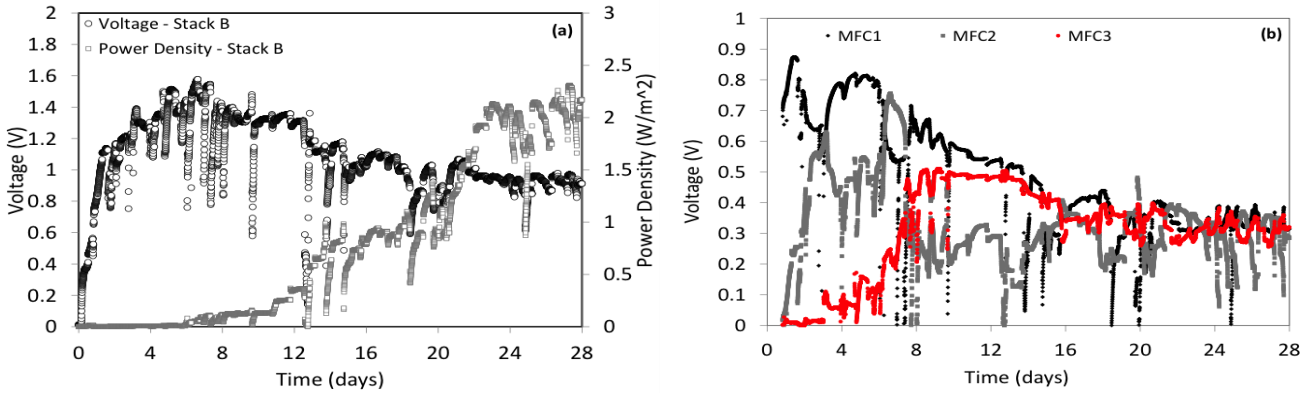

Figure 3. Voltage and power as a function of time during start-up of (a) Stack B; (b) individual cells of Stack B (top).

Effect of the stack location on performance

Due to the higher performance and faster start-up of Stack A, and the highly variable voltage of Stack B during and after start-up, it was believed that reactor location may have led to the significantly different performance of the stacks. Therefore, after 28 days of operation, the reactor was flipped so that Stack A was operating as the top reactor and Stack B was operating as the bottom reactor. Voltage of individual MFCs of Stack A (initially the bottom reactor) were similar prior to flipping the reactor (Figure 4a). However, variability in voltage between individual MFCs began to increase after the reactor was flipped, ranging from 0.23 V to 0.32 V, representing a 32% difference between individual MFCs (Figure 4a). In contrast, voltage of individual MFCs of Stack B (initially the top reactor), prior to flipping, were highly variable (Figure 4b). Once the reactors were flipped, variability in voltage decreased to only 7% between individual MFCs, ranging from 0.29 V to 0.31 V (Figure 4b). Furthermore, the decreased voltage variability corresponded to an increase in power density of Stack B (Figure 4c), which ultimately reached a maximum value of 3 Wm^{-2} after 40 days of operation (Figure S2). This represents a greater than 36% increase in power density when Stack B was operated as the bottom reactor compared to when operated as the top reactor, although it was 14% less than the maximum power achieved with Stack A before flipping. Flipping the reactors, however, had a detrimental effect on Stack A, as power density was decreased 28% to 2.5 Wm^{-2}.

The higher performance and stable voltage of Stack B when operated as the bottom reactor in combination with the decreased performance and variable voltage of Stack A after the reactors were flipped indicate that reactor location can significantly affect performance. The reduced performance when reactors are operated as the top reactor is likely due to mass transfer limitations and increased electrode spacing caused by gas being trapped within the CEA structure. Despite gas-venting slits in the anodes, when operated as the top reactor, gas is more likely to become trapped, as it will rise unless otherwise prevented. Both increased electrode spacing and mass transfer limitations; caused by gas build-up, result in increased internal resistance, which ultimately decreases performance. Distribution of trapped gas within the CEA structures would not be the same across the 3 MFCs connected in series. Gas could accumulate in one MFC faster and/or in larger quantities than in other MFCs in the series.

As a result, internal resistance of individual MFCs will be different within the Stack, ultimately leading to the highly variable voltage observed when either Stack A or Stack B was operated as the top reactor. Differences in internal resistance could also affect biofilm growth, limiting development during the critical start-up phase, ultimately effecting maximum power density achievable within a stack of MFCs.

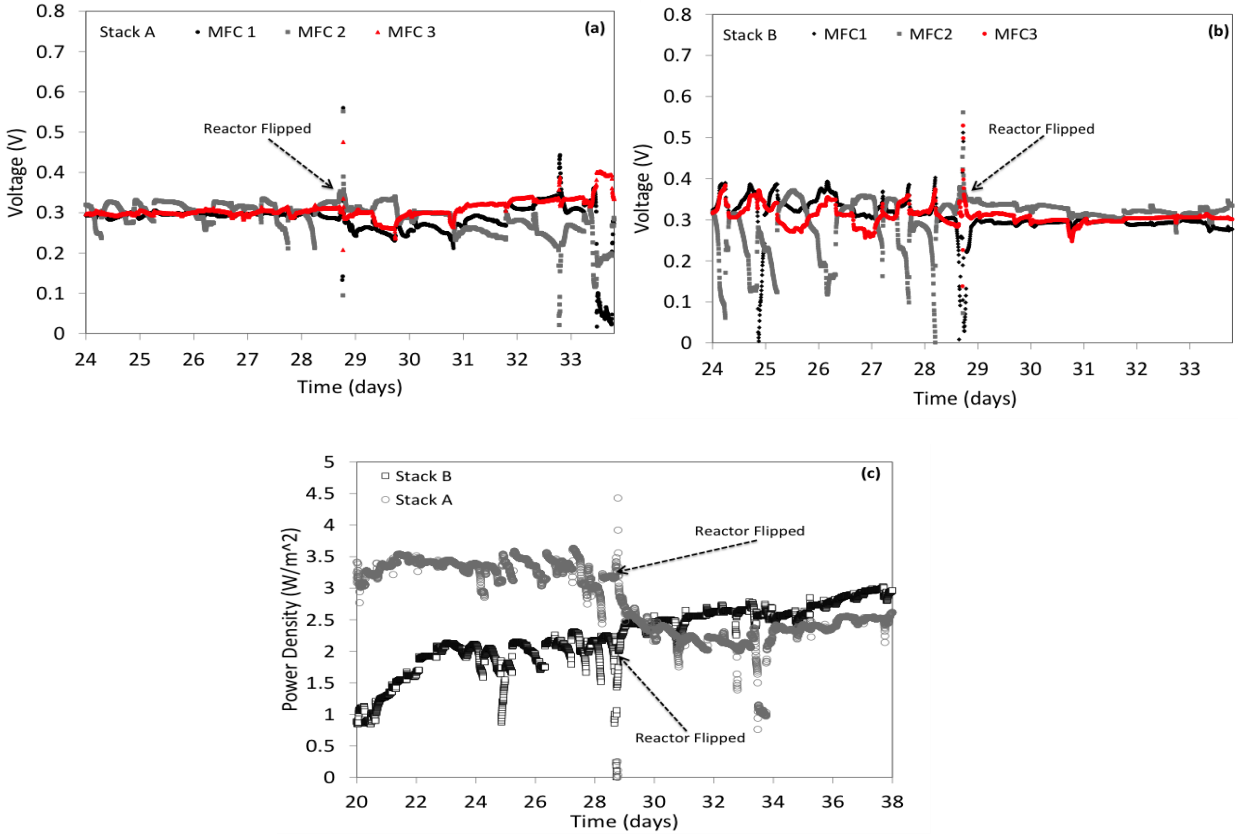

Figure 4. Performance of the reactor before and after flipping showing (a) voltage as a function of time for Stack A; (b) voltage as a function of time for Stack B; and (c) power as a function of time for both Stack A and Stack B.

Effects of operational conditions (HRT, substrate and buffer concentrations) on iCiS-MFC performance

At an acetate concentration of 5.9 g/L, decreasing HRT from 240 min to 120 min resulted in an increase in power density of Stack B by 6% from 2.56 to 2.71 Wm^{-2} (Figure 5a). Further decreasing HRT from 120 min to 80 min resulted in a further increase in power density by 11% (3 Wm^{-2}). However, decreasing HRT from 80 to 60 min did not result in further increase in power density. A similar trend was observed for Stack A.

When the MFC stacks were operated at lower acetate concentration (0.59 g L^{-1}), power density decreased by more than 68% for both Stack A and Stack B. Decreasing HRT of Stack B from 80 min to 40 min resulted in an increase in power density by 21% from 0.55 Wm^{-2} to 0.67 Wm^{-2} (Figure 5b). An additional decrease in HRT from 40 min to 25 min resulted in an additional increase in power density by 46% (0.98 Wm^{-2}). However, further decreasing HRT from 25 to 20 min resulted in a decrease in power density by 12%. A similar trend was observed for Stack A.

The results at both high and low acetate concentration, presented here, indicate that at longer HRTs, substrate can become limiting when iCiS-MFC s are operated hydraulically in series (Janicek et al., 2014) [i]. The decreased performance at the lowest HRTs tested (highest flow rates) was possibly due to lower concentration of produced bicarbonate buffer (Fan et al., 2012) **Hata! Yer işareti tanımlanmamış.**. Furthermore, significantly higher performance was achieved when the reactor was operated at the higher acetate concentration. This has not been shown to be the case for other MFC designs in which increasing acetate concentration beyond 0.59 g L^{-1} did not appreciably affect

performance (Cheng and Logan 2011). The disparity might be due to the high substrate utilization rate achieved in the CEA-MFCs caused by the much higher electrode area/volume ratio and development of a highly efficient anodic biofilm resulting from the lowered internal resistance of the iCiS-MFCs.

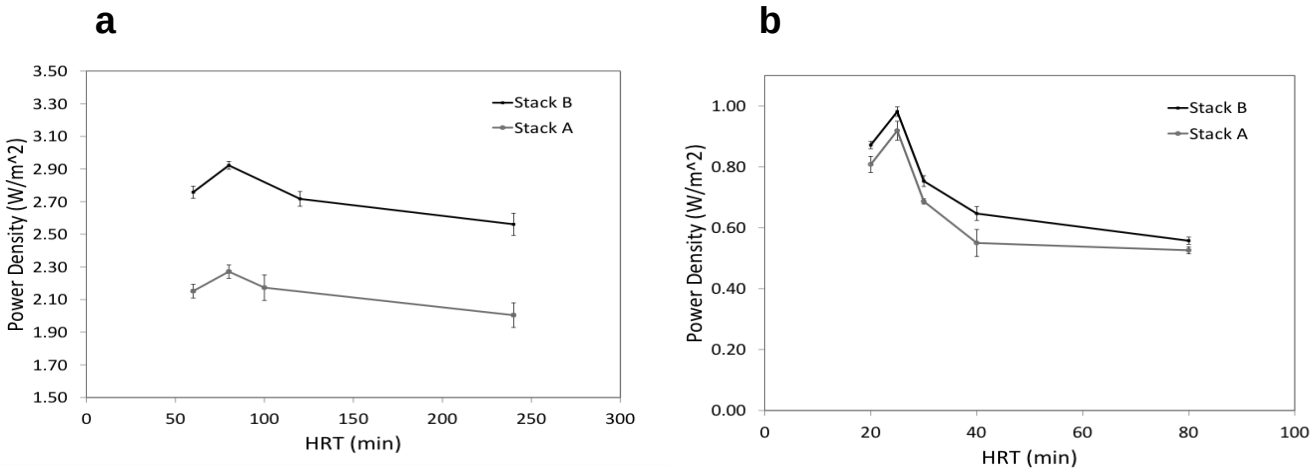

Figure 5. Power density as a function of HRT for (a) Stack A & B operated at higher acetate concentration (5.9 g L^{-1}); and (b) Stack A & B operated at lower acetate concentration (0.59 g L^{-1}).

It is well known that increasing buffer concentration can increase maximum power generation of MFCs (Liu et al., 2005). However, addition of large quantities of buffers will likely be cost prohibitive for practical applications. To investigate how power generation of the newly developed system was affected by the buffer concentration, iCis-MFC stack were also operated under low buffer concentration (10 mM PBS). Results show that power reached a maximum of 1.5 Wm^{-2} at an acetate concentration of 5.9 g L^{-1} (Figure 6). This represents only 50% decrease in power density when buffer concentration is decreased from 80 mM PBS to 10 mM, suggesting the produced bicarbonate might considerably contribute to the reduction in internal resistance. When the substrate concentration decreased to 0.59 g L^{-1}, the power density further decreased to 0.5 Wm^{-2} and remained stable over the 150 days of operation. (Figure 7a and b, Figure S2). The significant decrease in power density at lower acetate concentration might be due to substrate limitation and less produced bicarbonate buffers.

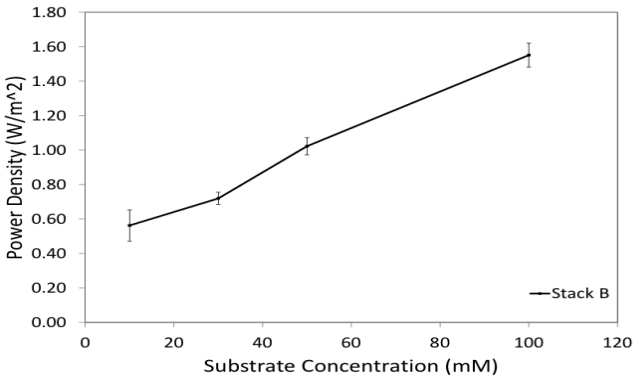

Figure 6. Power density as a function of substrate (acetate) concentration for Stack B operated at 10 mM PBS.

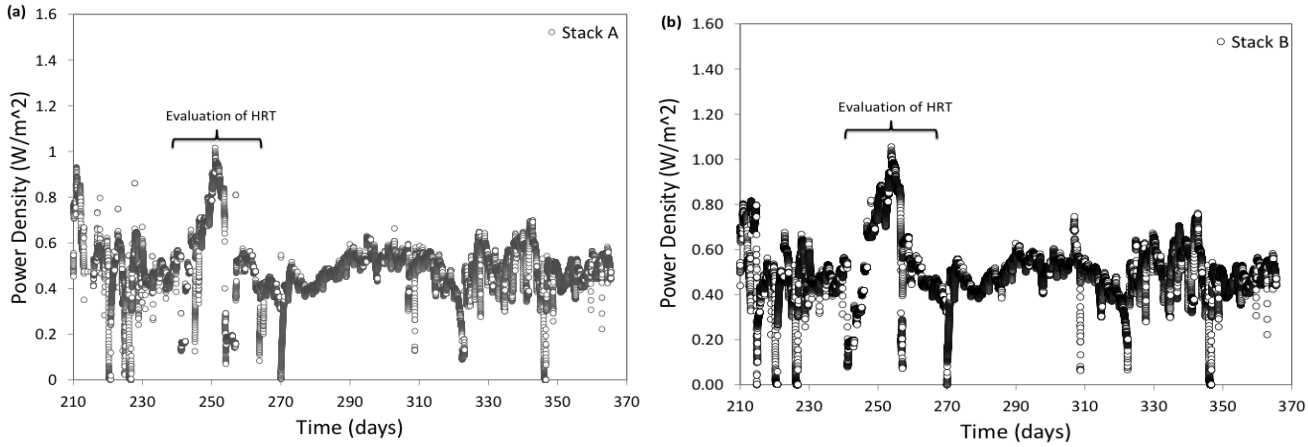

Figure 7. Power density as a function of at an acetate concentration of 0.59 g L-1 and buffer concentration of 10 mM PBS for (a) Stack A; and (b) Stack B.

Conclusions

Results presented here demonstrate that the iCiS-MFCs can achieve a high stable power output of over 3 W/m^2 at an overall voltage output of 0.9 V. The high performance can be attributed to both the CEA structure and the design of internal series connection, which lead to lower internal resistance. The lowered internal resistance combined with the fact that the reactor was acclimated at the higher acetate concentration (5.9 gL^{-1}), may also have allowed a highly efficient anodic biofilm to develop. The internal series connection also alleviated the need for a current collector, resulting in reduced cost for fabrication and enhanced reliability. With this design, reactor size was increased significantly with no decrease in performance, as is typically the case when increasing MFC reactor size. Voltage reversal, a common issue for serially connected MFCs, hasn't affected the operation of the iCiS-MFC during the one-year operation. These results clearly demonstrate the great potential of this iCiS-MFC s design for scaling-up.

Lower performance when both stacks were operated as the top reactor suggests that trapped gas may be an issue during scale-up if the current operational mode is used. One alternative is to operate the reactor in a vertical orientation rather than the current horizontal orientation. Vertical orientation in combination with gas release mechanisms may prevent gas from becoming trapped between electrodes. The activated carbon/carbon cloth cathode used in this study is well suited for this type of operation, as it has shown high pressure tolerance (Janicek et al., 2015a; Janicek et al., 2015b). Results presented here also indicate that a high degree of voltage variability between MFCs in a stack, during start-up, may lead to lower performance during the stable power output phase. Facilitating even biofilm growth during start-up phase seems crucial.

The high and low acetate concentrations tested in the reactor represent COD values of approximately 6000 mg L^{-1} COD and 600 mg L^{-1} COD, respectively, as representatives of typical food pressing wastewater and municipal wastewater. The significantly higher power density of the reactor at the higher acetate concentration suggests that treating wastewaters with higher COD values would be more appropriate for the iCiS-MFC to balance the energy recovery and capital cost. Treating municipal wastewater may not justify the current expense of MFC technology, as adequate energy may not be generated to offset the high cost of MFCs. In addition, despite the low internal resistance caused by the internal series connection compared to reactors connected in series that don't contain this feature, low buffer concentration presents a significant challenge to performance, especially when substrate concentration is also low. Further scaling up this reactor could be accomplished by increasing the number of MFCs connected in series as well as increasing the size of each MFC. Further investigation into scaling-up the iCiS-MFC design will ultimately determine any limitations with respect to size and reactor effectiveness for practical application.

Funding

The authors would like to acknowledge support from the US National Science Foundation (CBET 0955124, PFI 1312301).

Conflict of interest

The authors declare no conflict of interest.

Data availability statement

Data can be obtained from the corresponding author upon a reasonable request. Supporting information includes additional figures that are referenced in the text. This material is available free of charge via the Internet.

Ethics committee approval

Ethics committee approval is not required for this study.

Authors' contribution statement

The authors acknowledge their contributions to this paper as follows: **Study conception and design**: H.L., Y.F., A.J.; **Data collection**: A.J., Y.F.; **Analysis and interpretation of results**: Y.F., A.J., H.L.; **Manuscript draft preparation**: A.J., Y.F. All authors reviewed the results and approved the final version of the manuscript.

References

Adami, S.E., Degrenne, N., Haboubi, W., Takhedmit, H., Labrousse, D., Costa, F., Allard, B., Luk, J.D.L.S., Cirio, L., Picon, O., & Vollaire, C., (2013). Ultra-Low Power, Low Voltage, Self-Powered Resonant DC-DC Converter for Energy Harvesting. *Journal of Low Power Electronics*, *9*, 103–117. https://doi.org/10.1166/jolpe.2013.1245

Aelterman, P., Rabaey, K., Pham, H. T., Boon, N., & Verstraete, W. (2006). Continuous electricity generation at high voltages and currents using stacked microbial fuel cells. *Environmental science & technology*, *40*(10), 3388–3394. https://doi.org/10.1021/es0525511

Cheng S., & Logan, B.E., (2011). Increasing power generation for scaling up single-chamber air cathode microbial fuel cells. *Bioresource Technology*, *102*, 4468-4473. https://doi.org/10.1016/j.biortech.2010.12.104

Cheng, S., Ye, Y., Ding, W., & Pan, B. (2014). Enhancing power generation of scale-up microbial fuel cells by optimizing the leading-out terminal of anode. *Journal of Power Sources, 248*, 931–938. http://dx.doi.org/10.1016/j.jpowsour.2013.10.014

Dekker, A., Ter Heijne, A., Saakes, M., Hamelers, H. V., & Buisman, C. J. (2009). Analysis and improvement of a scaled-up and stacked microbial fuel cell. *Environmental science & technology*, *43*(23), 9038–9042. https://doi.org/10.1021/es901939r

Dong, Y., Qu, Y., He, W., Du, Y., Liu, J., Han, X., & Feng, Y. (2015). A 90-liter stackable baffled microbial fuel cell for brewery wastewater treatment based on energy self-sufficient mode. *Bioresource technology*, *195*, 66–72. https://doi.org/10.1016/j.biortech.2015.06.026

Donovan, C., Dewan, A., Peng, H., Heo, D., & Beyenal, H., (2011). Power management system for a 2.5 W remote sensor powered by a sediment microbial fuel cell. *Journal of Power Sources*, *196*, 1171–1177. https://doi.org/10.1016/j.jpowsour.2010.08.099

Fan, Y., Hu, H., Liu, H., (2007). Enhanced Coulombic efficiency and power density of air-cathode microbial fuel cells with an improved cell configuration. *Journal Power Sources*, *171*, 348-354. https://doi.org/10.1016/j.jpowsour.2007.06.220

Fan, Y., Sharbrough, E., & Liu, H. (2008). Quantification of the internal resistance distribution of microbial fuel cells. *Environmental science & technology*, *42*(21), 8101–8107. https://doi.org/10.1021/es801229j

Fan, Y., Han, S.K., & Liu, H., (2012). Improved performance of CEA microbial fuel cells with increased reactor size. *Energy & Environmental Science*, *5*, 8273–8280. https://doi.org/10.1039/C2EE21964F

Feng, Y., He, W., Liu, J., Wang, X., Qu, Y., & Ren, N. (2014). A horizontal plug flow and stackable pilot microbial fuel cell for municipal wastewater treatment. *Bioresource technology*, *156*, 132–138. https://doi.org/10.1016/j.biortech.2013.12.104

Ge, Z., Wu, L., Zhang, F., & He, Z. (2015). Energy extraction from a large-scale microbial fuel cell system treating municipal wastewater. *Journal of Power Sources*, *297*, 260–264. https://doi.org/10.1016/j.jpowsour.2015.07.105

Gurung, A., Kim, J., Jung, S., Jeon, B. H., Yang, J. E., & Oh, S. E. (2012). Effects of substrate concentrations on performance of serially connected microbial fuel cells (MFCs) operated in a continuous mode. *Biotechnology letters*, *34*(10), 1833–1839. https://doi.org/10.1007/s10529-012-0979-3

Gurung, A., & Oh, S.E., (2012). The Performance of Serially and Parallelly Connected Microbial Fuel Cells. *Energy Sources, Part A: Recovery, Utilization and Environmental Effects*, *34*, 1591–1598. https://doi.org/10.1080/15567036.2011.629277

Janicek, A., Fan, Y., & Liu, H., (2014). Design of microbial fuel cells for practical application: a review and analysis of scale-up studies. *Biofuels*, *5*, 79-92. https://doi.org/10.4155/bfs.13.69

Janicek, A., Fan, Y. & Liu, H., (2015a). Performance and stability of different cathode base materials for use in microbial fuel cells. *Journal of Power Sources*, *280*, 159-165. https://doi.org/10.1016/j.jpowsour.2015.01.098

Janicek, A., Gao, N., Fan, Y., & Liu, H. (2015b). High performance activated carbon/carbon cloth cathodes for microbial fuel cells. *Fuel Cells*, *15*(6), 855-861. https://doi.org/10.1002/fuce.201500120

Ieropoulos, I., Greenman J., & Melhuish, C., (2008). Microbial fuel cells based on carbon veil electrodes: Stack configuration and scalability. *International Journal of Energy Research*, *32*, 1228–1240. https://doi.org/10.1002/er.1419

Liu, H., Cheng, S., & Logan, B.E., (2005). Power Generation in Fed-Batch Microbial Fuel Cells as a Function of Ionic Strength, Temperature, and Reactor Configuration. *Environmental Science and Technology*, *39*, 5488–5493. https://doi.org/10.1021/es050316c

Logan B. E. (2010). Scaling up microbial fuel cells and other bioelectrochemical systems. *Applied microbiology and biotechnology*, *85*(6), 1665–1671. https://doi.org/10.1007/s00253-009-2378-9

Logan, B. E., & Rabaey, K. (2012). Conversion of wastes into bioelectricity and chemicals by using microbial electrochemical technologies. *Science (New York, N.Y.)*, *337*(6095), 686–690. https://doi.org/10.1126/science.1217412

Logan, B. E., Wallack, M. J., Kim, K. Y., He, W., Feng, Y., & Saikaly, P. E. (2015). Assessment of Microbial Fuel Cell Configurations and Power Densities. *Environmental Science and Technology Letters*, *2*(8), 206-214. https://doi.org/10.1021/acs.estlett.5b00180

Lovley, D. R., & Phillips, E. J. (1988). Novel mode of microbial energy metabolism: organic carbon oxidation coupled to dissimilatory reduction of iron or manganese. *Applied and environmental microbiology*, *54*(6), 1472–1480. https://doi.org/10.1128/aem.54.6.1472-1480.1988

Oh, S.E.. Logan, B.E., (2007). Voltage reversal during microbial fuel cell stack operation. *Journal of Power Sources*, *67*, 11–17. https://doi.org/10.1016/j.jpowsour.2007.02.016

Perlack, R D. Biomass as Feedstock for a Bioenergy and Bioproducts Industry: The Technical Feasability of a Billion-Ton Annual Supply. United States. https://doi.org/10.2172/885984

Wang, H. Y., Bernarda, A., Huang, C. Y., Lee, D. J., & Chang, J. S. (2011). Micro-sized microbial fuel cell: a mini-review. *Bioresource technology*, *102*(1), 235–243. https://doi.org/10.1016/j.biortech.2010.07.007

Wei, J., Liang, P., & Huang, X. (2011). Recent progress in electrodes for microbial fuel cells. *Bioresource technology*, *102*(20), 9335–9344. https://doi.org/10.1016/j.biortech.2011.07.019

Wu, P. K., Biffinger, J. C., Fitzgerald, L. A. & Ringeisen, B. R. A., (2012). low power DC/DC booster circuit designed for microbial fuel cells. *Process Biochemistry, 47*, 1620–1626. https://doi.org/10.1016/j.procbio.2011.06.003

Zhu, N.W., Chen, X., Tu, L.X., Wu, P.X., & Dang, Z., (2021). Voltage reversal during stacking microbial fuel cells with or without diodes. *in Advanced Materials Research*, 396–398. Switzerland: Trans Tech Publications, pp. 188–193, http://dx.doi.org/10.4028/www.scientific.net/AMR.396-398.188